MODELING AND OBSERVATIONAL STUDIES OF

SEA ICE - MIXED LAYER INTERACTIONS ON THE WEST

ANTARCTIC PENINSULA CONTINENTAL SHELF

by

David Allen Smith
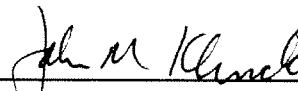B.S. June 1990, West Virginia University

A Dissertation Submitted to the Faculty of
Old Dominion University in Partial Fulfillment of the
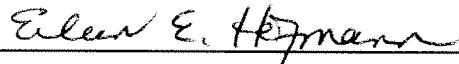Requirements for the Degree of

DOCTOR OF PHILOSOPHY
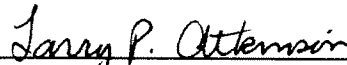
OCEANOGRAPHY

OLD DOMINION UNIVERSITY
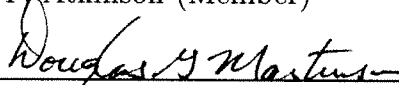December 1999

Approved by:

J. M. Klinck (Director of Advisory
Committee)

E. E. Hofmann (Member)

L. P. Atkinson (Member)

D. Martinson (Member)

ABSTRACT

MODELING AND OBSERVATIONAL STUDIES OF SEA ICE - MIXED LAYER INTERACTIONS ON THE WEST ANTARCTIC PENINSULA CONTINENTAL SHELF

David Allen Smith
Old Dominion University, 1999
Director: Dr. J. M. Klinck

Meteorological and hydrographic observations collected between January and August of 1993 are used to characterize the hydrographic structure, heat content, heat exchange at the air/ice/sea interface and to force numerical models for the continental shelf waters to the west of the Antarctic Peninsula.

Individual components for the 1993 heat budget are quantified and ranked indicating that incoming short wave radiation (Q_{sw}), with values in excess of 150 to 200 W m^{-2}, dominate the overall summer budget. Conversely, the winter budget is dominated by sensible heat losses which typically on the order of 50 W m^{-2} with episodic losses exceeding values of 150 W m^{-2}. These episodic losses coincide with periods of cold atmospheric temperatures ($T_{air} <$ -15 °C) and are on the same time scales as those associated with the passage of synoptic low pressure systems through Drake Passage.

A vertical time-dependent thermodynamic ice-ocean model is developed and forced with 1993 heat fluxes to further investigate the vertical transfer of heat through Antarctic Surface Water (AASW) and to characterize the time dependent hydrographic structure of the mixed layer. The timing of the simulated ice cycle was consistent with the timing of a satellite derived ice cycle. The simulations indicate that a heat loss of 10 to 20 W m^{-2} from AASW to the ice persist through the year and that a balance between this heat loss and heat fluxes at the ice/ocean interface control overall ice growth. A persistent resupply of heat through the pycnocline to the base of AASW on the order of 10 to 20 W m^{-2} is simulated and is primarily

driven by double diffusion. The differential vertical transfer of heat and salt resulting from double diffusion is shown to be important to the hydrographic structure of AASW.

The numerical simulations and the heat flux calculations based on 1993 hydrographic and meteorological data indicate that vertical processes are important to the hydrographic structure of the mixed layer along the west Antarctic Peninsula. Horizontal processes, such as advection, such as advection are not necessary to close regional heat budgets.

This dissertation is dedicated to my family.

ACKNOWLEDGMENTS

I sincerely thank Drs. John Klinck and Eileen Hofmann for their support throughout my tenure as a student. I am also thankful to the members of the faculty and staff who had an interest in my education at the Center for Coastal Physical Oceanography. I am especially thankful to the members of my dissertation committee Drs. Larry Atkinson and Douglass Martinson for their guidance throughout the project.

I am very fortunate to have shared my graduate experience with many students at the Center for Coastal Physical Oceanography. In particular I would like to thank former office mates Cathy Lascara and John Holdzkom. My graduate experience was greatly enriched by my professional and personal relationships with Cathy and John.

To my parents, David and Sandy, I am grateful for the advice, support and guidance that you gave me through the years. Finally I would like to thank my wife, Robin, and my two daughters Marianna and Alison. I can not imagine what my experience would have been like without your never ending love and support.

TABLE OF CONTENTS

TABLE OF CONTENTS (continued) Page

TABLE OF CONTENTS (continued) Page

TABLE OF CONTENTS (continued)

LIST OF TABLES Page

LIST OF FIGURES Page

LIST OF FIGURES (continued)

LIST OF FIGURES (continued) Page

CHAPTER 1

INTRODUCTION

The waters to the west of the Antarctic Peninsula (WAP) (Figure 1) have long been recognized for their biological importance. Marr's [1962] interpretation of the 1934 *Discovery* data indicated that shelf waters to the west of Antarctic Peninsula are a region with abundant concentrations of Antarctic krill (*Euphausia superba*). The biological importance of the region has received extensive attention since Marr's [1962] original observation in such international programs as the First and Second International Biomass Experiments (FIBEX and SIBEX, respectively) [Gordon and Nowlin, 1978; Everson and Miller, 1994; Nowlin and Clifford, 1982; Sievers and Nowlin, 1984; Stein, 1983; Stein and Rakusa-Suszczewiski, 1983, 1984; and Stein, 1986, 1989] and German research efforts [Huntley et al., 1991; Niiler et al., 1991 and Stein, 1992].

In 1990, the National Science Foundation funded a Long-Term Ecological Research (LTER) site based at Palmer Station (i.e. Palmer LTER program), on Anvers Island (Figure 1), designed to study the ecology along the west Antarctic Peninsula shelf and its relation to the physical environment. The central hypothesis of the program is that many of the observed biological processes along the west Antarctic Peninsula shelf are related to the seasonal advance and retreat of the ice edge [Smith et al., 1995].

The waters to the west of the Antarctic Peninsula are characterized by a seasonal ice cover which cycles between nearly ice-free, summer conditions to full ice cover in the winter [Stammerjohn and Smith, 1996]. The maximum extent of the winter ice cover exhibits interannual variability characterized by years of high and low ice cover. The ice cycle is correlated with cold and warm winter atmospheric conditions

---

[1]The *Journal of Geophysical Research* was used as the journal model.

[Stammerjohn and Smith, 1996].

The primary objective of this research is to identify, quantify and rank the importance of physical processes which underlie the observed hydrographic structure and mixed layer dynamics within the continental shelf waters to the west of the Antarctic Peninsula. It is believed that key features in the mixed layer, which affect the region's biological processes, are determined by physical processes such as exchange of heat and salt at the air-ice-sea interface and across-shelf interactions with the Antarctic Circumpolar Current (ACC). It is also believed that the ocean may play an important feedback role in the complex atmosphere/ice cycle within the region. The approach taken to achieve this objective will involve the analysis of hydrographic and atmospheric data to form conceptual models of water mass interaction and surface heat flux exchanges. These conceptual models will then be extended into numerical studies.

The specific research questions addressed in this research are:

- Given the spatial and temporal variability of the water masses along the western Antarctic Peninsula shelf, what can be inferred about the underlying physics?

- What are the relative contributions of wind mixing, buoyancy forcing (i.e. ice related process and atmospheric fluxes), double diffusion and other vertical processes on the time evolution of the surface mixed layer?

- To what extent can vertical processes account for observed hydrographic structure, mixed-layer dynamics and temporal sea ice distributions? Are horizontal exchanges necessary to balance the vertical processes?

In recognition of the limited historical data coverage along the west Antarctic Peninsula [Hofmann et al., 1996], the Palmer LTER program includes a component
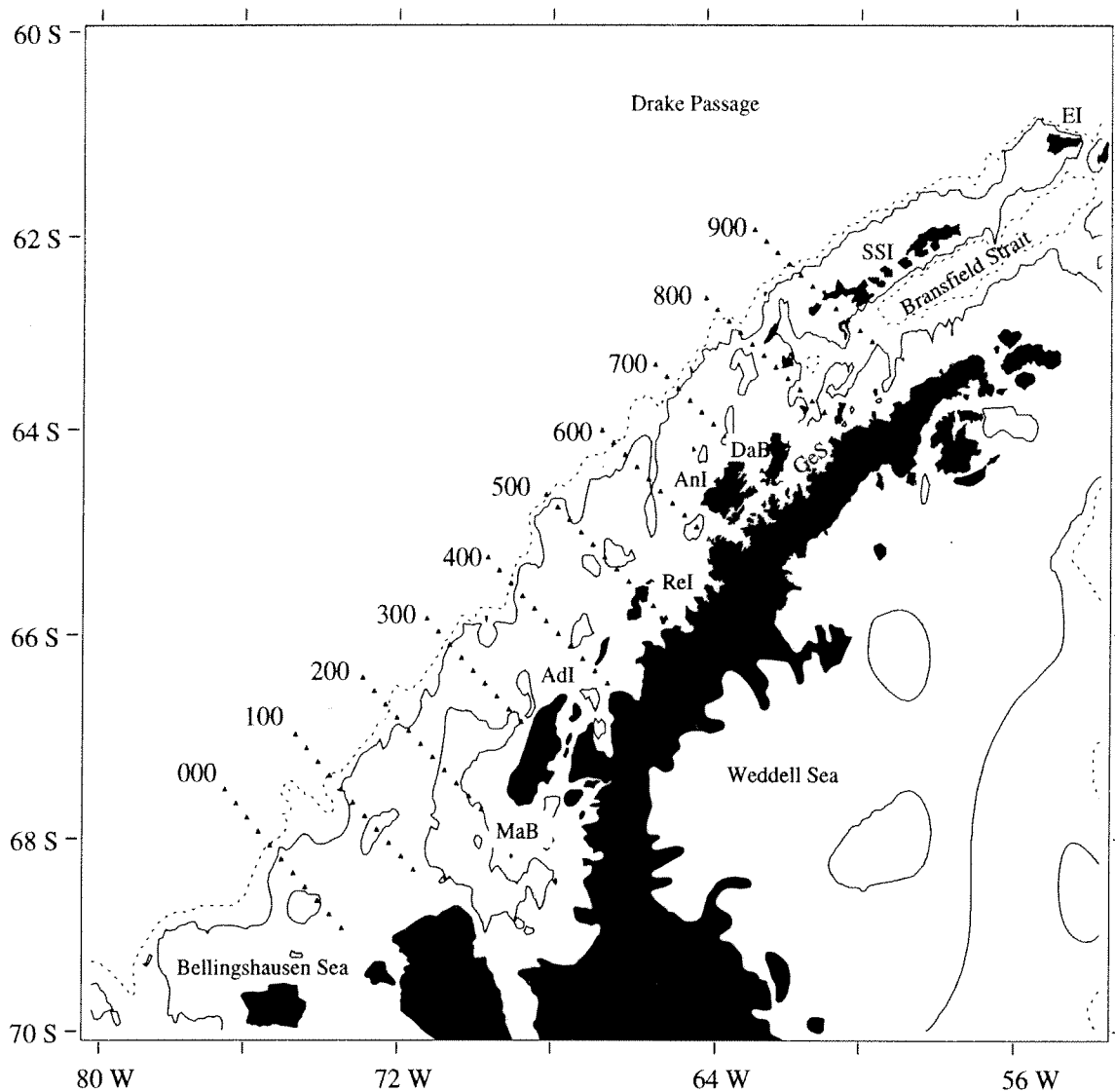
Figure 1. Palmer LTER study region along the west Antarctic Peninsula continental shelf. The across-shelf sampling distribution is indicated by the triangles. Across-shelf stations are separated by 10 km and the 10 across-shelf transects (000 line through the 900 line moving southwest to northeast) are separated by 100 km. The 500 and 1000 m isobaths are indicated with the solid, and dotted lines, respectively. Geographic locations are abbreviated as: AdI-Adelaide Island, AnI-Anvers Island, DaB-Dallman Bay, EI-Elephant Island, GeS-Gerlache Strait, MaB-Marguerite Bay, ReI-Renaud Island and SSI South Shetland Islands.

designed to sample the region at least once a year with multiple cruises within certain years. The resulting hydrography is the most extensive, synoptic hydrographic data set for the west Antarctic Peninsula shelf waters to date and provides an excellent basis for the study of the region's physical properties. Investigations using these data are presented in Klinck and in Smith et al. [1999] and indicate that vertical heat fluxes may be dominated by the double diffusive instability and balanced by a slow and/or intermittent across shelf flux of heat from offshore. These concepts will be expanded and investigated further in this study.

The numerical modeling component of this research will consist of several process oriented studies and will involve the development of a vertical mixed layer model capable of including the effects of ice cover. This will be achieved by coupling a thermodynamic-dynamic ice model to the level 2.5 turbulence closure scheme [Mellor and Yamada, 1982] of the Princeton Ocean Model (POM), thus providing time dependent turbulent vertical mixing terms. This scheme has been found to reproduce realistic dynamics of the mixed layer [Blumberg and Mellor, 1987]. This model is used to evaluate the importance of vertical process on the structure of the mixed layer. These processes include the effects of wind driven turbulence mixing, surface buoyancy flux and double diffusion on vertical flux of heat and salt.

It is anticipated that this research will lend insight into the physical processes which influence the mixed layer dynamics of waters over the continental shelf west of the Antarctic Peninsula. Given the strong relationship between the physical environment in the region and biological processes, it is expected that this research will interest biologists. It is also believed that the oceanic response, and potential oceanic feedback into the coupled air/ice/sea system, will interest atmospheric scientists. The basic concepts explored in this research are fundamental to the development of models used to predict the response of the coupled physical-biological processes along the west Antarctic Peninsula to climatic change.

CHAPTER 2

BACKGROUND

The first section of this chapter gives a brief overview of the Palmer LTER program including its primary objectives, sampling grid, design and sampling strategy. The following section is a summary of previous hydrographic and circulation studies along the west Antarctic Peninsula. The third section provides a brief overview of meteorological and sea ice observations for the west Antarctic Peninsula region. The final section summarizes numerical modeling studies for the west Antarctic Peninsula region and adjacent seas and provides a general overview of ice-ocean modeling.

2.1 Palmer LTER program

The Palmer LTER program, based at Palmer Station on Anvers Island (Figure 1), has as a central hypothesis that interannual variability in the region's physical environment, in particular the extent of winter sea ice cover, drives interannual variability observed in the region's biology [Smith et al., 1995]. The program is multidisciplinary and includes components designed to collect, synthesize and model many of the physical and biological components of the regional environment and ecosystem, including the region's meteorology, sea ice, chemistry, hydrography and biology.

A sampling grid was established for the Palmer LTER [Waters and Smith, 1992] which extends 900 km along the west Antarctic Peninsula from the Bransfield Strait to Alexander Island (Figure 1). The offshore extent of the grid is 200 km. The grid is composed of 10 across-shelf transects with a 100 km separation. The southernmost across-shelf transect is designated the 000 line while the northernmost transect is the 900 line. A baseline connects the innermost stations on each across shelf transect

and runs parallel to the peninsula. Following the Palmer LTER naming convention, a station which is 100 km away from innermost station on the 600 line would be referred to as the 600.100 station.

The offshore extent of the grid is sufficient to encompass the entire shelf which averages 400 m in depth. The 1000 m isobath (Figure 1) is the general location of the shelf break while the 500 m isobath demonstrates the highly irregular bathymetry of the shelf. The shelf is interrupted by several depressions which run from the outer to the inner shelf. One such cut intersects the 600 line to the west of Anvers Island (Figure 1) and provides a deep conduit for potential exchange of shelf waters with oceanic waters located offshore.

The basic sampling strategy for the Palmer LTER program includes an annual occupation the 200, 300, 400, 500 and 600 lines during the ice free summer months. During 1993, the region was sampled three times including cruises in the summer, fall and winter. The most extensive sampling was conducted as part of the fall cruise where the entire grid (000 to 900 lines) was sampled over a 2 month period. This fall cruise included a hydrographic survey with an across shelf resolution of 10 km and provided the most comprehensive, synoptic, hydrographic survey for the region to date.

2.2   Hydrography and circulation

The hydrography of the west Antarctic Peninsula was first mapped in the 1930's during the *Discovery* cruises to the Weddell-Scotia confluence and the Bransfield Strait [Clowes, 1934]. The northern shelf waters to the west of the Antarctic Peninsula (Figure 1) was revisited during 1970's as part of the International Southern Ocean Studies (ISOS) program [Gordon and Nowlin, 1978; Nowlin and Clifford, 1982; Sievers and Nowlin, 1984]. Interest in the region's biology initiated sampling through the 1980's as part of the First and Second International Biomass Experiments (FIBEX

and SIBEX, respectively) [Stein, 1983; Stein and Rakusa-Suszczewski, 1983, 1984]. While the focus of the FIBEX and SIBEX programs was biological in nature, hydrographic data were collected. These data were generally restricted to the top 100 - 200 m of the water column, cluster around the Bransfield Strait, and do not extend south along the Peninsula.

Hydrographic results from the ISOS, FIBEX and SIBEX studies along the west Antarctic Peninsula can be summarized as follows: (1) The entire sub-pycnocline waters along the west Antarctic Peninsula shelf (excluding the Bransfield Strait) are characterized by warm, salty, oceanic water originating in the Antarctic Circumpolar Current (ACC) as Circumpolar Deep Water (CDW). (2) Within the Bransfield Strait, the deep waters lack the prominent, sub-surface temperature maximum characteristic of CDW and most likely originate along the western shelf of the Weddell Sea [Whitworth et al., 1994]. (3) The highly variable surface waters of the west Antarctic Peninsula are consistent with those of Antarctic Surface Water (AASW) which extend southward from the polar front to the Antarctic continent [Sievers and Nowlin, 1984].

In a review of historical data along the west Antarctic Peninsula, Hofmann et al. [1996] concluded that there is limited interaction between the deep waters of the Bransfield and those of the west Antarctic Peninsula. They also concluded that the west Antarctic Peninsula differs from other Antarctic shelf systems (e.g., Weddell and Ross Seas) as it does not appear to be a site of dense shelf water formation.

While little is known about the hydrography along the west Antarctic Peninsula, even less is known about its circulation. Drifter data indicate that the surface currents flow northward through the Gerlache and Bransfield straits, forming the Bransfield current [Niiler, 1990]. To date, few direct current measurements exist for the west Antarctic Peninsula shelf south of the Bransfield Strait. An estimate of the geostrophic currents, confirmed from limited hydrographic measurements, for

the west Antarctic Peninsula are presented in [Stein, 1992] and suggest that weak cyclonic gyres may exist on the continental shelf.

2.2.1 Hydrographic observations from the Palmer LTER program

The most extensive, synoptic hydrographic data set along the west Antarctic Peninsula has been collected during several cruises that were part of the Palmer LTER program. These cruises were conducted in the austral summer, fall and winter of 1993, the austral summer of 1994 and the austral spring of 1991. Details on the data coverage and processing during the individual cruises are given in Klinck et al. [1994], Lascara et al. [1993a, 1993b] and Smith et al. [1993a, 1993b]. These hydrographic data have been used to develop a detailed descriptions of the water masses found along the west Antarctic Peninsula [Smith et al., 1999], thermohaline variability [Hofmann and Klinck, 1998] and changes in the heat and salt content of the water column during the 1993 sampling season [Klinck, 1998]. Results from these studies are summarized below.

The continental shelf waters along the west Antarctic Peninsula can be characterized as a two layer system which is separated by a distinct permanent pycnocline (Figure 2). The upper layer consists of the highly variable AASW which is in direct contact with the atmosphere and exhibits variability in its heat and salt content on seasonal (and shorter) time scales [Klinck, 1998; Smith et al., 1999]. The seasonal variability of AASW (Figure 3) is minimum in the winter and maximum in the fall. During this later period, the surface waters were characterized by multiple mixed layers at a wide range of temperatures and salinities [Smith et al., 1999]. Klinck [1998] calculates changes in heat content for the upper portion of the water column along the west Antarctic Peninsula using temperature data acquired during the 1993 and 1944 cruises to the west Antarctic Peninsula shelf. He demonstrates that AASW evolves from well mixed winter conditions (T $\sim$ -1.9 °C and S $\sim$ 34

Qi   Qopen

z=0m   X

ice   ice

AASW

Qsur

AASW(WW)   T < -1.5 C S~33.8 psu

z=150 - 200 m

Qv

z=300 m   UCDW

Qh   modified-UCDW   T = 1.2 to 1.4 C
S = 34.65 to 34.7 psu

H

T > 1.6 C
S ~ 34.7 psu

z= 400 m

dx=25km

L=100-150 km

z
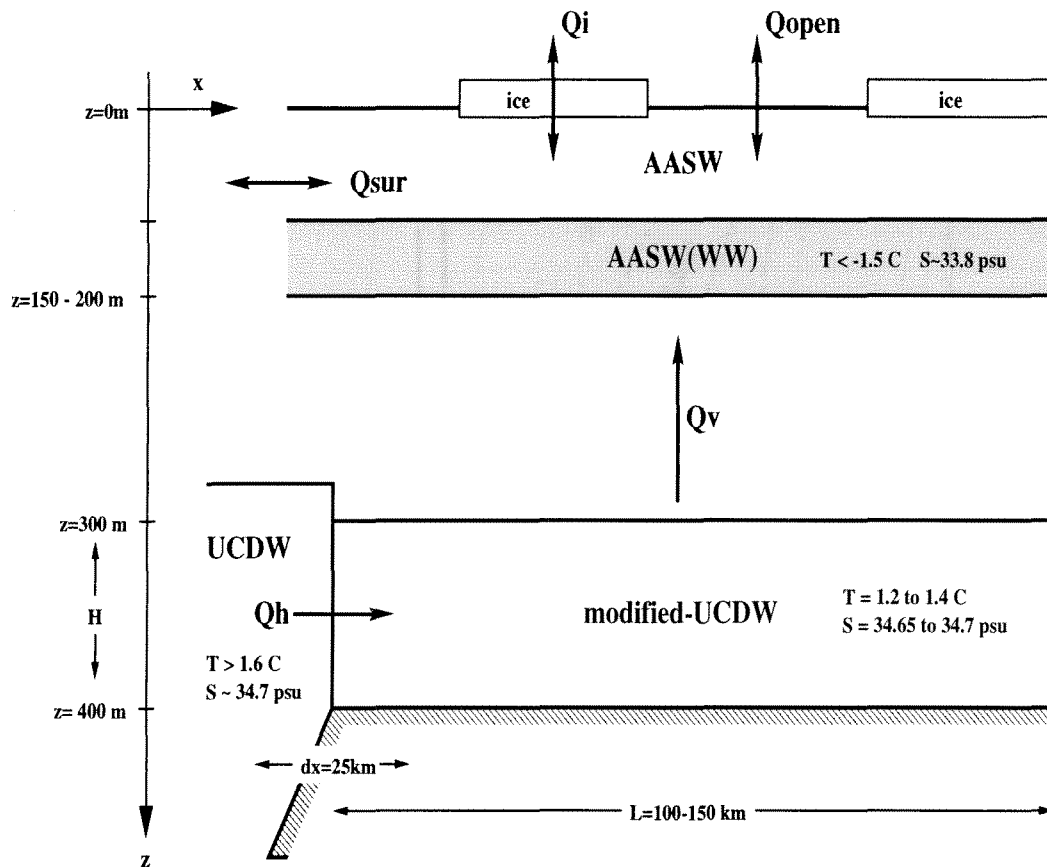
Figure 2. Schematic water mass distribution and box model. Antarctic surface water (AASW) and its end member, Winter Water (WW) occupy the top 100 to 200 m of the water column. The sub-pycnocline waters are UCDW and modified-UCDW which are located on the oceanic and shelf side of the shelf break, respectively. Arrows indicate potential mixing and water mass exchange pathways. Idealized shelf dimensions which are used in box model calculations for the shelf to quantify the individual heat fluxes (Q's), are indicated.
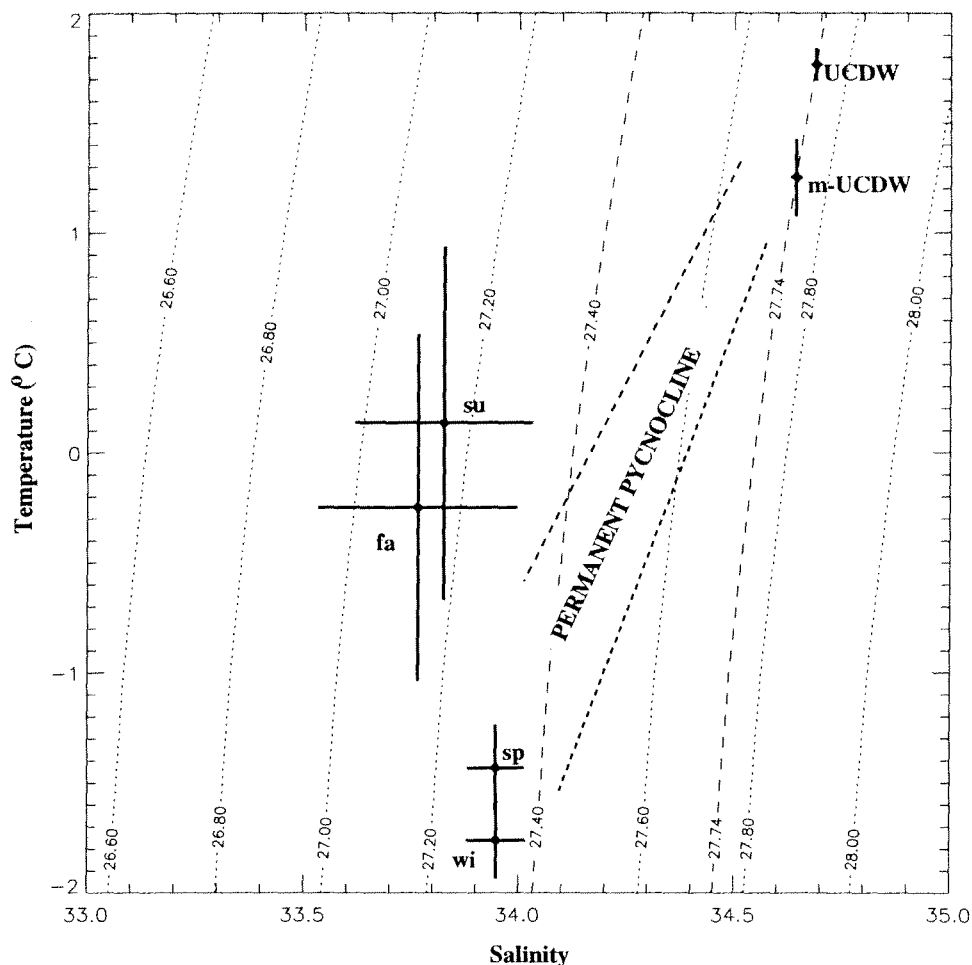
Figure 3. Hydrographic statistics from the Palmer LTER program. θ-S diagram from hydrographic data collected as part of the Palmer LTER program excluding the Bransfield Strait. The statistical envelopes found at $\sigma < 27.4$ represent surface θ-S means (± 1 s.d.) for a winter, spring, summer and fall cruise (wi, sp, su and fa, respectively). Combined θ-S means (± 1 s.d.) for the sub-pycnocline waters along $\sigma = 27.74$ are also indicated. The statistics for water with a temperature above 1.6 °C are labeled "UCDW" while the statistics for water below 1.6 °C are labeled as "m-UCDW" (modified-UCDW). Dashed lines show the general position of the permanent pycnocline. Constant density is indicated with curved dotted lines; the 27.4 and 27.74 isopycnals are indicated with dashed lines.

extending to a depth of 150 m) to summer, stratified conditions with an average heating rate on the order of 60 W m^{-2}.

Two key hydrographic features which characterize the surface layer are the depth of winter water (WW) and the depth of the mixed layer (*mld*). The coldest end member of AASW is termed WW and is the portion of AASW which is sufficiently deep to retain its temperature and salinity acquired during the previous winter [Mosby, 1934; Sievers and Nowlin, 1984] and forms a distinct temperature minimum just above the permanent pycnocline (Figure 4a). The *mld* is generally considered to be the maximum depth of surface mixing and is represented by the well mixed surface waters with uniform fairly uniform temperature and salinity (Figure 4a). The *mld* for the west Antarctic Peninsula shelf waters is controlled by stratification, wind mixing and buoyancy forcing associated with surface fluxes of heat and salt and is defined in this study to be the depth where the buoyancy frequency (N^2) exceeds an arbitrary threshold of 0.2×10^{-4} rad^2 s^{-2} (Figure 4b) (other thresholds can be used yielding similar results). During the winter, the mixed layer can extend to the top of the permanent pycnocline (i.e. to the depth of WW) (Figure 5e,f). During the spring, summer and fall, surface stratification resulting from surface heating and the input of fresh water results in shallow *mld's* (Figures 5a,c). Under conditions of surface stratification, a seasonal pycnocline can form between the mixed layer and WW (Figure 4a).

The sub-pycnocline waters along the shelf generally consist of warm, salty (T > 1.4 °C and S ~ 34.7) water of oceanic, off-shelf origin (Figure 3). The statistics presented on the 27.74 isopycnal (Figure 3) indicate two things: 1) the sub-pycnocline waters form two distinct classes and 2) there exists little variability in their properties over time as indicated by the existence of two distinct clusters of data. The latter of these two observations is consistent with the temperature distributions from the historical record [Hofmann et al., 1996] which includes over 50 years of observa-
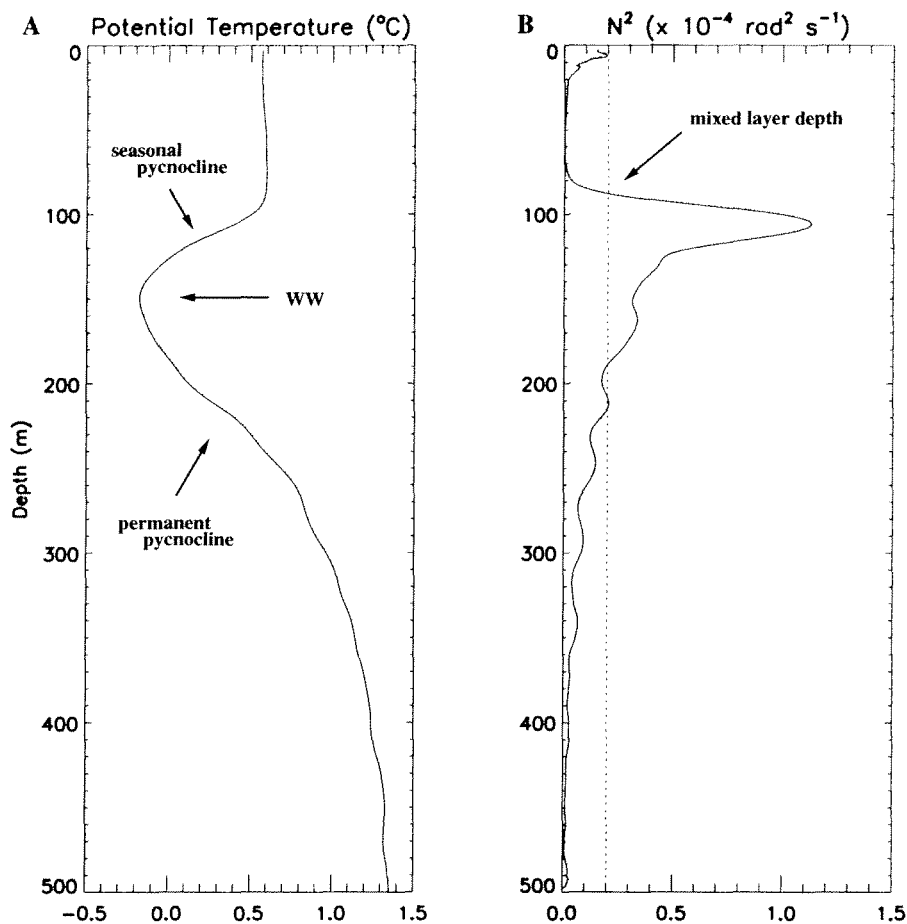
Figure 4. Fall 1993 potential temperature and buoyancy frequency versus depth for the 600.120 station. Vertical profiles of A) potential temperature (°C) and B) buoyancy frequency (N^2) (rad^2 s^{-2}) for the 600.120 station measured during Fall 1993. The temperature minimum indicates the depth of WW. The seasonal and permanent pycnoclines are labeled. The N^2 criteria used to determine mixed layer depths is indicated by the dotted line.
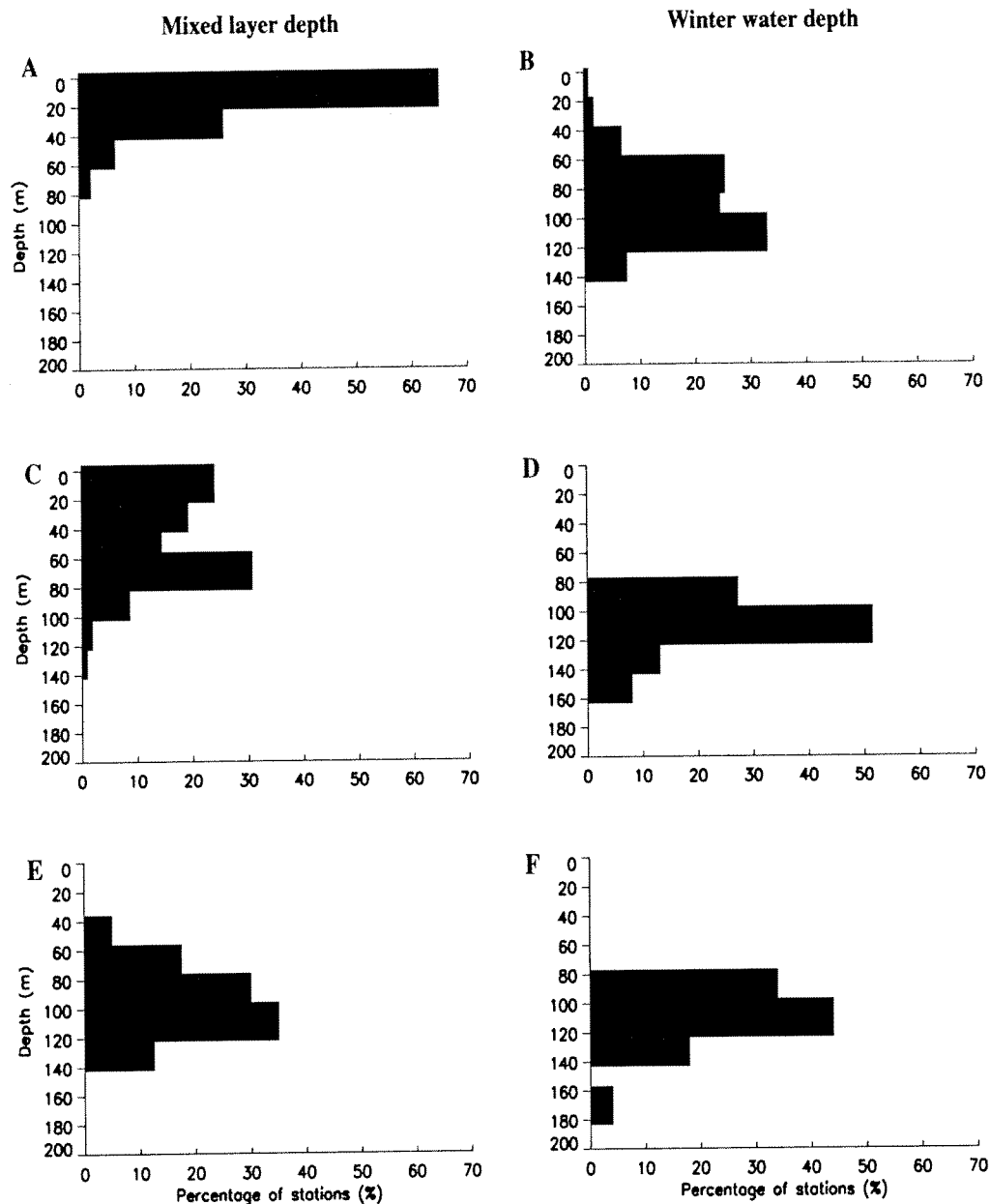
Figure 5. Frequency distributions for the winter water and mixed layer and mixed layer depths. A) Mixed layer and B) winter water depths were obtained from hydrographic observations made in January 1993. Mixed layer depths for C) March 1993 and E) August 1993 and Winter water depths for D) March 1993 and F) August 1993. The depth of the mixed layer is defined by the shallowest depth where the buoyancy frequency (N^2) exceeds 0.2×10^{-4} rad^2 s^{-2}. The analysis is based on all of the summer, fall and winter 1993 temperature and salinity data described in Section 3.1.

tions. The two classes are a warmer (T > 1.6°C) cluster from water on the oceanic side of the shelf break and cooler (1.2 < T < 1.4 °C) found on the shelf (Figure 2). This separation is statistically significant as the temperature mean of each group lies more than one standard deviation from the other mean. Smith et al. [1999] distinguish between these clusters calling the warmer group Upper-CDW (UCDW) and the cooler group modified UCDW. The modified version of UCDW is found over the shelf while unmodified UCDW was found only on the oceanic side of the shelf break and at stations influenced by the ACC. These observation indicate that the boundary of the ACC (thus the separation between UCDW and the modified UCDW) is generally within 20 km of the shelf break with a transition zone on the order of 10 to 25 km wide.

An analysis of historical hydrographic data which covers nearly 90 (1900-1990) years, presented in Hofmann et al. [1996] indicates that the separation between UCDW and the cooler version of UCDW found on the shelf persists over long time scales. Klinck [1998] and Smith et al. [1999] propose that the modified-UCDW is formed, and its hydrographic properties maintained, as UCDW from the ACC moves onto the shelf and looses heat (and salt) to overlying, cooler, fresher Winter Water (WW). Klinck [1998] and Smith et al. [1999] calculate the onshore flux of heat and salt necessary to balance vertical losses through the permanent pycnocline. The horizontal and vertical diffusive balances (Q_h and Q_v in Figure 2, respectively) that contribute to the formation of the modified version of UCDW can be expressed as

$$K_h^T \frac{H}{L} \frac{\partial T}{\partial x} \Big|_{x=sb} - K_v^T \frac{\partial T}{\partial z} \Big|_{z=py} = \frac{1}{\rho_o C_p} I_H$$

$$K_h^S \frac{H}{L} \frac{\partial S}{\partial x} \Big|_{x=sb} - K_v^S \frac{\partial S}{\partial z} \Big|_{z=py} = \frac{1}{\rho_o} I_S \qquad (1)$$

where I_H and I_S are the volume integrated heat and salt changes below the perma-

nent pycnocline and the subscripts *sb* and *py* indicate that the terms are evaluated at the shelf break and across the pycnocline. The vertical and horizontal mixing coefficients for heat (T) and salt (S) are represented by K_v and K_h. In the Smith et al. [1999] study, the balance given by (1) is assumed to apply over the long term, background steady state and therefore assumes that $I_H = I_S = 0$. Klinck [1998] used the above model to examine changes in the sub-pycnocline waters between seasons and evaluated I_H and I_S from observations. Using observed property distributions, Klinck [1998] and Smith et al. [1999] found that the hydrographic signature of modified UCDW on the shelf could be maintained with $K_H^T \sim K_H^S$ with values between 10 and 100 m^{2}s^{-1}. The most consistent balances were found when allowing for differences in the coefficients of vertical diffusion which would occur with double diffusion (i.e. $K_v^S = .1$ to $.3$ K_v^T).

The two layer structure of the west Antarctic Peninsula continental shelf waters, and the formation of a distinctive permanent pycnocline (Figure 2) is different than many mid-latitude shelf systems where well mixed conditions extend throughout the water to the bottom. Klinck [1998] and Smith et al. [1999] speculate that one possible explanation for the oceanic character of the sub-pycnocline shelf waters along the west Antarctic Peninsula is the rather deep shelf which is generally greater than 400 m thus allowing oceanic water to intrude (Figure 1). The lack of cold, dense shelf water may also result from the relatively warm atmospheric conditions and/or the absence of large permanent ice shelves in the region.

2.3 Meteorology and sea ice

Meteorological conditions are important in determining water mass distribution and the dynamics of the mixed layer. Obvious meteorological contributions to mixed layer dynamics are wind driven Ekman circulation and buoyancy forcing from atmospheric fluxes of heat and fresh water. Also, in high latitude systems the atmospheric

heat flux plays a crucial role in sea ice formation.

The surface waters of the west Antarctic Peninsula continental shelf region vary from nearly ice-free ($< 10\%$ coverage) in the austral summer to fully ice covered (nearly 100% coverage) in the austral winter [Stammerjohn and Smith, 1996]. Furthermore, the extent of maximum winter ice cover, and the timing of the advance and retreat of ice, is variable from season to season [Stammerjohn and Smith, 1996], and interannual variability in the extent of winter ice coincide with variations in the mean winter temperatures. These warm and cold atmospheric conditions result in low and high ice years, defined relative to the average ice conditions over time.

Smith et al. [1996] use atmospheric data from Faraday Station to demonstrate that climatic conditions along the western side of the Antarctic Peninsula are characterized as a maritime climate which is generally warmer than the Weddell side. They also indicate that the temperatures exhibit a meridional gradient (especially in the winter) where temperatures along the southern portion of the Antarctic Peninsula are cooler than in the north near the Bransfield Strait. This temperature gradient breaks down in the summer giving way to a more uniform distribution. Smith et al. [1996] also use data from a mid-shelf automatic weather station (AWS) (i.e. located about 100 km from the Antarctic Peninsula near the 600 line) to show that atmospheric conditions differ from onshore to offshore. The differences between onshore and offshore atmospheric conditions is also demonstrated by Klinck and Smith [1995] where station meteorology is compared to ship-based observations during the 1993 LTER fall cruise. Land-based meteorological data (i.e. from Palmer and Faraday) is influenced by local topography (especially the wind data) which may account for a large part of the across-shelf differences. While the mid-shelf data may represent conditions on the shelf more realistically than the station data, the record is rather short (1 year). The mid-shelf data set also contains many data gaps. Because of these problems, data at the peninsula stations will be used in this study.

2.4 Circulation modeling studies for the west Antarctic Peninsula region

2.4.1 Regional modeling studies

Capella [1989] adapted the three-dimensional, primitive equation model of Semtner [1974] to simulate ice-free circulation around the Bransfield Strait and South Shetland Islands. His results indicate a northeastward wind-driven surface flow which is sensitive to seasonal changes in the wind field. He also demonstrates a region of complex circulation near Elephant Island, which most likely results from an interaction of the wind driven flow and the complex bathymetry. Capella [1989] did not include sea ice effects on the circulation and the southern boundary of his model (periodic with the northern boundary) only extended to the northern portion of the west Antarctic Peninsula shelf. Even with these limitations, the general magnitude and direction of the simulated flow fields presented by Capella [1989] provide some context for evaluating the results of this study.

The Fine Resolution Antarctic Model (FRAM) [FRAM Group, 1991; Webb et al., 1991] provides simulated circulation fields for the entire Southern Ocean on a 2.5 by 2.5 km grid and reproduces many of the key circulation features such as the general location and transport of the ACC. However, the simulated circulation for the west Antarctic Peninsula shelf region is questionable [Hofmann et al., 1996]. The realism of the model solutions in this region is affected by the smoothed bathymetry used in the model. The west Antarctic Peninsula shelf bathymetry is poorly represented. Also, the FRAM circulation does not directly include sea ice processes.

2.4.2 Coupled sea ice-ocean models

Sea ice models are generally divided into thermodynamic sea ice models and coupled dynamic-thermodynamic sea ice models. The former predicts sea ice growth and

melting as a function of the imbalance between imposed atmospheric heat fluxes and the calculated heat flux through the ice [Maykut and Untersteiner, 1969; Semtner 1976]. The latter couples ice growth from a thermodynamic model to wind and current-driven ice motion. The most complex sea ice models include the effects of internal ice stress on ice motion and thickness by including a numerical treatment of ice rheology (e.g., Hibler [1979]). However, Hibler [1979] and Ikeda [1989] indicate that rheology is unnecessary for thin, new ice with areal coverage less than 80%, conditions which generally apply to the shelf waters along the West Antarctic Peninsula [Stammerjohn and Smith, 1996].

Coupled sea ice-ocean models of the Weddell Sea [Hibler, 1979; Lemke, 1987; Lemke et al., 1990; Stossel et al., 1990], the Bering Shelf system [Kantha and Mellor, 1989; Mellor and Kantha, 1989] and the Arctic [Häkkinen and Mellor, 1990] have been used to demonstrate the importance of sea ice processes and thermodynamics on circulation and mixed layer at high latitudes. While none of these models specifically address the shelf waters of the west Antarctic Peninsula, the results from these studies are used to formulate models for the region. Specifically, Kantha and Mellor [1989] couple a thermodynamic sea ice model, based on the Semtner [1976] model, to the Mellor and Yamada [1982] level 2.5 (MY2.5) turbulence closure scheme used in the Princeton Ocean Model (POM). The model was later enhanced by Häkkinen and Mellor [1990] and is hereafter referred to as the MKH model. The coupling in the MKH model involves the parameterization of physics in the molecular sub-layer at the ice-water interface, which transfers heat and salt between the ice and ocean models. This parameterization was found to have a significant effect on sea ice thermodynamics. Much of their work provides the basis for the sea ice - mixed layer development in this study.

CHAPTER 3

DATA AND METHODS

This chapter provides details of the datasets, analysis methods and numerical model used to estimate heat budgets and assess the physical processes contributing to the mixed layer structure of the west Antarctic Peninsula shelf waters.

3.1   Data sets

The temperature and salinity data collected from four cruises that occurred on the west Antarctic Peninsula continental shelf along with meteorological data from two land-based stations (Faraday and Palmer) are used to construct regional heat budgets and to initialize and validate a sea ice-mixed layer model. The meteorological data from Faraday Station consists of daily observations of air temperature, relative humidity, atmospheric pressure and wind speed and direction. Sea surface temperatures and solid precipitation records (described in Section 3.4.5) from Palmer Station were also used in the heat budget and sea ice mixed layer model. Meteorological variables from a National Center for Environmental Prediction (NCEP) and National Center for Atmospheric Research (NCAR) 40 year data re-analysis [Kalnay et al., 1996] were used to obtain larger spatial cover. Daily records are limited to the year 1993, but monthly values are reported for the entire 40 year time span. Sea ice concentrations used in this study were derived from the recently re-distributed global sea ice concentration grids from the National Center for Snow and Ice Data Center (NCSID).

3.1.1   Hydrographic data

Between January 1993 and February 1994, portions of the west Antarctic Peninsula shelf were sampled during four cruises (details in Table 1). The fall (March-May) 1993 cruise included the entire area between the 000 and 900 (Figure 1) and provided

Table 1. Season, dates, and region covered for the west Antarctic Peninsula cruises used in this study.

LTER Cruise ID	Season	Dates (dd-month yy)	Lines Sampled
93A	summer	08-Jan 93 to 07-Feb 93	200-600
93B	fall	25-Mar 93 to 15-May 93	000-900
93C	winter	23-Aug 93 to 30-Sep 93	200-600
94A	summer	11-Jan 94 to 07-Feb 94	300-600

the most extensive, synoptic hydrographic observation for the region to date. The 200 through 600 lines were occupied during the summer 1993 (January-February) and the winter 1993 (August-September). During the summer of 1994, the 300 through 600 lines were occupied providing hydrographic data for two consecutive summer seasons.

On all cruises, conductivity-temperature-depth (CTD) measurements were made with a 20 km across-shelf resolution using a SeaBird CTD mounted on a Bio-Optical Profiling System (BOPS) [Smith, 1984] to within 20 m of the bottom, or to 500 m in deeper water. On the fall 1993 cruise, a SeaBird 911$^+$ was also deployed to obtain 10 km resolution in hydrographic properties. During the fall cruise, CTD casts were made to depths of 20 m above the bottom, or to 4000 m for deeper water. Water samples were taken at discrete depths and analyzed for salinity with a Guideline Salinometer calibrated with IAPSO standard sea water. During the fall cruise, frequent cross-sensor comparisons were made. Additionally, pre- and post-cruise calibrations were made by SeaBird Electronics. No significant sensor drift was determined in time or with depth; thus, no corrections were made to the original data. Derived data products were calculated using algorithms given in UNESCO [1993]. Full details on data collection and processing for each cruise are given in Klinck et al. [1994], Lascara et al. [1993a, 1993b] and Smith et al. [1993a, 1993b].

3.1.2 Meteorological and radiation data from Faraday Station

Atmospheric observations from Faraday Station, made by British Antarctic Survey (BAS) personnel, are archived at the University of Wisconsin. The Faraday data are the longest, most consistent and highest quality measurements of atmospheric conditions for the region to the west of the Antarctic Peninsula. The data span the years from 1957 to 1993 and include observations of dry and wet bulb air temperatures (°C), cloud cover (%), wind speed (m s^{-1}), wind direction (° from N), relative humidity (%) and atmospheric pressure at the sea level (mb) taken at 3 hour intervals. Details on BAS data sets, collection techniques, data processing and sensor calibrations can be found in Jones and Limbert [1987]. The Faraday observations were used to calculate daily averages for all meteorological parameters which were used to estimate surface fluxes of heat and salt. These fluxes are also used as input to the sea ice-mixed layer model. Observations of surface radiation, including hourly records of total short wave radiation (W m^{-2}), are available from BAS for the years of 1985 through 1993.

Estimation of the flux of short wave radiation at the ocean's surface are needed in the calculation of the surface, ice free heat budget (Section 3.2) and for input into the sea ice-mixed layer model (Section 3.3). The contribution of short wave radiation to the heat budget is estimated by applying a cloudiness factor derived by Laevastu [1960] to the clear-sky, geometric model of Zillerman [1972].

The equation for clear-sky, short wave radiation (Q_{sw}^{clear}) (W m^{-2}) is

$$Q_{sw}^{clear} = \frac{S_c \, cos^2 Z}{10^{-5}(cos Z + 2.7)e_A + 1.085 \, cos Z + 0.1} \tag{2}$$

where S_c (Table 2) is the solar constant and e$_A$ is the atmospheric vapor pressure (calculated from relative humidity). The cosine of the solar zenith angle (Z) is given by

$$cos Z = \; sin \, \phi \; sin \, \gamma \; + \; cos \, \phi \; cos \, \gamma \; cos \, \Psi \tag{3}$$

where ϕ is latitude (ϕ=65°S in this study). Solar declination (γ) and the hour angle (Ψ) are given, respectively, by

$$\gamma = 23.44° \; \cos\left[360°(172 - year\ day)/365\right] \qquad (4)$$

and

$$\Psi = 15° \; (12 - solar\ time) \qquad (5)$$

Total short wave flux at the surface (Q_{sw}) is then estimated by reducing Q_{sw}^{clear} (2) by a cloudiness factor [Laevastu, 1960].

$$Q_{sw} = Q_{sw}^{clear} \left(1 - 0.6 \; C_t^3\right) \qquad (6)$$

where C_t is cloud cover in tenths of sky obscured.

The short wave radiation record at Faraday is a direct measurement at the earth's surface and contains information about the clouds thus providing an excellent record to verify and calibrate the cloudiness correction and the clear-sky model. Comparisons between calculated short wave radiation and the direct measurements from Faraday (Figure 6) indicate that (2) and (6) accurately reproduce the time variability of the short wave radiation at this location. The model-data comparison (Figure 6) indicates that, no tuning of these equations is necessary and therefore the simulated short wave radiation time series was used as input to the sea ice-mixed layer model.

3.1.3 Sea surface temperature near Palmer Station

A daily record of sea surface temperatures (SST) for the waters surrounding Palmer Station for the years 1992-1994 was calculated by combining surface data from ship observations near Palmer Station (50 km radius) with records obtained from an AWS located at Bonaparte Point (65°15'S, 64°15'W). This combined data set was averaged to give daily values. Quadratic curves were fit to the spring, summer and

A

B
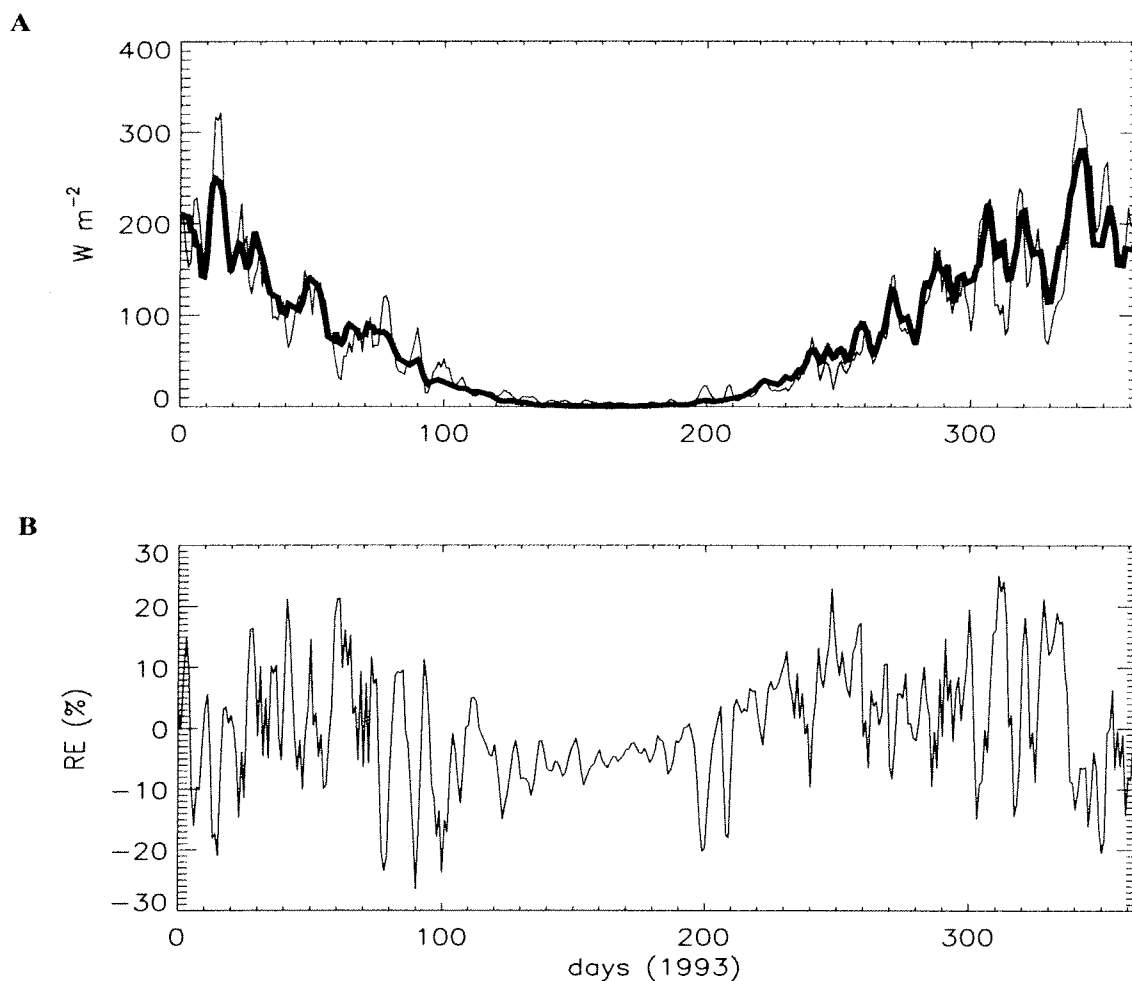
Figure 6. Comparison of calculated and measured surface, short wave radiation flux. A) Comparison between the short wave radiation flux (W m^{-2}) calculated from the Zillerman [1972] and Laevastu [1960] equations (thick line) and a direct measurements made at Faraday Station (thin line). Measured and calculated averages for the year are 84 and 82 W m^{-2}, respectively. B) Relative error (RE) for measured and calculated short wave radiation fluxes (Q_{sw}^{meas}, Q_{sw}^{calc}). RE= 100.*(Q_{sw}^{calc}-Q_{sw}^{meas})/ ($Q_{sm_7}^{meas}$), where $Q_{sm_7}^{meas}$ is the measured short wave radiation data smoothed with a 7 point smoother. The average RE=-1.3 %.
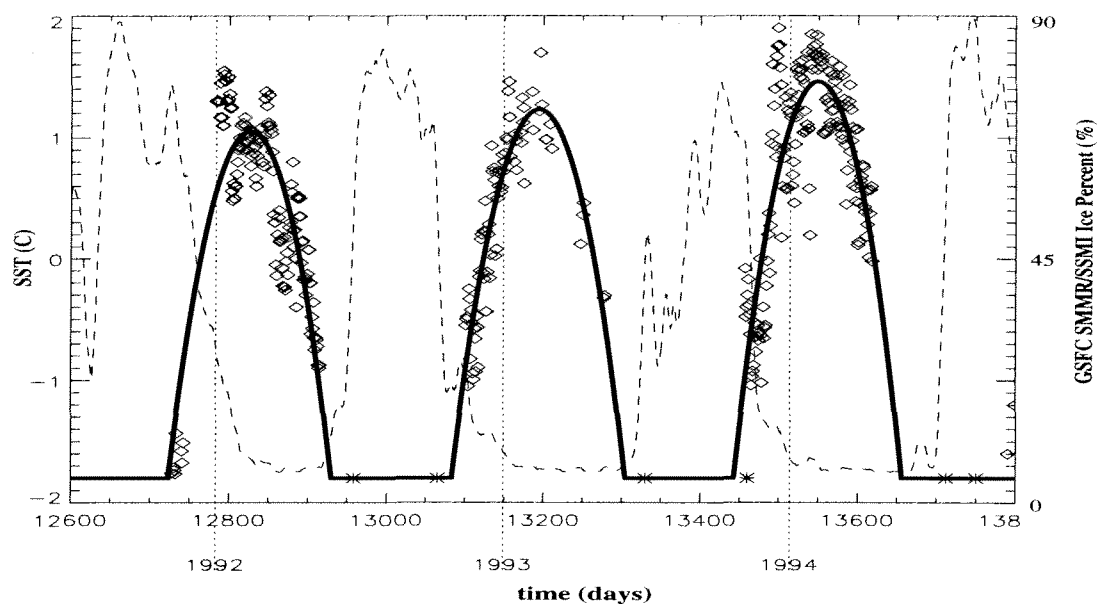
Figure 7. SST record for the Palmer Basin (50 km radius around Palmer Station) for 1992-1994. Diamonds indicate daily average surface temperatures computed from Bonaparte Point AWS and surface temperature and salinity from ship observations. The thick solid line represents a curve fit to the data. The dashed line is the GSFC SMMR/SSMI derived sea ice concentration which are used to set the SST to the freezing point of sea-water with salinities typical of those along the west Antarctic Peninsula shelf (SST=-1.9°C). The x-axis represents the Julian day since January 1, 1957 (January 1 of each year are indicated with vertical dotted lines).

fall observations to produce a continuous daily record. Winter SST conditions were assumed to be freezing (T_f=-1.9°C) during times when satellite-derived (Section 3.1.5) sea ice distributions indicated that the region around Palmer Station had at least 20% ice cover. The daily averaged SST observations and the resulting continuous SST record, along with the satellite derived ice fields used to determine winter SST's, are presented in Figure 7. The diamonds in the figure represent the daily observations while the solid black line represents the derived SST record. Periods of constant SST at the freezing point coincide with periods of ice cover (as indicated by the dashed line). Summer SST's range between 1 and 2 °C. These summer temperatures are consistent with the observations the inner-station data presented in Smith et al. [1999]. The smooth SST curves produced by this method averages over high frequency variability observed in the daily observations; however, this method is conservative and does not produce false peaks associated with more elaborate methods of producing continuous daily records (e.g. spline fitting techniques). The fitted SST data appear to underestimate the summer peak temperatures; however, it will be shown in Section 4.1.2 that the total heat budget is not very sensitive to the choice of SST.

3.1.4 Meteorological data from the NCEP/NCAR reanalysis project

A globally gridded (2.5×2.5°) atmospheric data set from a joint project between the National Center for Environmental Prediction (NCEP) and the National Center for Atmospheric Research (NCAR) provides various atmospheric parameters on 17 different pressure levels (including sea-level) for a 40 year (1957-1996) time span [Kalnay et al., 1996]. Their global reanalysis model assimilates global distributions of land-based and ship based meteorological observations. An advantage of this technique, described in Kalnay et al. [1996], is that the numerical procedure remained essentially unchanged during the entire analysis eliminating apparent climate shifts

which arise from using various techniques during a simulation.

Daily atmospheric data for the 1993 and monthly averages for the entire simulation were obtained from NCEP and NCAR for use in this study. Daily values are available for the entire 17 year simulation but such detailed analysis was beyond the scope of this study. Atmospheric pressure (mb) and air temperature (°C) at sea level were extracted for a geographic region around Drake Passage (10° to 180°W and 30° to 85°S) and were used to identify larger-scale spatial patterns which may affect interpretations of ocean heat and sea ice budgets (Section 5.2).

3.1.5 Sea ice from the SMMR and SSMI

A 17-year record of sea ice concentrations for the west Antarctic Peninsula shelf was extracted from the National Snow and Ice Data Center (NSIDC) archives [Cavalieri et al., 1997]. The NSIDC data is a combination of three previous data sets which have been cross-calibrated at NASA Goddard Space Flight Center (GSFC) [Comiso et al., 1997]. This record is the longest, most continuous global record of sea ice distributions to date. The individual sea ice records are from the Nimbus 7 Scanning Multichannel Microwave Radiometer (SMMR) satellite which operated from October 1978 to August 1987. The second and third records are derived from the Defense Meteorological Satellite Program's Special Sensor Microwave/Imager satellite (F8 and F11 SSM/I), providing data coverage from July 1987 to December 1991 and from December 1991 to September 1995, respectively. Comiso et al. [1979] use time overlaps to cross-calibrate the individual time series. These calibrated data are referred to as either the GSFC SMMR/SSMI sea ice record or the observed ice fields when used in this study.

The equal area (625 km^2) GSFC SMMR/SSMI sea ice grid in the vicinity of the west Antarctic Peninsula is illustrated in (Figure 8). This grid consists of sea ice data with east-west and north-south positions given by i and j locations, respectively.
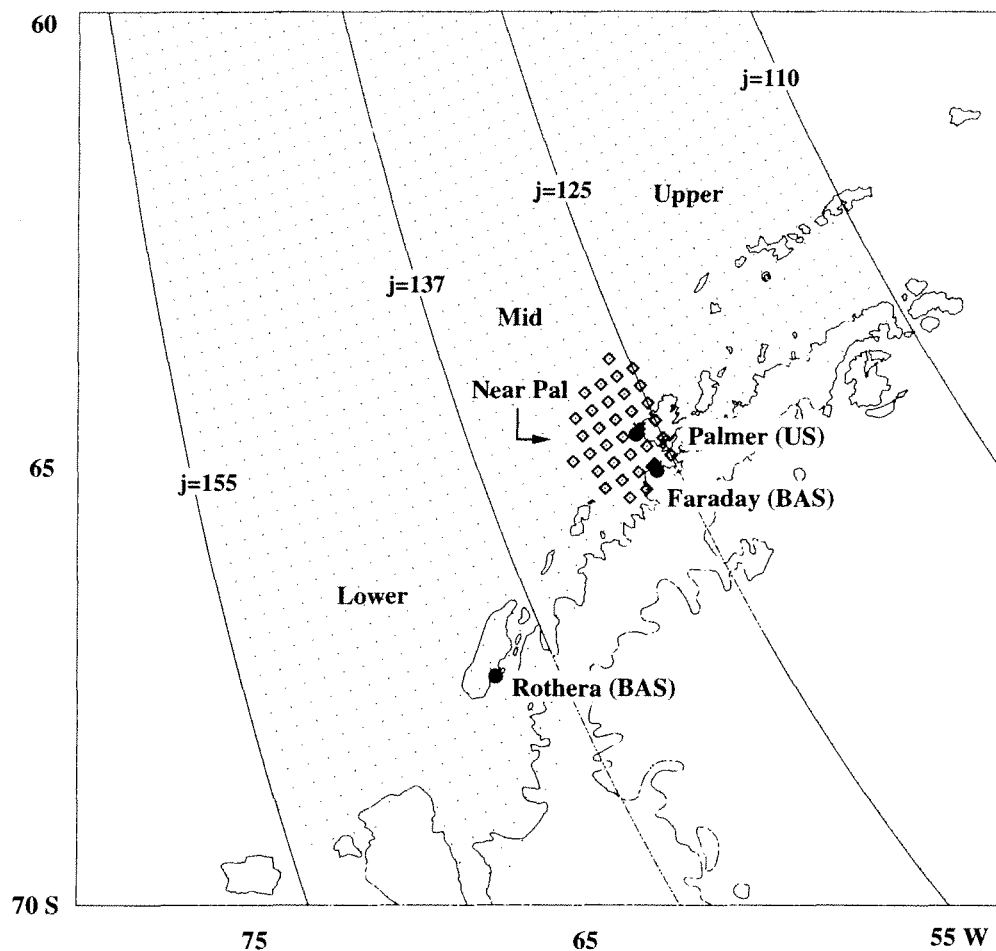
Figure 8. The west Antarctic Peninsula and the GSFC SMMR/SSMI sea ice concentration grid (indicated with dots). The GSFC SMMR/SSMI grid is an equal area grid (625 km^2) with east-west and north-south gird locations given by i and j indexes, respectively. The j index is used to define the northern (j=110) and southern (j=155) boundaries of the grid for use along the west Antarctic Peninsula. Similarly, lines of constant j index are used to partition the region into a lower-, mid- and upper-region. GSFC SMMR/SSMI data locations within 50 km of Palmer Station are indicated with diamonds.

The GSFC grid is area preserving and the i,j pairs do not correspond to consistent longitude and latitude locations, thus resulting in the distortion noticed in Figure (8) when projecting the GSFC SMMR/SSMI grid onto the cylindrical map used to represent the west Antarctic Peninsula shelf.

The northern and southern extent for data extracted for use in constructing a west Antarctic Peninsula shelf time series are given by GSFC SMMR/SSMI j indexes of $j = 155$ (south) and $j=110$ (north), respectively (Figure 8). The eastern extent of the region is defined by the Antarctic Peninsula. No offshore (westward) grid extent was specified, which allows all sea ice between the peninsula and the ice edge to be included in the analysis.

Sea ice area for a given cell ($A_i^{(i,j)}$) is calculated by multiplying the percentage ice cover for the cell by its total area (i.e. 625 km^2 for all cells). For a given day, the total ice area for the west Antarctic Peninsula region by summing all $A_i^{(i,j)}$ over the grid presented in Figure (8) bounded by the j indices described above. The time series for ice area (Figure 9b) is then produced by repeating the above summation for all daily records in the GSFC SMMR/SSMI record.

In addition to the total sea ice area for the west Antarctic Peninsula, 4 sub-sets of sea ice time series were extracted to give information for different regions along the shelf as well as near Palmer (Figure 8). The north-south GSFC SMMR/SSMI grid index (i.e. j index) is used to define these sub-sets as follows: lower [138 < j < 155], middle [126 < j < 137] and upper [138 < j < 155] regions (Figure 8). In addition to total ice record and the lower-, mid- and upper- regions, a near-Palmer record consisting of data within 50 km of Palmer Station (indicated with diamonds in Figure 8) was also extracted. The near Palmer record is used frequently to compare model derived sea ice to observations.

Smith et al. [1996] compares a similar sea ice record to air temperatures recorded at Faraday Station and concludes that there is a relationship between cold/warm

wintertime atmospheric temperatures and high/low ice years. This result is quantitatively similar to trends observed in (Figure 9) with high ice years in 1980 and 1987 corresponding to cold air temperatures. The lowest ice year on record (1989) corresponds to the winter with the warmest atmospheric conditions. These relationships will be investigated further in this study.

3.2   AASW heat flux calculation

The total heat and salt budget for AASW (schematically represented in Figure 2) include surface fluxes through the atmosphere-AASW interface, ice-AASW interface and vertical fluxes through the permanent pycnocline.

The surface heat budget for the AASW layer west Antarctic Peninsula is calculated by assuming that through ice heat fluxes are negligible when compared to the heat fluxes in the open-water, ice-free regions (i.e. $Q_{open} > Q_{ice}$ in Figure 2). Under this assumption, the total heat flux is represented by the ice-free budget which is calculated by combining bulk aerodynamic estimates of latent and sensible heat fluxes (Section 3.2.1) with contributions from short- and long-wave radiation. The short- and long-wave radiation budgets are calculated from geometric equations commonly used in numerical modeling studies (e.g. Parkinson and Washington [1979]) (Section 3.1.2 and 3.2.1).

Vertical heat and salt fluxes from warm, salty sub-pycnocline waters found at depth along the shelf are estimated using the double diffusive model presented by Marmorino and Caldwell [1976] (MC76 model) (Section 3.2.2). Klinck [1998] and Smith et al. [1999] indicate the transfer of heat and salt through the permanent pycnocline is enhanced, and possibly governed, by process of double diffusion.

The AASW heat budget described above only accounts for vertical processes at the atmosphere-AASW interface and vertical fluxes of heat through the permanent pycnocline. Horizontal contributions of heat and salt (i.e. Q_{sur} in Figure 2) are
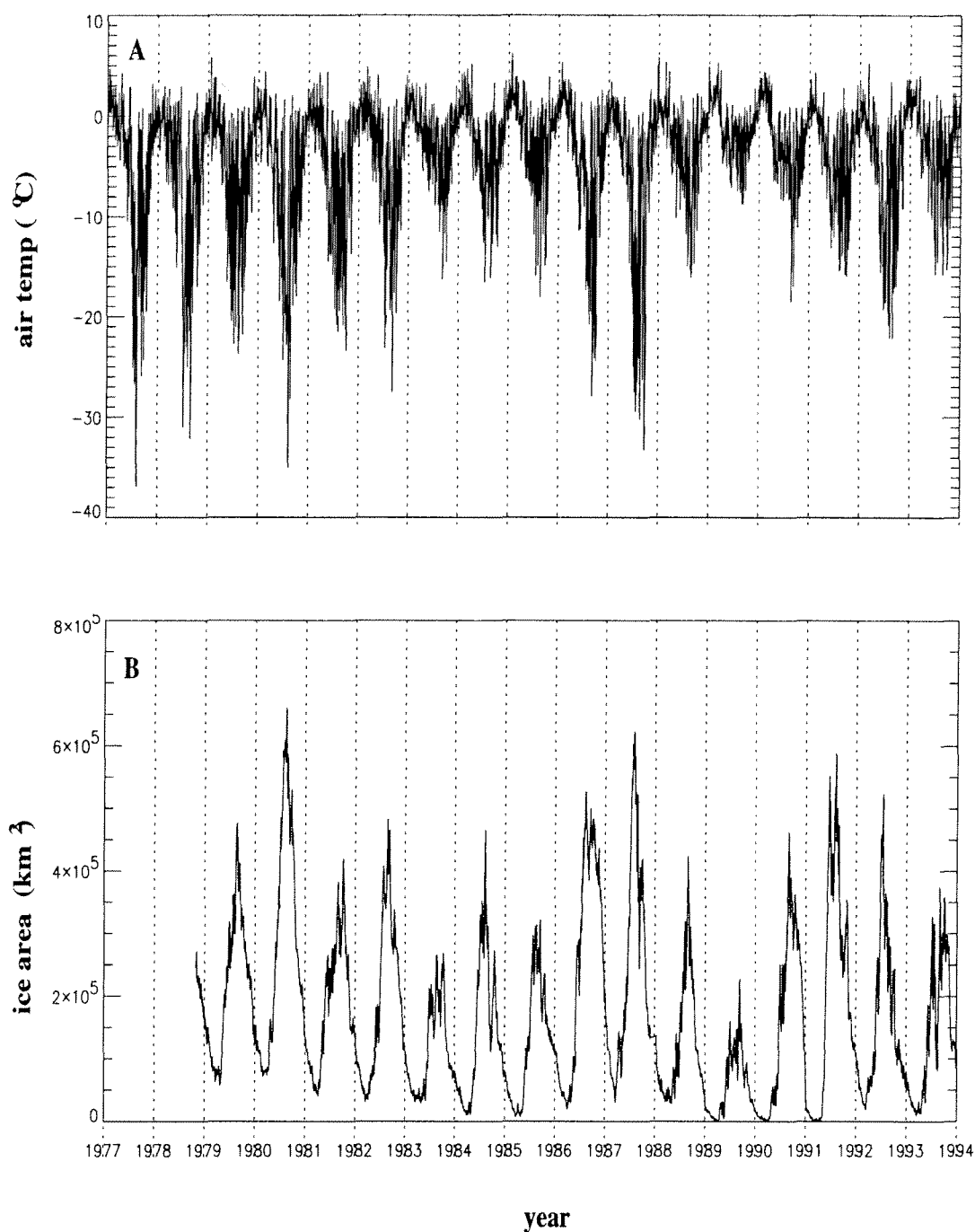
Figure 9. A) Air temperatures observed at Faraday Station and B) Extracted GSFC SMMR/SSMI sea ice time series. Vertical dotted lines indicate January 1 of each year.

not included in the calculation. These processes will be addressed in the modeling portion of the study along with the contribution of heat fluxes at the sea ice-AASW interface (Section 3.4.5) which are also neglected in this ice-free calculation.

3.2.1 Surface, ice-free heat flux calculation

The total heat exchange (Q_{tot}) (W m^{-2}) across the air-sea ice interface is estimated as

$$Q_{tot} = (1 - A_i)Q_{open} + A_i \cdot Q_{ice} \tag{7}$$

where Q_{open} is the ice-free, open ocean heat exchange, Q_{ice} represents heat exchanges through the sea ice and A_i is the ice concentration obtained from the daily, near-Palmer GSFC SMMR/SSMI ice record (Section 3.1.5). The determination of Q_{open} is fairly straightforward and involves using observations of meteorological and oceanic data. Estimating Q_{ice} requires measurements of ice thickness (h_i), the skin temperature of ice and surface albedo and which are not commonly available.

In high latitude systems, open ocean heat fluxes are often orders of magnitude greater than through-ice heat fluxes even in regions characterized by 98% ice cover [Parkinson and Washington, 1979]. Thus, an initial estimate for the regional heat budget for the shelf waters will assume that the ice acts as a perfect insulator blocking all heat transfer between the ocean and atmosphere (i.e. $Q_{ice} = 0$). This assumption will be relaxed, and evaluated, in the modeling section of the study where through ice heat fluxes are calculated.

Assuming that heat exchanges through the ice are zero, the ice-free flux at the air-sea interface (Q_{tot}) can then be estimated as

$$Q_{tot} = (1 - A_i) \cdot [(1 - \alpha_s) \cdot Q_{sw} + \epsilon \cdot (Q_{lw}^{back} - Q_{lw}^{down}) + Q_{sens} + Q_{lat}] \tag{8}$$

where Q_{sw} represents the heat input into the surface water from total incoming short wave radiation, given by equations (2) and (6), and α_s is the surface albedo (Table 2).

The upward longwave radiation (Q_{lw}^{back}) is calculated from the Stefan-Boltzmann relationship

$$Q_{lw}^{back} = \sigma \left(SST + 273\right)^4 \tag{9}$$

where ϵ is the surface emissivity and σ is the Stephan-Boltzmann constant (Table 2). Daily sea surface temperatures from near Palmer Station were used to specify SST (Section 3.1.3).

Incoming longwave radiation (Q_{lw}^{down}) is estimated from air temperature, T_{air} (°C) and cloud cover, C_l.

$$Q_{lw}^{down} = \sigma \left(T_{air} + 273\right)^4 \cdot \left(0.7855 + 0.2232 \cdot C_l^{2.75}\right) \tag{10}$$

Sensible heat exchange (Q_{sens})is estimated with a bulk aerodynamic formula for heat transfer

$$Q_{sens} = \rho_a C_{pa} C_{HO} W \left(T_{sst} - T_{air}\right) \tag{11}$$

where c_{pa} and ρ_a are the specific heat of air at constant pressure and the density of air, respectively and W is the wind speed (m s^{-1}) The heat transfer coefficient (C_{HO}) (Table 2) is chosen to be consistent with the MKH model.

Latent heat exchange (Q_{lat}) is calculated from

$$Q_{lat} = \rho_a L_v C_{HO} W \left(q_o - q_A\right) \tag{12}$$

where L_v is the latent heat of vaporization, q_A and q_o are the specific and the saturated specific humidities, respectively.

3.2.2 Double diffusive heat and salt flux

A second source of heat and salt to AASW is the relatively warm, salty, sub-pycnocline waters found below 100 m on the shelf to the west of the Antarctic Peninsula [Hofmann and Klinck, 1998] (c.f. Figure 2). These waters are a modified version of oceanic UCDW and are consistently found along the shelf. The

Table 2. Constants used in the heat flux calculations and numerical model.

Symbol	Variable Name	Value
ρ_a	density of air	1.3 kg m^{-3}
ρ_i	density of ice	900 kg m^{-3}
ρ_o	density of water	1028 kg m^{-3}
g	gravitational acceleration	9.8 m s^{-2}
k_i	thermal conductivity (ice)	2.04 J m^{-1} s^{-1} K^{-1}
k_s	thermal conductivity (snow)	0.33 J m^{-1} s^{-1} K^{-1}
L_v	latent heat of vaporization	2.501×10^6 J kg^{-1}
L_f	latent heat of fusion	3.347×10^5 J kg^{-1}
k_t	molecular diffusivity (heat)	1.4×10^{-7} m^2 s^{-1}
k_s	molecular diffusivity (salt)	1.1×10^{-9} m^2 s^{-1}
C_{pa}	specific heat of air	1004 J K^{-1} kg^{-1}
C_{po}	specific heat of water	3990 J K^{-1} kg^{-1}
α_s	surface albedo (ocean)	0.10
α_i	surface albedo (ice)	0.64
α_{sn-w}	surface albedo (wet snow)	0.73
α_{sn-d}	surface albedo (dry snow)	0.82
ϵ	surface emissivity	0.97
S_c	Solar constant	1353 W m^{-2}
σ	Stephan-Boltzmann constant	5.67×10^{-8} W m^{-2} K^{-4}
C_{HO}	transfer coefficient (ocean-air)	1.5×10^{-3}
C_{HI}	transfer coefficient (ice-air)	$2.0 \times C_{HO}$
ν	viscosity	1.8×10^{-6} m^2 s^{-1}

magnitude of the fluxes of heat and salt from the modified UCDW to the base of
AASW was first investigated using a simple box model [Smith et al., 1999] which
indicated that double diffusion may play an important role in the vertical transfer
of heat (primarily) and salt (slightly). In many high latitude systems where cold,
fresh water overlies warm, salty water, double diffusion enhances the vertical trans-
fer of heat and salt. The double diffusive instability results when the temperature
contribution to the density profile is unstable but static stability is provided by the
vertical distribution of salinity [Turner, 1973].

Indicators of the potential importance of the double diffusive instability are the

density ratio (R_ρ) and its related diagnostic, the Turner angle (Tu).

$$R_\rho = \beta S_z \cdot (\alpha T_z)^{-1}$$
$$Tu = \frac{180°}{\pi} \, tan^{-1} \left(\frac{1 + R_\rho}{1 - R_\rho} \right) \tag{13}$$

where T_z (°C m^{-1}) and S_z (psu m^{-1}) are the vertical derivative of temperature and salinity, respectively and α (°C^{-1}) and β (psu^{-1}) are the thermal expansion and haline contraction coefficients, respectively. These two diagnostics measure the relative importance of the stabilizing effect of salinity to the destabilizing effect of temperature.

Values of $R_\rho > 1$ (and $Tu <$ -45°) indicate that conditions in the region favor the double diffusive instability and increased vertical fluxes of heat and salt are expected [Kelly, 1984]. For oceanic temperatures and salinities sampled on the shelf along the west Antarctic Peninsula shelf, the coefficient of haline contraction about 15 times that of thermal expansion (i.e. $\frac{\beta}{\alpha} \sim 15$). Given typical temperature and salinity differences across the 100 m thick pycnocline of 3.5°C (0.035 °C m^{-1}) and 0.5 (.005 psu m^{-1}), respectively, a typical density ratio for the region is 2.5 ($Tu \sim$ -65°).

With the potential for double diffusion established by $R_\rho > 1$, several models exist to estimate the associated transfer of heat and salt. These models are based on laboratory observations [Turner 1973] that the heat transfer across a double diffusive interface is proportional to the temperature difference raised to the four-thirds power ($\Delta T^{\frac{4}{3}}$). A common $\Delta T^{\frac{4}{3}}$ model, proposed by Marmorino and Caldwell [1976] (MC76), estimates vertical fluxes of heat (Q_{dd}) across a double diffusive interface with the following empirical relationship

$$Q_{dd} = 0.00859 \, \rho_o \, C_{po} \, \alpha^{-1} \cdot (g \, k_t^2 \, \nu^{-1})^{\frac{1}{3}}$$
$$\cdot exp\left\{ 4.6 \, exp\left[-0.54 \cdot (R_\rho - 1) \right] \right\} \cdot (\alpha \Delta T)^{\frac{4}{3}} \tag{14}$$

where ρ_o is the mean density, C_{po} is the specific heat of water, k_t is the molecular diffusivity for heat and g is the acceleration due to gravity (Table 2). A comparison of the MC76 to several other $(\Delta T^{\frac{4}{3}})$ models and a review of the double diffusive process are presented in Robertson et al. [1995].

It is convenient to express the double diffusive heat flux calculated by (14) in terms of its related mixing coefficient (K_{dd}^T). The double diffusive mixing coefficient can be found by solving

$$K_{dd}^T = Q_{dd} \left(\rho_o \ C_{po} \frac{\partial T}{\partial z} \right)^{-1} \tag{15}$$

A mixing coefficient for salt can be found using a relationship from Large, McWilliams and Doney (LMD) [Large et al., 1994] as follows

$$K_{dd}^S = \begin{cases} (1.85 - 0.85 R_\rho) \ K_{dd}^T R_\rho^{-1} & \text{when} \quad 1 > R_\rho > 2 \\ 0.15 \ K_{dd}^T R_\rho^{-1} & \text{when} \quad R_\rho > 2, \end{cases} \tag{16}$$

and is illustrated in Figure 10.

For typical pycnocline temperature and salinity values along the west Antarctic Peninsula, (14) gives a double diffusive heat flux (Q_{dd}) of about 10 W m^{-2}, which equates to a mixing coefficient (K_{dd}^h) of 5×10^{-5} m^2 s^{-1}. For density ratios characteristic of the west Antarctic Peninsula shelf waters, the typical mixing coefficient for salinity is significantly smaller than that for heat (i.e. $K_{dd}^s \sim 3 \times 10^{-6}$ m^2 s^{-1} for $R_\rho = 2.5$), a result typical of the double diffusive instability.

Given the potential importance of the double diffusive process along the west Antarctic Peninsula, its heat and salt transfer through the pycnocline will be considered when calculating ice-free heat budgets. The process will also be included in the modeling study. A full double diffusive heat flux calculation is presented in Section 4.1.3 for the 600.120 station.

3.3   Thermodynamic ice-ocean model

The thermodynamic ice-ocean model developed for this study is used to examine the role of vertical heat and salt fluxes on the seasonal evolution of the mixed
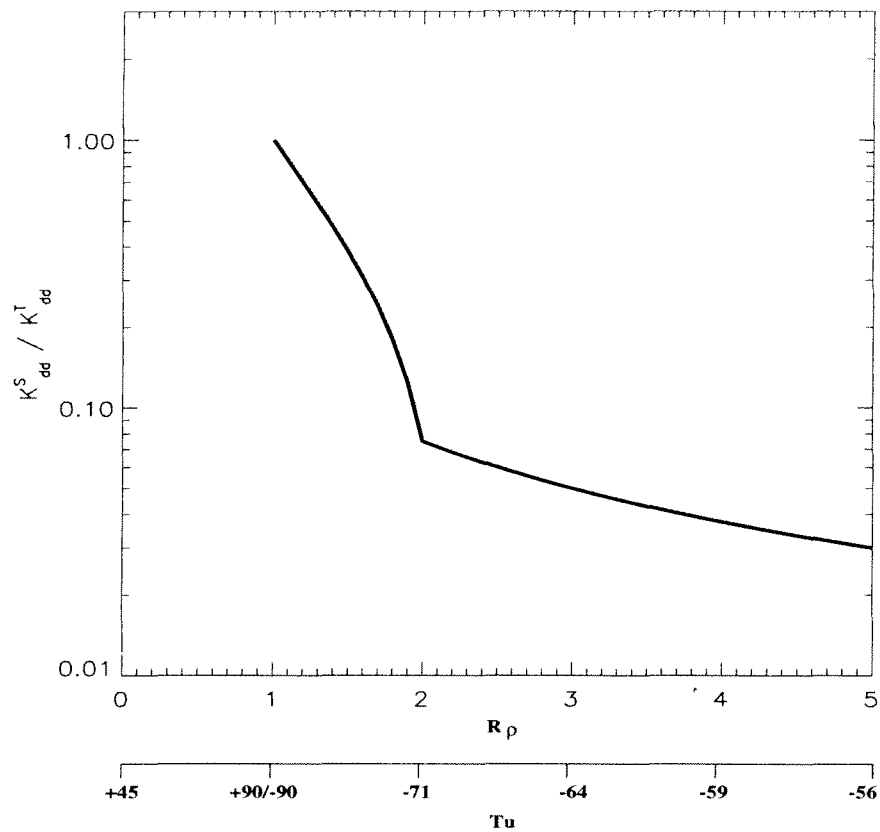
Figure 10. Double diffusive mixing coefficient K_{dd}^S (salt), normalized by K_{dd}^T (heat), as a function of the density ratio. Tu is indicated along the x-axis. For density ratios typical of those calculated for the shelf to the west of the Antarctic Peninsula (i.e. $R_\rho \sim 2$ to 2.5), $K_{dd}^S < 0.10\ K_{dd}^T$.

layer. In particular, the model will calculate the density structure of AASW as it reacts to surface fluxes of heat and salt, which are calculated as discussed in the previous section. A description of the equations of motion and the equations for oceanic temperature and salinity are presented in Section 3.3.1 while the ice model is described in Section 3.4. Numerical details such as vertical grid spacing, time stepping and numerical solution techniques are discussed in Section 3.5 for the entire ice-ocean model.

3.3.1 Ocean model equations

The ocean model is based on the vertical portion of the Princeton Ocean Model (POM) [Mellor, 1993; and Blumberg and Mellor, 1987], which includes prognostic equations for current velocity, temperature, and salinity. The Mellor-Yamada level 2.5 turbulence closure scheme (MY2.5) provides time dependent vertical mixing coefficient for momentum and scalar properties (K_m and K_h), respectively.

The governing equations for horizontal momentum (u,v) are

$$\frac{\partial(u,v)}{\partial t} = f(v,-u) + \frac{\partial}{\partial z}\left[(K_m + K_m^{Ri_g}) \frac{\partial(u,v)}{\partial z} \right] \tag{17}$$

where K_m is the time-dependent, turbulent mixing coefficient for momentum from the MY2.5 turbulence scheme, and $K_m^{Ri_g}$ is a gradient Richardson number parameterization of mixing resulting from shear instabilities. This last process is an enhancement to the standard mixing scheme of POM and is described in Section 3.3.2.

The equations for time and vertical temperature (T) and salinity (S) structure are:

$$\frac{\partial T}{\partial t} = \frac{\partial}{\partial z}\left[(K_h + K_h^{Ri_g} + K_{dd}^T) \frac{\partial T}{\partial z} \right] + F_T^{nudge} \tag{18}$$

$$\frac{\partial S}{\partial t} = \frac{\partial}{\partial z}\left[(K_h + K_h^{Ri_g} + K_{dd}^S) \frac{\partial S}{\partial z} \right] + F_S^{nudge} \tag{19}$$

where K_h and $K_h^{Ri_g}$ are the MY2.5 turbulent, and gradient Richardson, mixing coefficients, respectively, for heat and salt. The differential transfer of heat and salt through the permanent pycnocline by double diffusion (Section 3.2) may be important along the west Antarctic Peninsula shelf, so this process is parameterized in the model by K_{dd}^T and K_{dd}^S (details are presented in Section 3.3.4). Given the vertical representation of the ocean model used in this study, (18) and (19) do not directly include the process of upwelling on the distribution of temperature and salinity. Such a process would have to be directly imposed or assumed to be part of the background diffusion. However, there is no significant lifting observed in the across-shelf density structure [Hofmann and Klinck, 1998; Smith et al., 1999] which would indicate that persistent upwelling is occurring in the region. Thus, the process of upwelling is not directly included in the model.

The last terms in (18) and (19) allow the simulated temperature and salinity to be forced back to a specified climatology. These terms prevent drift in the hydrographic structure of the sub-pycnocline waters which would occur in the absence of horizontal processes. This relaxation scheme and the relaxation time used is explained in Section (3.3.5).

3.3.2   Level 2.5 turbulence closure scheme

Full details on the MY2.5 turbulence closure scheme are presented in Mellor and Yamada [1974]. A brief overview is presented here as a reference.

The MY2.5 turbulence scheme provides time and space dependent turbulent mixing coefficients for momentum and scalar properties such as temperature and salt (K_m and K_h, respectively) by equating $(K_m, K_h) = ql(S_m, S_h)$, where S_m and S_h are derived stability factors and are geometrically determined from properties in the fluid (e.g., vertical momentum and density structures). The MY2.5 scheme requires tracking two additional prognostic variables: twice the kinetic energy (q^2) and the

turbulence macroscale (l). Equations similar in form to (18) and (19) (without the enhancements from double diffusion and gradient Richardson mixing) are used to solve for q^2 and l.

3.3.3 Gradient Richardson mixing

A deficiency of all turbulence closure schemes is their inability to realistically represent mixing in highly stratified conditions [Large et al., 1994; Kantha and Clayson, 1994]. This problem is significant in conditions with melting ice, which introduces a very thin layer of fresh water which then warms with surface heating, and stabilizes the top of the water column.

Kantha and Clayson [1994] include a mixing scheme which parameterizes shear induced instabilities and the breaking of internal waves in an attempt to remove limitations of the MY2.5 scheme. This scheme depends on the gradient Richardson number,

$$Ri_g = N^2 \left(\left(\frac{\partial u}{\partial z} \right)^2 + \left(\frac{\partial v}{\partial z} \right)^2 \right)^{-1} \tag{20}$$

where N is the buoyancy frequency (rad s^{-1}) and u and v are the horizontal components of velocity. The scheme calculates $K_m^{Ri_g}$ based on the gradient Richardson number as follows

$$K_m^{Ri_g} = \begin{cases} \alpha_b & \text{when } Ri_g > Ri_c \\ \alpha_b + 5 \times 10^{-3} \cdot \left[1 - \left(\frac{Ri_g}{Ri_c} \right)^2 \right]^3 & \text{when } 0 < Ri_g < Ri_c \\ \alpha_b + 5 \times 10^{-3} & \text{when } Ri_g < 0, \end{cases} \tag{21}$$

where α_b is a constant background diffusivity and is set to 10^{-5} m^2 s^{-1} for momentum and 10^{-6} m^2 s^{-1} for temperature and salinity [Kantha and Clayson, 1994].

As in the Kantha and Clayson [1994] study, Ri_c=0.7 is defined as the critical Richardson number. At Richardson numbers greater than the critical value, $K_m^{Ri_g}$ reduces to a constant background diffusivity (α_b) used in the standard POM mixing scheme. Richardson mixing coefficients for scalar properties ($K_h^{Ri_g}$) in (18) and
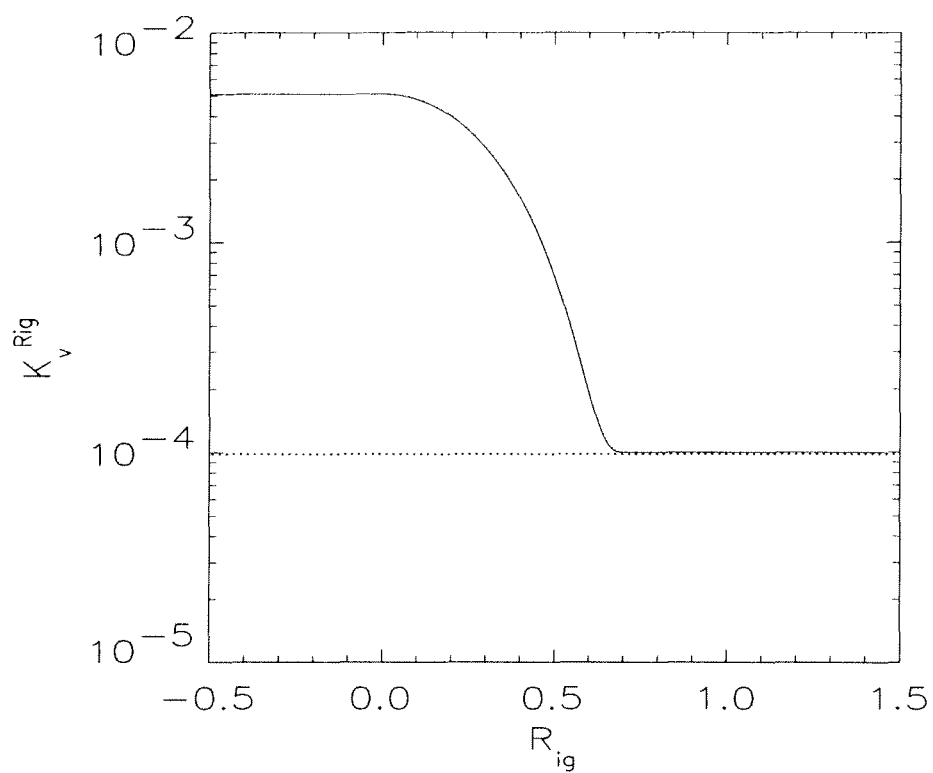
Figure 11. The gradient Richardson mixing coefficient (m^2 s^{-1}) as a function of the Richardson number. The figure is presented for a background diffusivity of 10^{-4} m^2 s^{-1} (dotted line).

(19) are found using the same formulation with different choices for the background diffusivity. The vertical mixing coefficient for momentum as a function of Richardson number is presented in Figure 11 where the default back to background mixing at Richardson numbers greater that 0.7 is indicated with a horizontal dotted line.

3.3.4 Double diffusive mixing

Double diffusive fluxes of heat and salt are calculated with the $\Delta T^{\frac{4}{3}}$ model of Marmorino and Caldwell [1976] (details presented in Section 3.2). Numerically, vertical profiles of the density ratio (R_ρ) are calculated from profiles of temperature and salinity at every time step. In regions of the water column where the density ratio is greater than 1, a double diffusive heat flux (Q_{dd}) is calculated from (14). Mixing coefficients for heat and salt are calculated using (15) and (16) and added to the standard mixing scheme given by (18) and (19).

3.3.5 Data nudging for temperature and salinity

Calculations presented in Klinck [1998] and in Smith et al., [1999] indicate the importance of lateral fluxes of heat and salt (summarized in Figure 2). Given that the model is vertical and time dependent, a source term must be added to (18) and (19) to artificially represent this lateral exchange. Thus, nudging terms are added to the governing equations as a source (or sink) of heat and salt for the sub-pycnocline waters.

The nudging term for temperature in (18) is implemented as

$$F_T^{nudge} = \nu(z) \cdot (T' - T) \tag{22}$$

where the model (T) is driven to some specified climatology (T'). The depth dependent nudging parameter ($\nu(z)$) can have values within the range of 0 (no nudging) to Δt^{-1} (full data replacement). A similar expression is used for salinity nudge in equation (19).

For all simulations presented in this study, $\nu(z) = \Delta t^{-1}$ at depth so that the sub-pycnocline temperature and salinity are replaced with the climatology (Figure 12a) at every time step. The strict nudging implemented in the sub-pycnocline waters is relaxed through the permanent pycnocline to zero in the top 200 m (Figure 12b) where the model is designed to track the complex density structure of AASW as it reacts to forcing at the air-ice-sea interface.

While the model is configured to allow nudging to any specified temperature or salinity, the initial conditions used in this model represent the climatology in the model (Figure 12a). The initial conditions for AASW are obtained by averaging all of the hydrographic profiles from stations occupied during the 1993 winter cruise. Initial conditions for the sub-pycnocline waters are obtained by averaging the profiles from all four cruises. Comparing the results of this calculation to those presented in Hofmann et al. [1996] indicates that the sub-pycnocline averages represent climatology for the west Antarctic Peninsula shelf waters.

Methods other than nudging could have been used to keep the sub-pycnocline waters from drifting. An alternative technique is to hold the temperature and salinity of the bottom grid point constant, which assumes an infinite supply of deep water with the specified hydrographic properties. However, this approach forces heat and salt through the bottom only and fails to reproduce the structure of the sub-pycnocline waters. The method used in this study is designed to mimic horizontal fluxes of heat and salt between the UCDW and the modified UCDW (Qh in Figure 2) and maintains the structure of the sub-pycnocline waters without affecting AASW. It also allows the sub-pycnocline heat and salt fluxes to be calculated so that the lateral exchanges can be estimated.
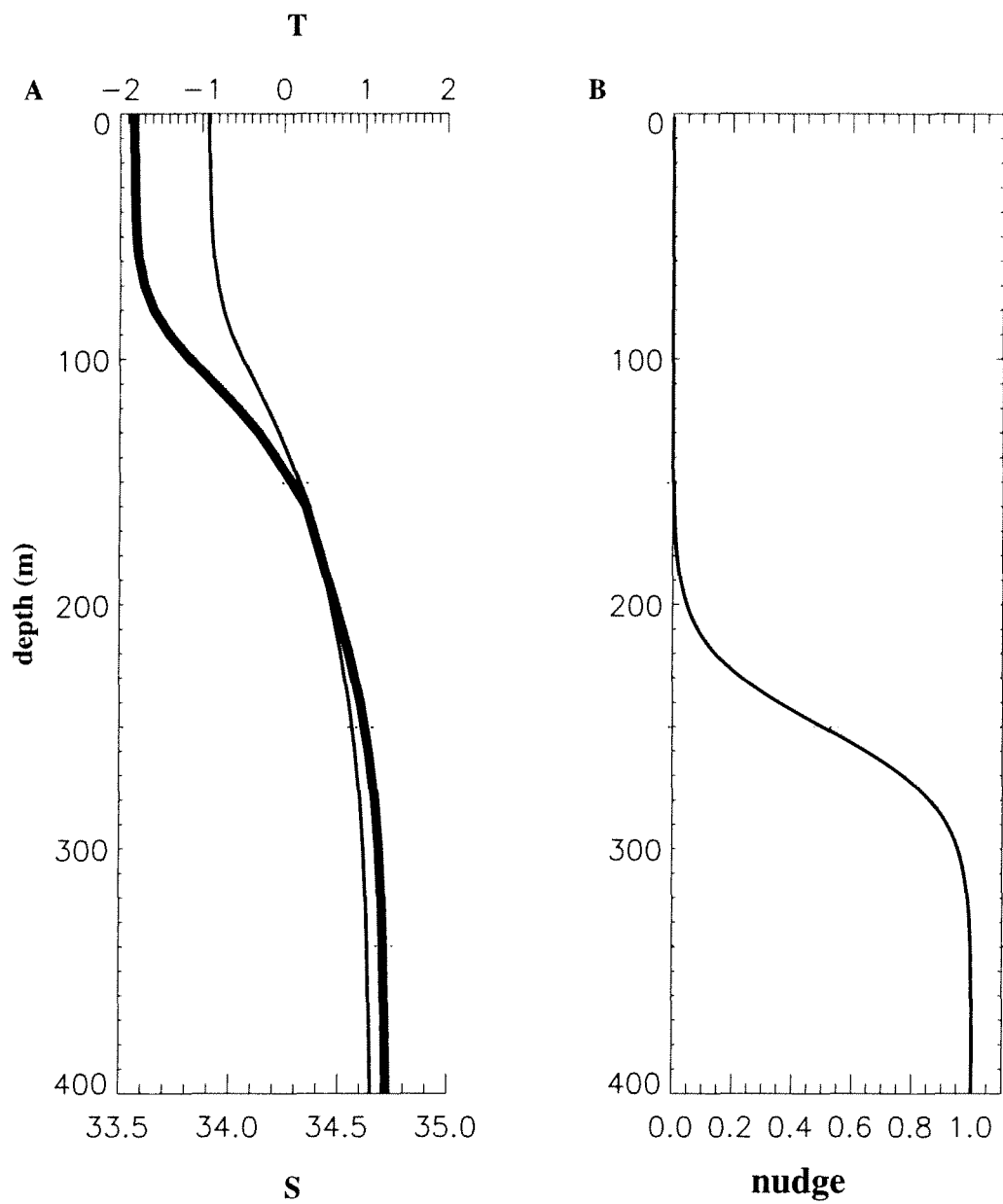
Figure 12. Nudging and climatology for the ice-ocean model. A) Vertical temperature (thick) and salinity (thin) profiles used for initial conditions and nudging. (B) Depth-dependent nudging parameter normalized by Δt. For $\nu(\Delta t)^{-1} = 0$ there is no nudging; for $\nu(\Delta t)^{-1} = 1$ the climatology replaces the simulated values.

3.4 Ice model

The sea ice model used in this study is based on a model presented in Mellor and Kantha [1989], Kantha and Mellor [1989] and Häkkinen and Mellor [1990]. This series of papers and the model itself will be referred to as the MKH papers and model.

The primary difference between the model used here and the MKH model is the treatment of thermodynamics within the sea ice. The MKH model includes one internal ice temperature point (i.e. Semtner 1-level ice model) while the model presented here follows the thermodynamics of the Semtner 0-level ice model [Semtner, 1976], which treats the ice as a uniform layer with thickness (h_i) and neglects internal ice thermodynamics. Effects of a temperature distribution within the ice are considered to be negligible for relatively thin ice (e.g., $h_i \sim 0.5$ to 1 m at maximum winter extent) as observed along the western Antarctic Peninsula.

The model (Figure 13) tracks four prognostic variables: area-averaged ice thickness ($h_i^{av} = A_i h_i$), percent local ice concentration (A_i) and the horizontal components of ice velocity (U_i and V_i). Changes in the ice thickness result from growth/melt rates at the air-ice, air-ocean and ice-ocean interfaces, which are produced by imbalances in the local heat fluxes.

3.4.1 Ice thickness and concentration

The equations for the area-averaged ice thickness and local ice concentration are given by

$$\frac{\partial (A_i h_i)}{\partial t} = \frac{\rho_o}{\rho_i} \left[A_i (Wio - Wai) + (1 - A_i)(Wao + Wfr) \right] \qquad (23)$$

and

$$h_i \frac{\partial A_i}{\partial t} = \frac{\rho_o}{\rho_i} \left[\Phi(1 - A_i)Wao + \Psi A_i Wio + (1 - A_i)Wfr \right] \qquad (24)$$

where the growth rates (m s^{-1}) associated with the air-ice, ice-ocean and air-ocean
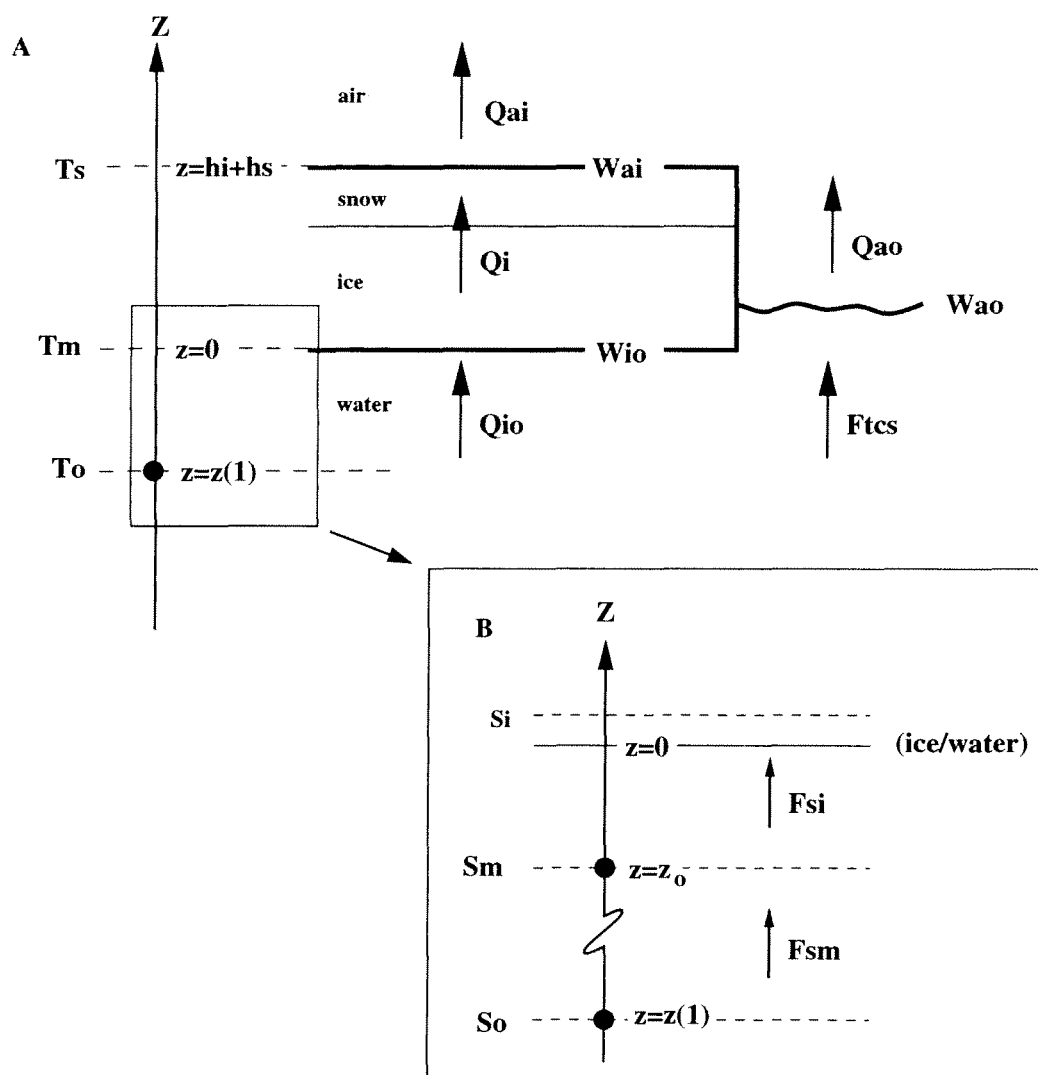
Figure 13. A schematic of the thermodynamics at the air-ice-ocean interface (with an optional, prescribed snow layer). A) Illustrated along the z-axis are the relative locations of the temperature at the ice-snow surface (Ts), base of the ice (i.e. molecular sub-layer) (Tm) and the first internal ocean grid point (To). The fluxes of heat from the ocean to the ice (Qio), the surface of the ice and open ocean to the atmosphere (Qai and Qao, respectively), through the ice ($Qice$) and from the internal ocean to the ocean surface (F_{tcs}) are indicated. Growth rates at the air-ice, (Wai), the ice-ocean (Wio) and open ocean (Wao) are indicated. B) An expanded schematic of the ice-water interface to illustrate salt fluxes from the molecular sub-layer to the ice (Fsi) and from the ocean to the molecular sub-layer (Fsm).

interfaces are indicated as Wai, Wio and Wao, respectively (Figure 13). Changes in ice thicknesses and concentration from horizontal ice motion (e.g., ice convergence and rheology) are neglected in this study. A convergence term can be added to (23) and (24), as in the MKH model; however, MKH specify the convergence term from observations in the Arctic ocean. Such observations do not exist for the west Antarctic Peninsula shelf region so the term is not included. The last term on the right hand side of (23) represents a growth rate associated with the conversion of sea water to frazil ice which occurs when the water column becomes super cooled (details in Mellor and Kantha [1989]). Frazil ice formation is calculated as part of the molecular sub-layer (Section 3.4.5); however, it was not found to play a significant role in ice production in the west Antarctic Peninsula region.

The process represented by (23) is the conservation of volume while (24) is an empirical relationship which merely partitions the thermodynamics from (23) into changes in ice thickness and concentration with the latter process interpreted as the opening and closing of leads. The parameters Φ and Ψ in (24) are tuning parameters and the values given in Häkkinen and Mellor [1990] are used,

$$\Phi = \begin{cases} 4.0 & \text{when} \quad Wao > 0 \text{ (growth)} \\ 0.0 & \text{when} \quad Wao < 0 \text{ (melt)} \end{cases}$$

$$\Psi = \begin{cases} 0.7 & \text{when} \quad Wio < 0 \text{ (melt)} \\ 0.0 & \text{when} \quad Wio > 0 \text{ (growth)} \end{cases} \tag{25}$$

where Φ and Ψ partition sea ice growth rates at the open ocean and under the ice.

The physical interpretation of the tuning parameters are as follows: for $A_i < 1\%$ and $\Phi{=}1$, Wao builds ice along the edges of leads thus preserving the thickness. Choosing the parameter to be greater than 1 is non-physical, but allows Wao to affect ice thickness as well as the concentration (MKH demonstrated the model is not sensitive to changes in this parameter once $\Phi > 2$). The Ψ term represents a reduction in ice concentration resulting from the differential removal of ice near leads [Häkkinen and Mellor, 1990].

3.4.2 Model heat fluxes

The total simulated heat flux is determined by combining ice-free, open ocean heat flux (Q_{ao}) calculated similarly as the ice-free, open ocean heat flux in Section 3.2 with through ice heat fluxes (Q_{ice}) calculated at every time step within the model. Meteorological variables of air temperature, relative humidity, cloud cover and atmospheric pressure obtained from the Faraday data set (Section 3.1.2) are used to calculate the surface fluxes of heat. The simulations also require sea surface temperature which is obtained from the top model grid cell. The oceanic heat flux (F_{tcs} in Figure 13b) is determined from the MY2.5 turbulence closure scheme using the top two oceanic grid points as:

$$F_{tcs} = \left(K_h + K_h^{Ri_g} \right) \frac{\partial T}{\partial z} \quad as \; z \to 0 \tag{26}$$

The double diffusive contribution near the sea surface is assumed to be negligible and is not included in (26).

The heat flux through the ice ($Qice$) is given by

$$Qice = \frac{k_s (T_s - T_m)}{h_s + \left(\frac{h_i \cdot k_s}{k_i} \right)} \tag{27}$$

where h_i and h_s are the thicknesses (m) of the ice and optional snow layers, respectively. The thermal conductivity of ice and snow are represented by k_i and k_s and T_m is the temperature at base of the ice in the molecular sublayer. Parameterizing the thermodynamic effects of the molecular sublayer [Mellor and Kantha, 1989; Steel et al., 1989] provides the thermodynamics coupling (Qio) between the ice and the ocean model (Section 3.4.5).

The air-ice heat flux (Qai) is calculated in a manner similar to the open ocean (Section 3.2), with sea surface temperatures (T_{sst}) and heat transfer coefficients (C_{HO}) in (11) and (12) replaced by the surface temperature of the ice (T_{ice}) and heat transfer coefficients appropriate for the air-ice interface. Choices for the transfer

coefficient for ice (C_{HI}) and for surface albedos (Table 2) are consistent with choices in the MKH model and those in Ikeda [1989].

3.4.3 Ice growth rates

The surface temperature of the ice, T_s, is advanced from the current time level ($t = n$) to the next time level ($t = n + 1$) by

$$T_s^{n+1} = min \ (T_s^n + \Delta T_s, \ T_{melt}) \tag{28}$$

where T_s is always less than or equal to the melting point of ice (T_{melt}) which is a function of the salinity within the ice (S_i) defined in Fujino [1974] as

$$T_{melt} = -m \cdot S_i - n \cdot z \tag{29}$$

where m and n are defined to be 5.43×10^{-2} K psu^{-1} and 7.59×10^{-4} K m^{-1}, respectively. Ice salinity is held constant throughout the simulations and is prescribed to be 8. Similar studies use various values for the salinity of sea ice with thick Arctic ice having values order of 4 to 5 [Häkkinen and Mellor, 1990; Parkinson and Washington, 1979] while thinner ice of Marginal Ice Zones (MIZ) have been characterized with salinities as high as 8 to 10 [Kamph and Backhaus, 1998].

The temperature change at the ice surface (ΔT_s) is obtained by assuming a balance of the heat flux at the air-ice interface balances (i.e. $Qai=Qice$). Using (28), the change must satisfy

$$\frac{k_s(T^n + \Delta T_s - T_m)}{h_s + \left(\frac{h_i \cdot k_s}{k_i}\right)} = Q_{solar}^{ice} + \epsilon\sigma \cdot (T^n + \Delta T_s + 273)^4 +$$
$$\rho_a C_{pa} C_{HI} W \left(T^n + \Delta T_s - T_{air}\right) \tag{30}$$

where Q_{solar}^{ice} is the combined affects of Q_{sw}, Q_{lw}^{down} and Q_{lat} over the ice. Solving (30) for (ΔT_s) yields an implicit equation for the temperature change (recall that

Q_{ice}^{solar} depends on T_s) which can be iterated to obtain the ice temperature change, and the new T_s. This calculation usually converges within 2 to 3 iterations.

Once the new T_s is found, heat fluxes are calculated. Any imbalance between through ice heat fluxes and those at the atmosphere-ice interface from setting surface temperatures to the freezing point results in surface melting. The fresh water flux from this surface melting is immediately added to the water column through the leads (i.e. no melt ponds are allowed to form). The surface melting is calculated as

$$Wai = \frac{(Qai - Qice)}{\rho_o L_f} \tag{31}$$

where L_f is the latent heat of fusion (Table 2). Note that iterating on ΔT such that $Qice = Qai$ forces the growth rate at the atmosphere-ice interface to be zero under non-melting conditions as the numerator in (31) vanishes. This makes physical sense because there is no water at the atmosphere-ice interface to form ice.

Similarly, growth rates at the base of the ice and at the atmosphere-ocean interface are calculated from imbalances in respective heat fluxes as (details in Section 3.4.5),

$$Wio = \frac{(Qice - Qio)}{\rho_o L_f} \tag{32}$$

$$Wao = \frac{(Qao - F_{tcs})}{\rho_o L_f} \tag{33}$$

The growth rate at the base of the ice can be positive (ice growth) or negative (ice melt) depending on the relative magnitudes of the fluxes. Growth rates at the atmosphere-ocean interface are constrained to be positive (growth) or zero by the choices of Φ (25) which eliminates the possibility of melting at the sides of the leads. The thermodynamic effects of leads are included by allowing heat to warm the surface and which increases melting at ice-ocean interface.
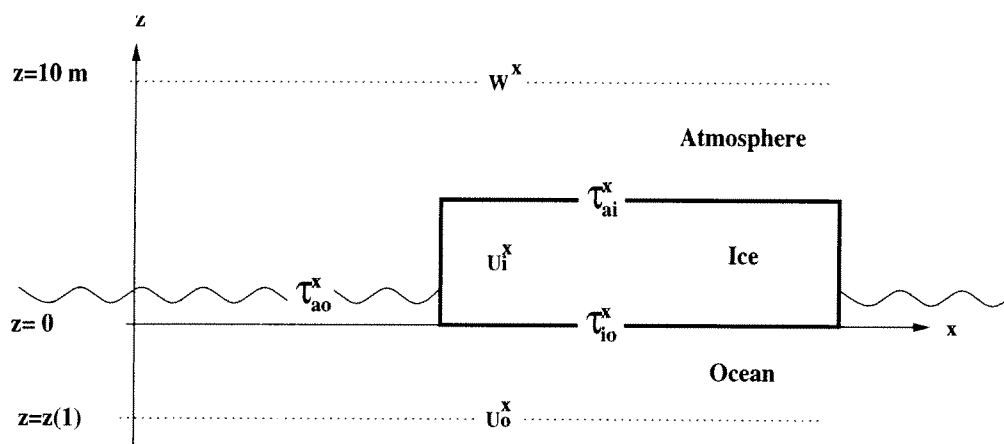
Figure 14. Schematic for the ice-ocean model interfacial stress terms ($\hat{x}$ direction). Illustrated along the z-axis are the relative locations of wind speed, (W^x), ice-snow velocity (U_i) and ocean velocity (U_o^x). Also indicated are the interfacial drag at the air-ice (τ_{ai}^x), ice-ocean (τ_{io}^x) and air-ocean (τ_{ao}^x) interfaces.

3.4.4 Ice momentum equations

The primary role of ice velocity in this model is to provide mixing to the ocean model under ice covered conditions. The ice slab is modeled as a free drifting block (e.g., no internal effects from rheology) forced by wind stress at the air-ice interface (τ_{ai}) and interfacial ice-water drag (τ_{io}). The free drift equations [Ikeda, 1989] are

$$A_i h_i \frac{\partial (U_i, V_i)}{\partial t} = A_i h_i f \; (V_i, -U_i) + \frac{A_i}{\rho_i} \cdot \left(\tau_{ai}^{(x,y)} - \tau_{iw}^{(x,y)} \right) \tag{34}$$

where ρ_i is the density of ice (Table 2) and the superscript x and y on τ_{ai} and τ_{iw} denote the component associated with U_i and V_i, respectively.

Simple drag laws are used to calculate the drag at the air-ocean and the open ocean, air-water (τ_{ao}) interfaces (Figure 14).

3.4.5 Ice-ocean model coupling and surface boundary conditions

The surface boundary condition used for the ocean model is [Mellor and Kantha, 1989],

$$\rho_o K_m \frac{\partial (u, v)}{\partial z} = A_i \tau_{io}^{(x,y)} + (1 - A_i) \, \tau_{ao}^{(x,y)} \tag{35}$$

where K_m is the mixing coefficient for momentum from the MY2.5 scheme (Section 3.3.2). The ice-ocean stress ($\tau_{io}^{(x,y)}$) is given by

$$\tau_{io}^{(x,y)} = \frac{\kappa \mu}{ln(\frac{z}{z_o})} \Delta(u, v) \tag{36}$$

where $\kappa = 0.4$ is the von-Karman constant and $\mu = [(\tau_{io}^x)^2 + (\tau_{io}^y)^2]^{\frac{1}{4}} \cdot \rho_o^{-\frac{1}{2}}$ is the friction velocity. The roughness parameter (z_o) is calculated as in the MKH studies and $\Delta(u, v)$ is the velocity difference between the ice and the ocean defined at the top oceanic grid point. The interfacial stress calculated in this step forces both the ocean and ice models, thus providing momentum coupling between the two. Typical stress values as a function of wind speed for the 1993 simulation (Section

4.3.2) are indicated in Figure 15 and are consistent with those reported in Wamser and Martinson [1993] for the Weddell Sea.

The thermodynamic coupling between the ice and ocean models (as in the MKH model) is based on the parameterization of a molecular sub-layer [Steel et al., 1989], which is a thin layer at the base of the ice. The molecular sub-layer is assumed to be at the freezing temperature ($T_m = T_f(S_m)$) (Figure 13b). The numerical details for parameterizing the molecular sub-layer are presented in Mellor and Kantha [1989] but are summarized here.

The key equations for the thermodynamic coupling involve heat and salt fluxes between the ocean and the molecular sub-layer. These equations are

$$F_{T_{o \to m}} = -\rho_o C_{po} C_{T_z} (T_m - T_o) \tag{37}$$

$$F_{S_{o \to m}} = -C_{S_z} (S_m - S_o) \tag{38}$$

where S_o is the oceanic salinity, C_{T_z} and C_{S_z} are heat and salt exchange coefficients, respectively, and depend on molecular diffusivities as described in MKH and in Steel et al. [1989].

The salt flux between the molecular sub-layer and the ice is given by

$$F_{S_{m \to i}} = (S_i - S_o) \cdot [\, A_i \cdot (Wio - Wai) + (1 - A_i) \cdot Wao \,] + S_o (P - E) \tag{39}$$

where $(P - E)$ is net precipitation over evaporation and the growth rates (Wai, Wio and Wao) are obtained from the current time level. Evaporation (E) is assumed to be zero while precipitation (P) prescribed from the atmospheric data (Section 3.1.2).

The daily averaged precipitation records from Palmer station are converted into an annual average of 2.07×10^{-8} m s^{-1} and added to the model at every time step. This annual average agrees well with Cullather et al. [1998] who obtain net precipitation on the order of 500 - 700 mm yr^{-1} (1.5 - 2.2$\times 10^{-8}$ m s^{-1}) for the west
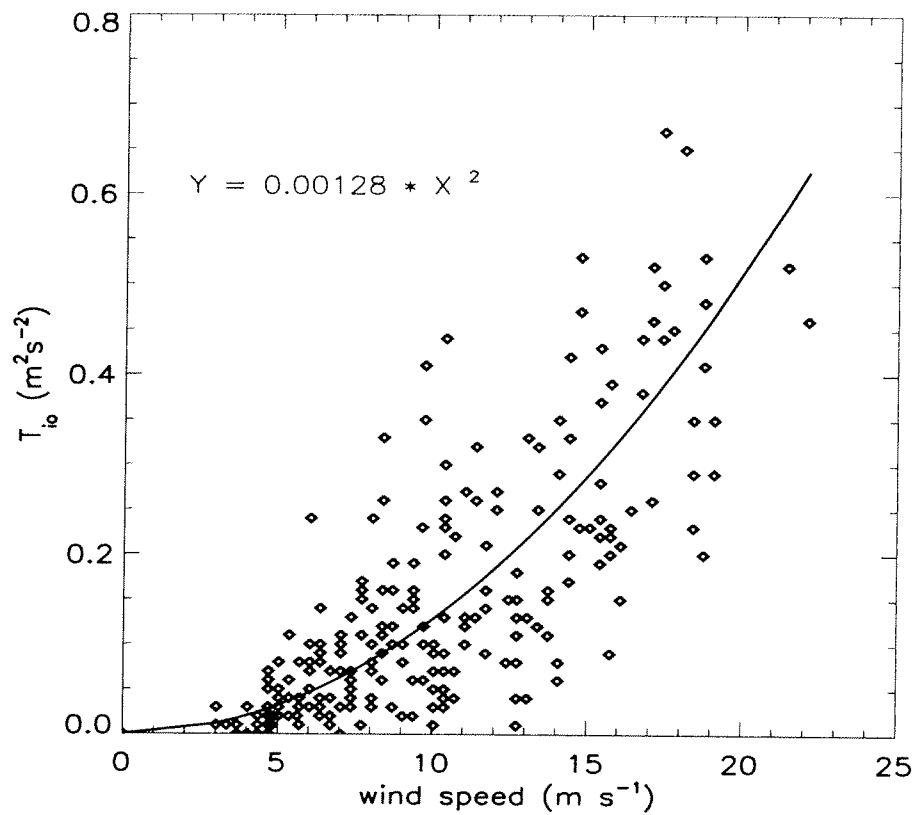
Figure 15. Ice-ocean stress as a function of wind speed. A least squares quadratic curve of best fit to the data is indicated with the solid curve.

Antarctic Peninsula region. The model accumulates snow if the surface temperature of the ice is colder than the freezing point, otherwise, the precipitation enters the ocean as water through open leads.

Salinity at the ice-ocean interface is found by equating (38) and (39). The melting point (T_m) is then obtained from local salinity (S_m) using (29) which is substituted into (37) and equated to the heat flux at the ice-ocean interface. Coupling between the models is achieved by forcing both models with these fluxes.

3.5 Numerical details

The ocean model is integrated in time using an implicit scheme described in Mellor [1993] and Blumberg and Mellor [1987]. The implicit scheme is designed for the full three-dimensional model and removes time stepping constraints from small values of vertical grid spacing and possible large values of vertical viscosities.

An Euler scheme is used to solve (23) and (24). The ice momentum equations (34) are a stiff set of equations with the potential for small oscillations in the forcing to be amplified by the inverse of ice thickness (i.e. h_i^{-1}). Because of this singularity, h_i is never allowed to go to zero. Instead it is held at a very small number $(h_{i_{min}} = 10^{-3}$ m) and A_i is allowed to vanish under conditions of no ice cover. For model stability, (34) is solved implicitly.

The time step (Δt) for all model simulations is 900 s (15 minutes) which is smaller than necessary for the simulations presented, but was chosen in anticipation of extending the model to three dimensions in the future. The model depth is 400 m and is resolved with 150 levels giving a vertical grid spacing (Δz) of 2.6 m. This vertical grid spacing was found to be smaller than needed, but resolved features in AASW such as vertical stratification. Further decreasing Δz did not improve the simulations but increased run time. Decreasing the vertical resolution decreased the ability to simulate features in the upper portion of AASW while producing no

significant change in the pycnocline or sub-pycnocline portion of the model. This latter result is most likely produced by the relaxation scheme and would need to be re-examined if nudging to climatology was removed or modified.

CHAPTER 4

RESULTS

The first portion of this chapter presents results from a AASW heat budget constructed using atmospheric and oceanic data measured in 1993. The second portion presents results of the oceanic response and the dynamics of the mixed layer under the atmospheric forcing obtained with the time and vertically dependent, coupled sea ice-ocean model.

4.1 AASW heat budget for 1993

4.1.1 Atmospheric regime

The winds along the west Antarctic Peninsula are typically strong, exceeding 15 to 20 m s^{-1} (30 to 40 knots) and are predominantly onshore to the southwest, or towards the north or northeast (Figure 16a). Air temperatures recorded at Faraday Station for 1993 had summer maximum temperatures around 5°C and winter lows around -15°C (Figure 16b). These winter temperatures fall in the mid-range of winter lows when compared to other years (Figures 9a).

Atmospheric conditions along the shelf to the west of the Antarctic Peninsula are warm compared to conditions in the interior of Antarctica. They are warmer than temperatures recorded along other Antarctic coastal regions characterized by permanent ice cover (e.g., Weddell Sea) [Smith et al., 1996] and are an indication that the shelf west of the Antarctic Peninsula can be characterized by a maritime climate. Daily averaged relative humidities along the peninsula are in excess of 80% while cloud cover is typically 80 to 90% (Figures 16b,c); a further indication of the maritime climate which characterizes the west Antarctic Peninsula shelf region.

All 1993 atmospheric parameters recorded at Faraday show variability about weekly intervals within which are embedded shorter (2-to-4 day) fluctuations. These

events occur approximately weekly and is associated with the passage of storms and their associated warm/cold fronts. Storm-scale variability occurs throughout the year (Figure 16), but the largest reversals are in the mid-winter temperature record which can increase from winter lows (-15°C) to summer-like temperatures (0°C) in one day and remain there for 5-10 days.

The wind record at Faraday can be used to partition the atmospheric regime into two general categories: strong, warm winds blowing down the coast, and weaker, cold winds blowing onshore from the west or south (Figures 16a,b and 17). The mid-winter temperature reversals are related to reversals in the wind field with warmer atmospheric conditions prevailing when winds are from the north. The relationship between the winds and the air temperatures persists for the entire year, but is most pronounced during the winter and spring seasons (Figure 17).

Cumulative wind rosettes for the 1993 Faraday Station (Figures 17) represents conditions over the entire year. Winds along the west Antarctic Peninsula are predominantly from the northeast or southwest (Figure 17a). Winds from the northeast are associated with air temperatures which are 5°C warmer than times with winds from the south (Figure 17c). Seasonal relationships between wind direction, speed and air temperatures can be seen in Figure 17d-o.

Sea surface temperatures (SST) (Figure 16e) (Section 3.1.3) range from summer highs of 1.6°C to freezing conditions in the winter (T_f = -1.8 to -2.0°C for salinities $\sim$ 33.8 to 34.0).

The ice free period near Palmer Station (day 0 through 170) is followed by 5 to 6 months of ice cover (Figure 16f). At the time of maximum winter ice extent, the region is characterized by 80% ice cover. Ice develops around day 170 with a rapid advance lasting several weeks. The initial growth period is followed by alternate ice growth and retreat which persists from day 190 to the time of maximum winter ice extent around day 305-310. A rapid spring melt begins around day 290 and
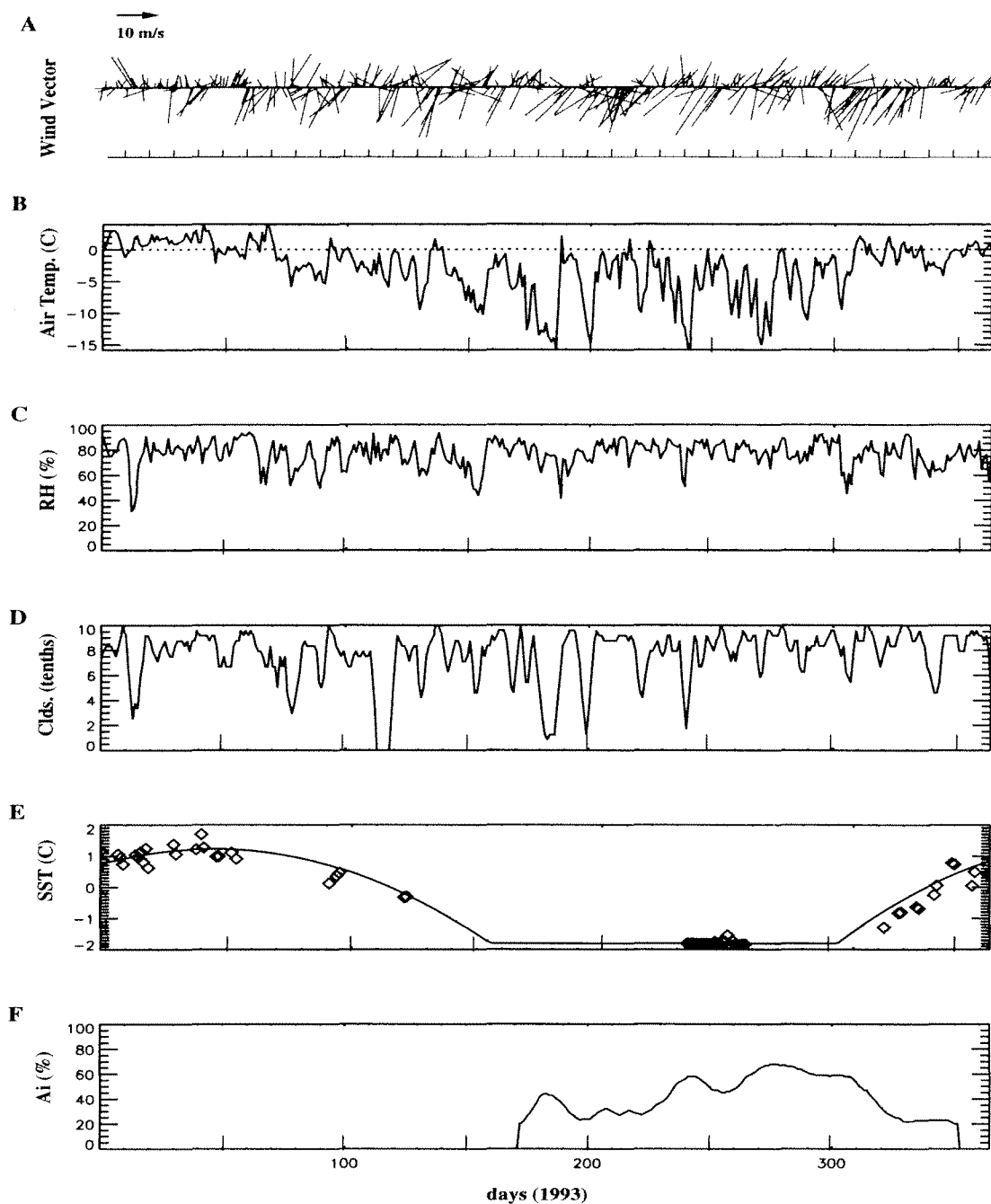
Figure 16. Atmospheric and oceanic variables for the 1993 ice free heat budget. Daily-averaged time series of A) Wind vectors (+ x-axis aligns with East), B) air temperature, C) relative humidity, D) cloud cover, E) near-Palmer SST (details in Section 3.1.3) and F) near-Palmer, ice concentrations. Observations are smoothed with a 7 day filter for presentation.
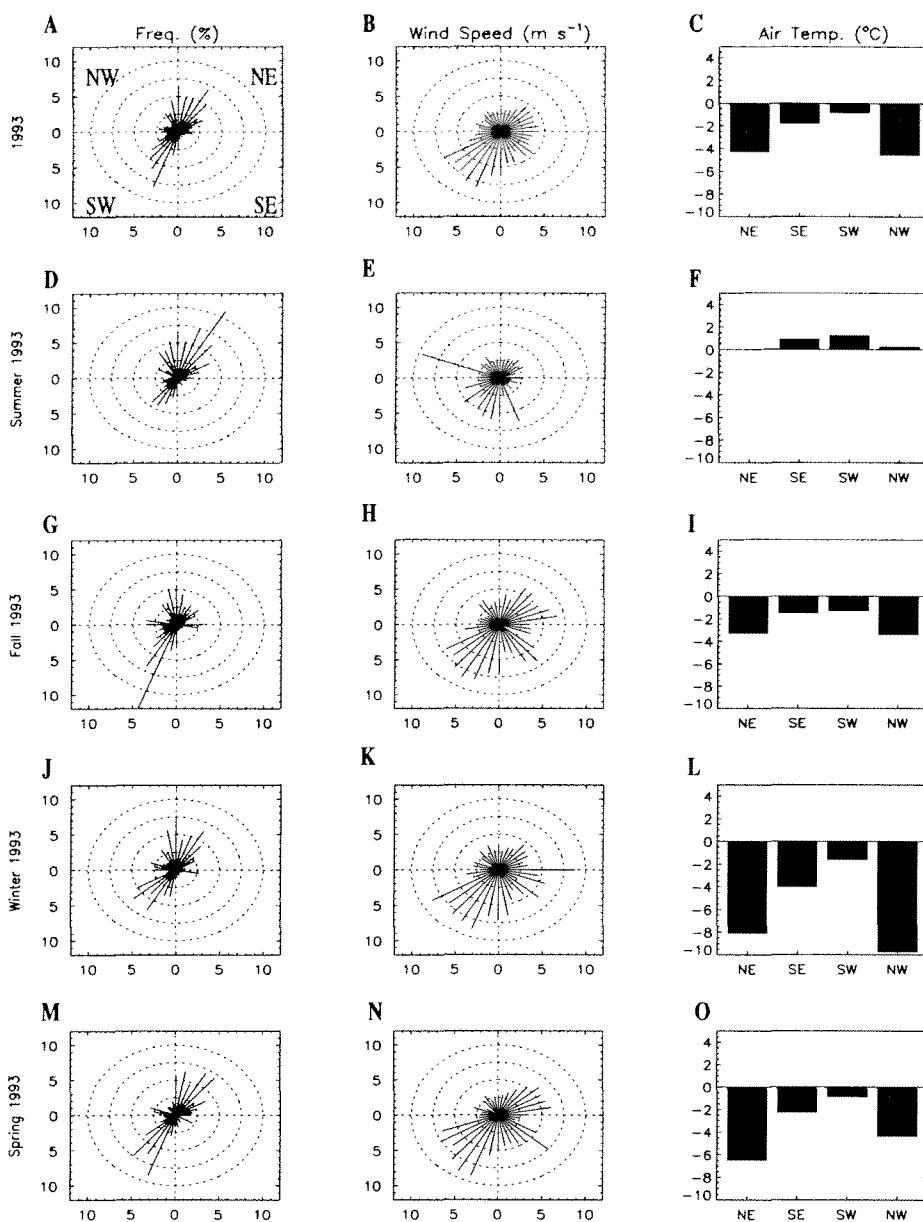
Figure 17. Cumulative 1993 wind rosettes for Faraday Station. A) The percentage of wind observations recorded at Faraday Station in a given 10° bin (NW, NE, SE and SW quadrants are labeled for reference). B) Average speed of all wind observations (m s^{-1}) blowing towards a given 10° bin. C) Average air temperature (°C) for winds blowing towards a given quadrant (i.e. winds blowing towards NE had an average wind speed below 5 m s^{-1} and corresponded to average temperatures of -5°C). Panels D to O provide the seasonal breakdown of A to C.

Table 3. Ice free heat flux statistics (W m^{-2}) for times consistent with three cruises to the west Antarctic Peninsula during the 1993 sampling season. All heat fluxes are rounded to the nearest 5 with positive fluxes indicating AASW warming (i.e. positive down).

LTER Cruise ID	Q_{open}	Q_{sw}	Q_{lw}	Q_{sens}	Q_{lat}
93A	110 ± 50	160 ± 70	-30 ± 15	5 ± 5	0 ± 5
93B	-90 ± 45	25 ± 15	-50 ± 20	-40 ± 30	-10 ± 5
93C	-30 ± 15	20 ± 5	-20 ± 10	-30 ± 25	-5 ± 5

continues through the spring until the ice vanishes. The initial spring melt is rapid but stalls around day 325 for several weeks.

4.1.2 Ice free, surface heat budget for surface waters

The atmospheric conditions presented in the previous section are used with the bulk aerodynamic equations presented in Section 3.2 to calculate a surface heat budget (Q_{open}) for the ice free shelf waters along the west Antarctic Peninsula (Figure 18). A summary of total budget and its individual terms over the times of the three 1993 cruises is presented in Table 3.

The short wave flux (Qsw) ranges from a summer maximum of 200 to 250 W m^{-2} to winter lows near 0 W m^{-2} (Figure 18a). From day 0 to 100, and again from day 300 to 365 (i.e. fall and summer months), short wave radiation is the dominant term in the surface heat budget providing nearly all of the heating (Figure 18a,c). Net long wave radiation (Q_{lw}^{down}-Q_{lw}^{back}) is a persistent oceanic loss with an annual average of 30 W m^{-2} and times when the losses are 80 W m^{-2}. This term becomes important in the overall heat budget during the fall when the dominance of short wave radiation diminishes sufficiently that long wave radiation cancels its heating effects. Short and long wave radiation balance around day 70 when SST begins to fall (Figure 16e).

From late-spring to early-fall, the ocean-atmospheric temperature difference is
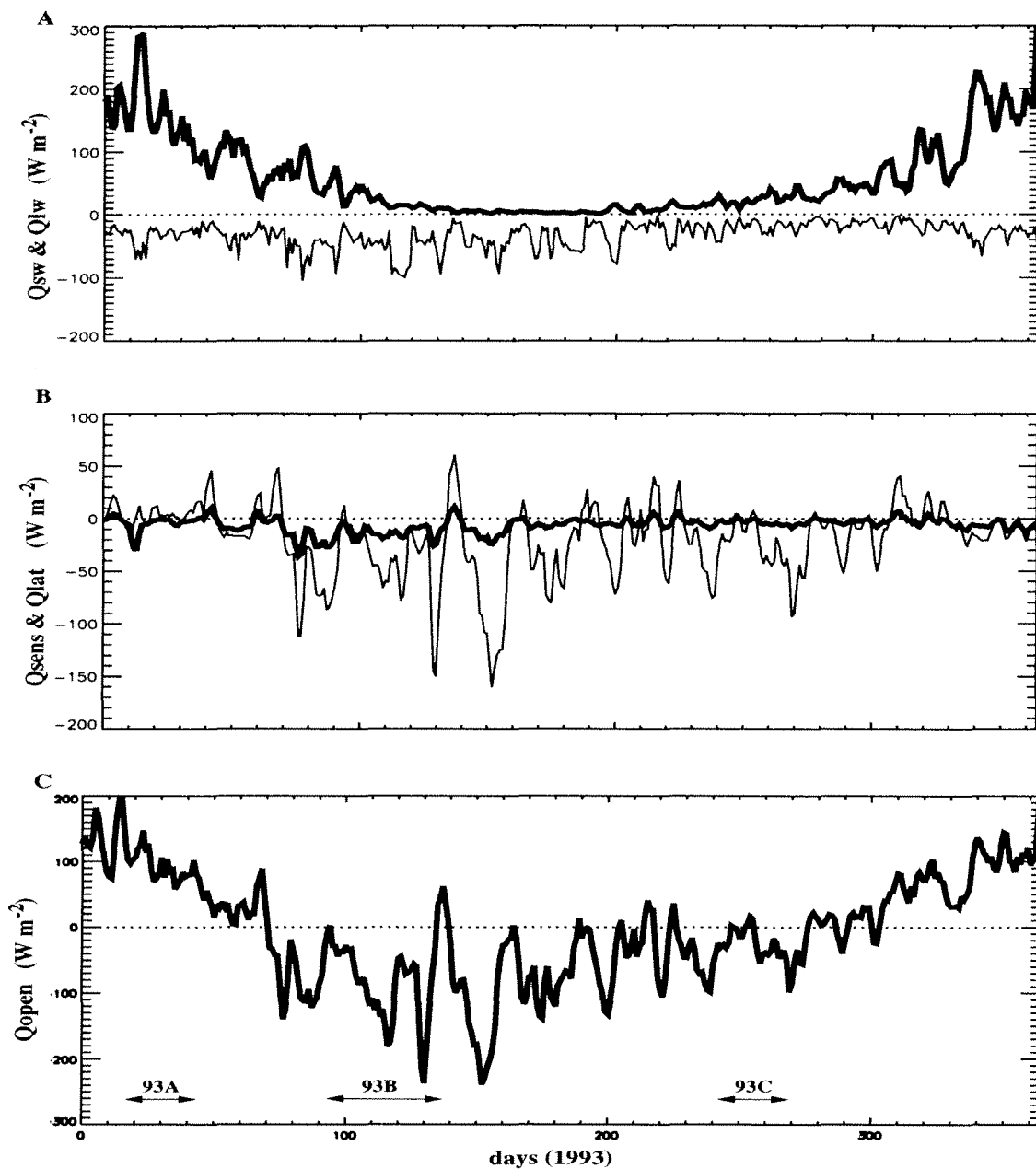
Figure 18. Ice free, surface heat budget calculated for 1993. Positive heat fluxes indicating AASW surface warming. All values are multiplied by (1 - A_i) (see Equation 8) and smoothed with a 3-day filter for presentation. A) (1 -α_s)· Q_{sw} (thick line) and ϵ · (Q_{lw}^{back} - Q_{lw}^{down}) (thin line). B) Q_{lat} (thick line) and Q_{sens} (thin line). C) Total Q_{open} from Equation 8. The x-axis is in days since January 1, 1993. The beginning and ending dates of the cruises to the region during the summer (93A), fall (93B) and winter (93C) are indicated by arrows and zero heat flux is indicated with a horizontal dotted line for reference.

only a few degrees resulting in sensible heat exchanges which averages near zero and ranges between $\pm$ 5 to 10 W m^{-2} (Figure 18b). Large temperature differences between the ocean and the atmosphere during the late fall, and winter, cause large sensible heat losses which can exceed 100 to 150 W m^{-2} (Figure 18b). The contribution of latent heat loss (Q_{lat}) to the ice free heat budget is usually insignificant compared to sensible contributions, being typically 4 to 10 times smaller (Figure 18b and Table 3). The low values for latent heat exchanges are typical for maritime environments and result from high relative humidity (Figure 16c) which suppresses evaporation. Daily averaged humidity at Faraday is 80 to 90% while relative humidities between 95 and 100% were recorded during the March to May 1993 (93B) cruise [Smith et al., 1993a].

The summer heat budget is dominated by surface heating from short wave radiation while the winter budget has large sensible heat losses through ice-free leads. Sensible heat losses through leads are episodic and reflect fluctuations in the atmospheric temperature (Figure 16b). The largest sensible heat losses (i.e. 100 to 150 W m^{-2}) typically occur when light to moderate winds (i.e. 2 to 5 m s^{-1}) are out from the south with cold atmospheric conditions (Figure 17). These significant sensible heat losses during the winter combine with the persistent heat loss from long wave radiation to force overall ice-free heat budget (Q_{open}) to cool the surface with losses on the order of 150 to 200 W m^{-2}.

Occasional mid-winter, warm atmospheric conditions (e.g., days 135 and 210-220 in Figure 18c) can change sensible heat exchanges from winter maximum heat losses to near zero values. On occasion, sensible heat exchanges are positive causing surface AASW warming during the winter.

The approach used to obtain daily values of SST (Section 3.1.3) introduces uncertainty into the ice free heat budget (Q_{open}). To evaluate the sensitivity of the calculation to SST, the heat budget was recalculated with SST=0°C (Q'_{open}). Other

A

B
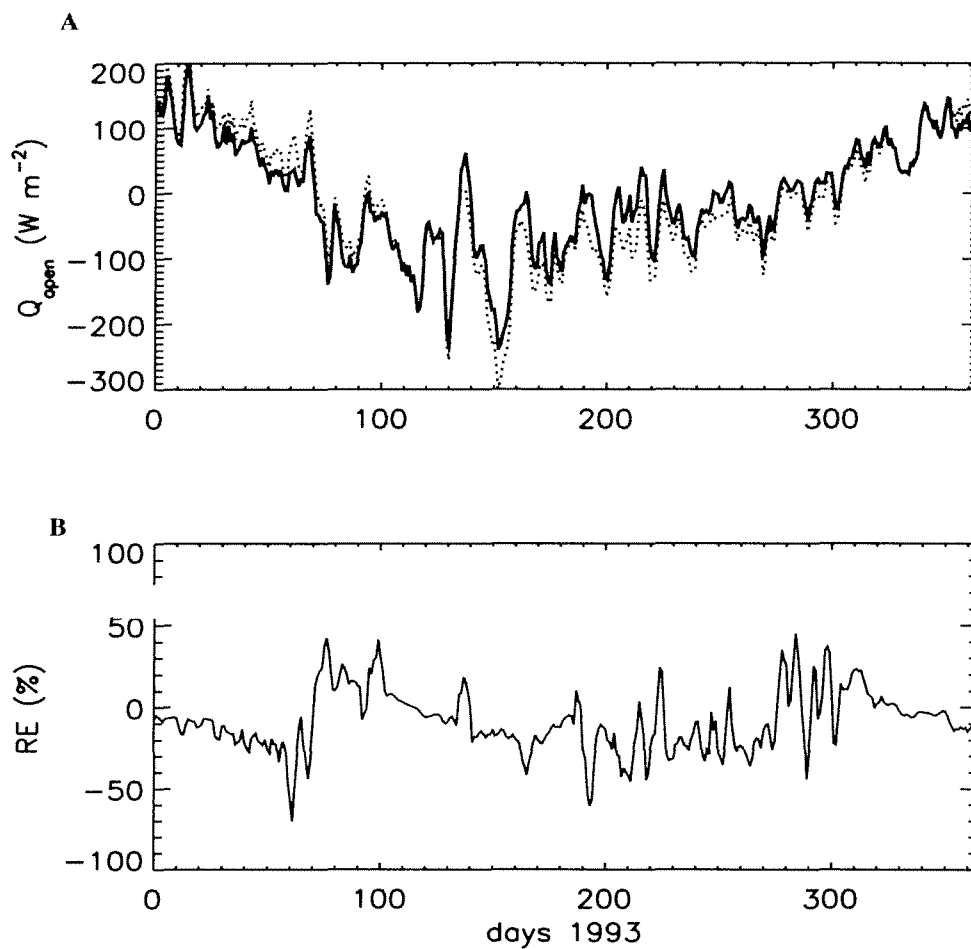
Figure 19. Sensitivity of the open ocean heat budget to SST. A) Heat budget for ice free conditions calculated using derived SST time series (Q_{open}) (thick line) and calculated with SST=0 (Q'_{open}) (thin line). B) Relative error (RE) between Q_{open} and Q'_{open} with RE = (Q_{open} - Q'_{open}) / ($smooth\ Q_{open}$) where *smooth* indicates the use of a 3 day smoother. The average RE is approximately -5%.

choices for SST between -2 and 2 °C yield quantitatively similar results when recalculating the budget (analysis not shown). The average relative error (RE) between the ice-free budget and the ice-free budget with SST=0 (Figure 19b), is approximately -12% with the largest errors resulting during the fall and winter when sensible heating is important in the ice-free heat budget. This average is artificially inflated by a few days when the calculated ice-free budget is near zero and small variations between the two calculations result in fairly large percentages.

During late-spring through early-fall, short wave radiation dominates the budget and errors due to the choice of SST are minimal because SST primarily enters the calculation through sensible heat fluxes in the fall through winter months. As the dominance of short wave heating diminishes in the fall, the temperature difference between the atmosphere and the ocean increases, ($\Delta_{air-SST} \simeq 15°C$) and the contribution of SST to the overall heat budget through sensible heating increases. This winter temperature difference between the atmosphere and ocean is largely determined by changes in the atmospheric temperature as SST remains close to the freezing point. Thus variations in the winter sensible heat exchanges are coincident with variations in the atmospheric conditions.

4.1.3   Heat and salt flux through the permanent pycnocline

As discussed in Section 3.2.2, the presence of warm, salty water of oceanic origin on the shelf provides a reservoir of heat and salt that can be transfered across the permanent pycnocline into the AASW layer.

A necessary condition for the double diffusive instability is Turner Angle (Tu) $< 45°$ [Kelly, 1984]. A sample vertical distribution of temperature and salinity for the 600.140 station (Figure 20a) illustrates the double diffusive calculation using the MC76 model (Figures 20b-c). The permanent pycnocline for 600.140 is characterized by Tu on the order of -65 to -50° (Figure 20b), which results in a maximum double
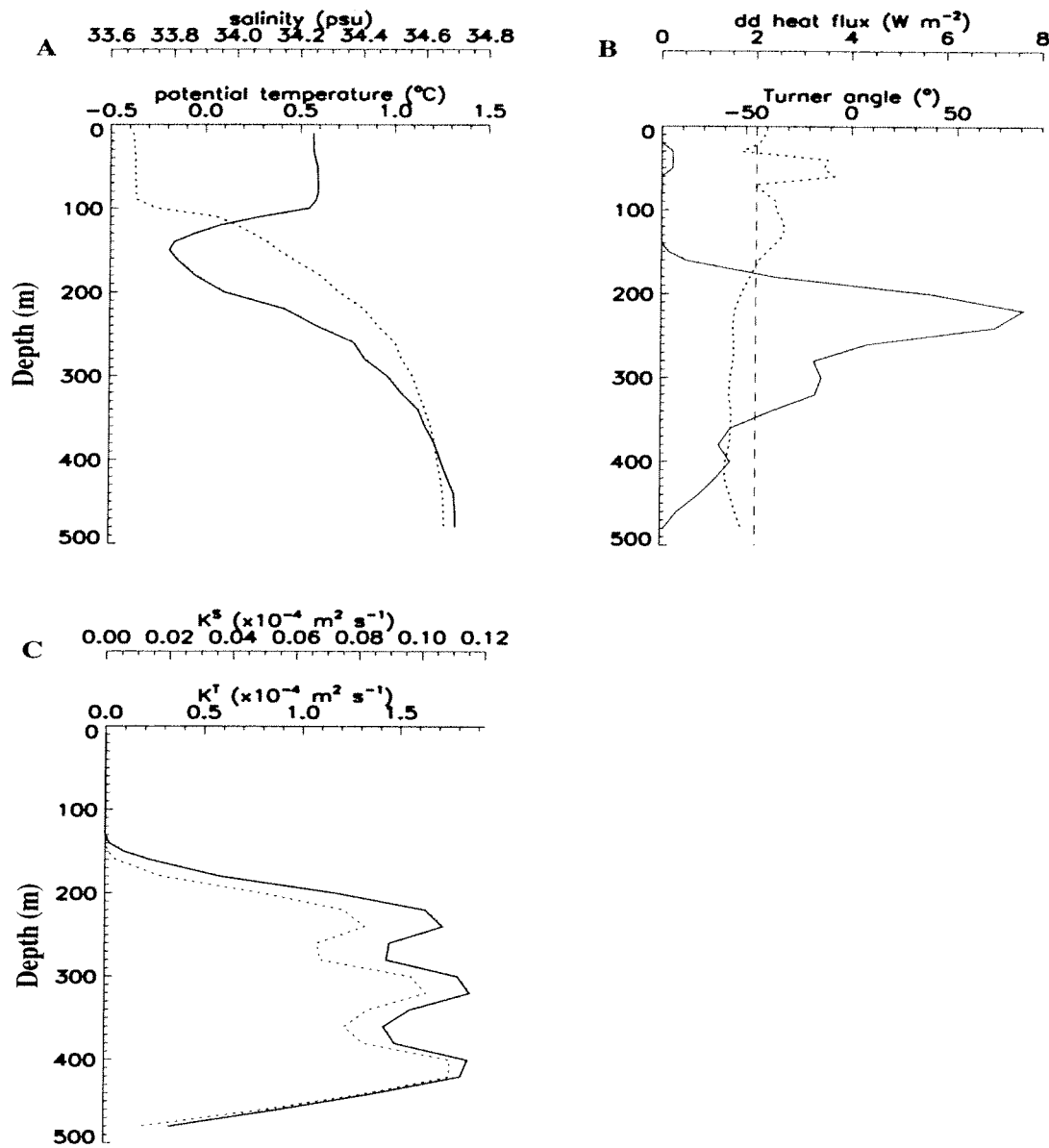
Figure 20. Double diffusive heat flux calculation for station 600.140 (Fall 1993). Vertical distributions of A) temperature and salinity at station 600.140 observed in March-May 1993, B) calculated Turner angle (dotted line) and the double diffusive heat flux (solid line) and C) mixing coefficients associated with the double diffusive heat and salt fluxes.

diffusive heat flux of 8 W m^{-2} at a mid-pycnocline depth of 210 m, the depth of the maximum of temperature and salinity gradients (Figure 20a,b).

Double diffusive mixing coefficients associated with the maximum double diffusive heat flux are found using (15) and (16) as $K_{dd}^T = 1.5 \times 10^{-4}$ and $K_{dd}^S = 1.2 \times 10^{-5}$ m^2 s^{-1}, respectively (Figure 20c). The order of magnitude difference between K_{dd}^T and K_{dd}^S is typical of double diffusive regimes with $R_\rho > 2$ ($Tu < $ -50°C) (Figure 10). The box model calculations presented in Smith et al. [1999] and Klinck [1998] required different vertical mixing coefficients to balance onshore fluxes of heat and salt in order to maintain the observed hydrographic structure of the sub-pycnocline waters.

The across-shelf distribution of double diffusive heat flux, calculated using the MC76 model and temperature and salinity data collected during the 1993 fall cruise across the 600 line, is fairly uniform with maximum values around 10 W m^{-2} (Figure 21). The fluxes are found at depths associated with the permanent pycnocline and tens of meters below WW (sub-surface temperature minimum in Figure 20). The only significant structure in the across-shelf distribution occurs at the shelf break boundary between modified-UCDW and UCDW, where fluxes in the ACC exceed 30 W m^{-2}.

Winter double diffusive heat fluxes, calculated as above, tend to extend deeper into the water column than they do in the fall by 10 to 20 m; however, the maximum heat flux remains at about 10 W m^{-2} (Figures 21a and b). Similar calculations, for transects sampled during the other cruises, indicate that spatial and temporal variability in the double diffusive heat flux is small and subtle differences which occur are within the accuracy of (14) and the data used (analysis not shown).
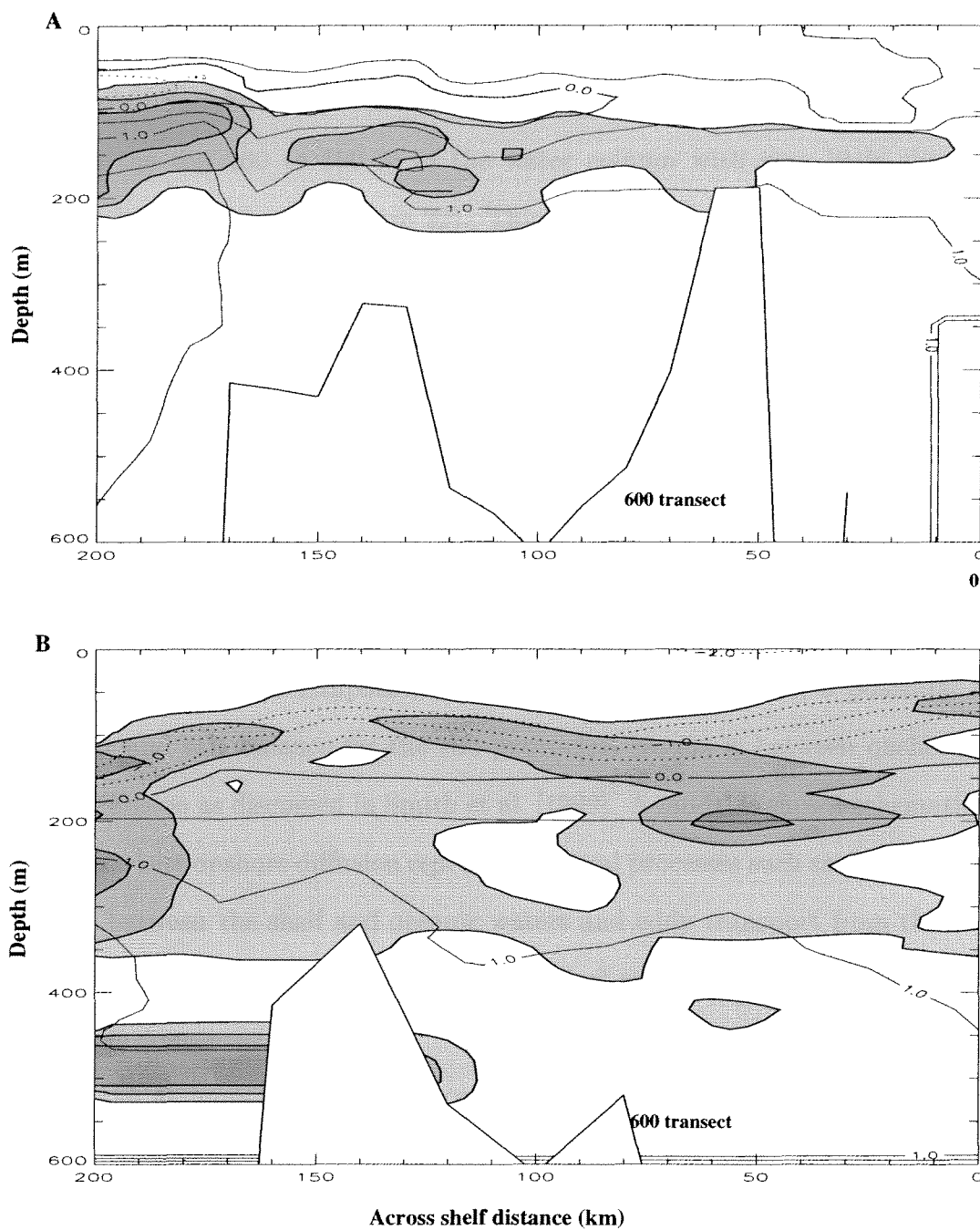
Figure 21. Fall and winter double diffusive heat fluxes for the 600 transect. Across shelf distribution of potential temperature (°C) for the 600 transect for the A) fall and B) winter 1993. The 5, 10 and 20 W m^{-2} double diffusive heat flux regimes are shaded as reference (lighter to darker for increasing fluxes). Temperature contours are for -2 to 1.5°C in 0.5°C intervals with dotted lines for negative values.

4.2 Bulk ocean budgets

The vertically averaged distributions of temperature and salinity indicate that most hydrographic variability between cruises during the 1993-94 sampling season occurred in the top 100 to 150 m of the water column with very little change in the sub-pycnocline waters (Figure 22). This result is consistent with the statistics calculated on the $\sigma=27.74$ (Figure 3) and confirms an analysis of historical data [Hofmann et al., 1996] indicating that the sub-pycnocline shelf waters to the west of the Antarctic Peninsula exhibit little variability over longer time scales. A station-by-station comparison of the temperature and salinity distributions [Klinck, 1998] indicates that subtle changes in the sub-pycnocline hydrography occurs and may be related to variability in the location of ACC relative to the west Antarctic Peninsula shelf break.

Given the persistent temperature and salinity characteristics, a potential first order heat and salt balance for the sub-pycnocline waters is between onshore and vertical diffusion as discussed in Smith et al. [1999]. A model is shown schematically (Figure 2) where onshore diffusion represents several processes such as diffusion down gradients between the shelf and oceanic waters and eddy transport from the ACC. Likewise, the processes represented in the vertical are down-gradient diffusion and double diffusion.

With the assumptions of a balance between onshore and vertical diffusion, (1) yields

$$HK_h^T\frac{\partial T}{\partial x} - LK_v^T\frac{\partial T}{\partial z} = 0$$

$$K_h^S H\frac{\partial S}{\partial x} - LK_v^S\frac{\partial S}{\partial z} = 0 \tag{40}$$

which is a set of two equations with four unknowns, K_h^T, K_h^S, K_v^T and K_v^S.
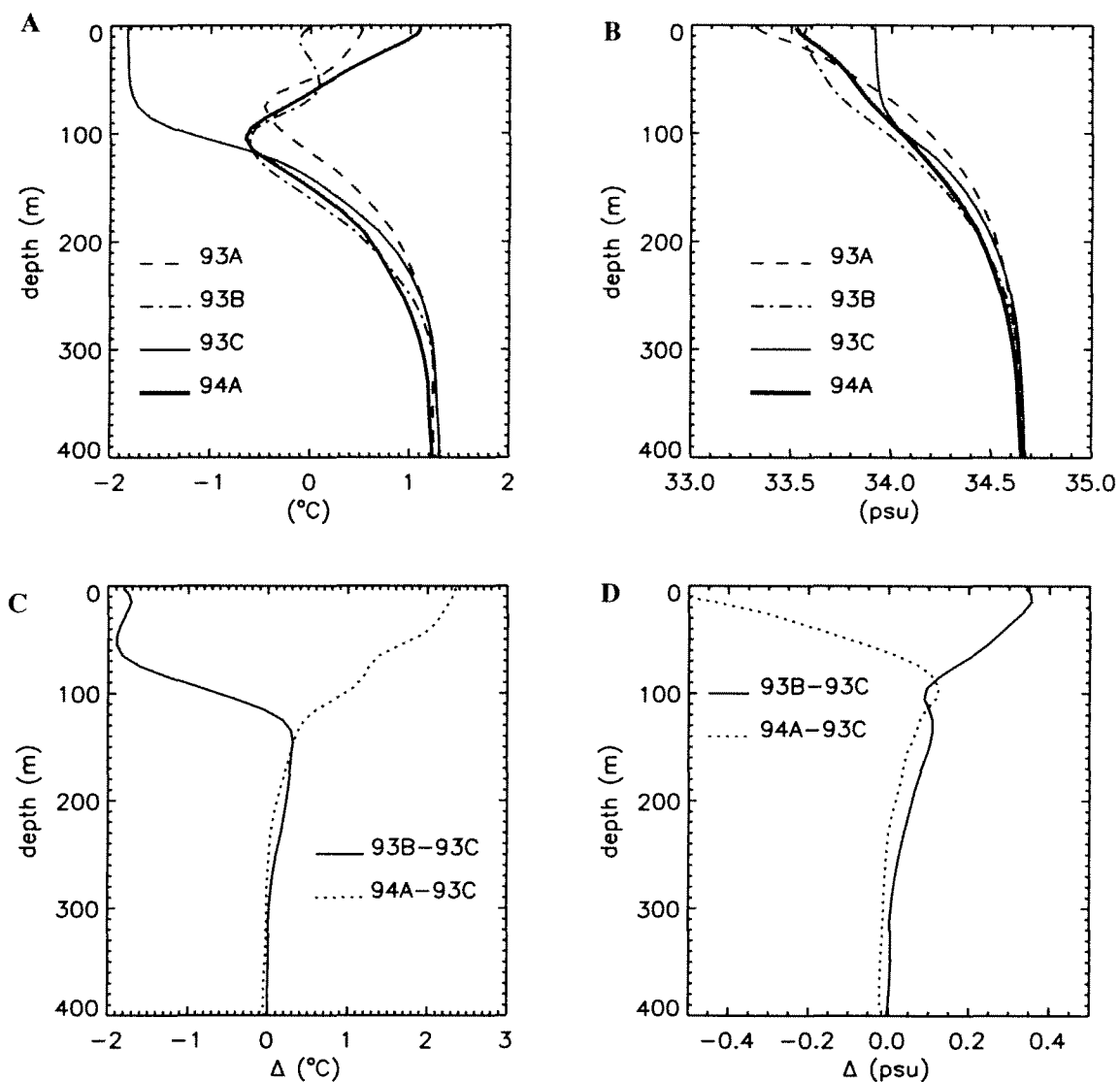
Figure 22. Shelf hydrography and hydrographic changes between cruises during the 1993-94 sampling season. Vertical distributions of the A) average temperature, B) average salinity, C) fall to winter and winter to summer temperature change and D) fall to winter and winter to summer salinity change calculated using observations from the west Antarctic Peninsula shelf.

The equations can be further reduced by assuming that horizontal diffusion is the same for heat and salt (i.e. $K_h^T = K_h^S$). Based on the results given in Section (4.1.3) the analogous assumption cannot be made in the vertical (i.e. $K_v^T \neq K_v^S$) thus allowing for differential, vertical transfer of heat and salt.

Given reasonable choices for horizontal diffusion of $K_h^T = K_h^S = 10$ to 100 m^2 s^{-1} [Klinck, 1998; Smith et al., 1999] the balancing vertical fluxes are found with $K_v^T = 1 \times 10^{-5}$ to 1×10^{-4} m^{-2} s^{-1} and $K_v^S = 8 \times 10^{-7}$ to 8×10^{-6} m^{-2} s^{-1}. The horizontal salinity gradient would need to be nearly an order of magnitude greater than observed to maintain a balance with $K_v^T = K_v^S$. This result is consistent (within an order of magnitude) with the results from the MC76 double diffusive calculation presented in the previous section (Section 4.1.3) and indicates that the observed sub-pycnocline hydrography can be maintained under the balance of horizontal and vertical diffusion. The most consistent balance is achieved with different vertical diffusion coefficients for heat and salt. double diffusion has an important role in the vertical transfer of heat and salt across the permanent pycnocline along the western Antarctic Peninsula.

Seasonal changes in the thermohaline properties of AASW occur (Figure 22) and the average heat and salt fluxes necessary to produce the observed changes can be found by

$$Q_H^{av} = \int_{z=h_l}^{z=h_u} \rho_o C_p \frac{\partial T}{\partial t} \cdot dz$$

$$Q_S^{av} = \int_{z=h_l}^{z=h_u} \rho_o \frac{\partial S}{\partial t} \cdot dz \tag{41}$$

where $\frac{\partial T}{\partial t}$ and $\frac{\partial S}{\partial t}$ are approximated by the temperature and salinity changes between cruises and the thickness of the AASW layer (0 to 110 m) defines the upper ($z = h_u$) and lower ($z = h_l$) limits for the integrals.

The observed AASW hydrographic changes from the fall (93B) to the winter (93C), correspond to an average heat flux loss of 47 W m^{-2} and a salinity fluxes of 1.5 mg salt m^2 s^{-1}. Conversely, the heat gain and flux of salt from winter to the summer (94A) are 40 W m^{-2} and -1.0 mg salt m^{-2} s^{-1}.

The time-integrated heat budget for the ice-free heat flux (Figure 23) shows an annual cycle in heating and cooling. Similar calculations which include the contributions from double diffusion and ice processes are also presented (Figure 23) as an indication of overall closure for the heat budget.

The average cooling for AASW between the 93B and 93C cruises is 73 W m^{-2} which is found by calculating the average slope of the solid curve in Figure 23 between days 110 and 225. The cooling is reduced to be 70 W m^{-2} (using the dashed curve in Figure 23) and 72 W m^{-2} (using the dotted curve in Figure 23) when accounting for heating from double diffusion and heat losses to ice, respectively. The average heating during the transition from winter to summer (93C to 94A) is 30 W m^{-2} and increases to 32 and 35 W m^{-2} when accounting for double diffusion and heat losses to ice, respectively.

The change in the salt content of the upper 100 to 150 m of the water column can be estimated for the same times as a consistency check on the local budgets (Figure 22b and d). Neglecting sources of salt from sub-pycnocline waters, the salt fluxes are consistent with ice growth/melt rates of approximately 0.25 to 0.5 cm day^{-1}. These rates are reasonable for the west Antarctic Peninsula continental shelf waters and would result in 0.25 to 0.5 m of ice in 2 to 3 months. The persistent, vertical flux of salt through the permanent pycnocline (salt source for AASW) could be balanced by precipitation rates on the order of 0.3 m yr^{-1} which are well within the precipitation rates recorded along the west Antarctic Peninsula (Section 3.4.5).
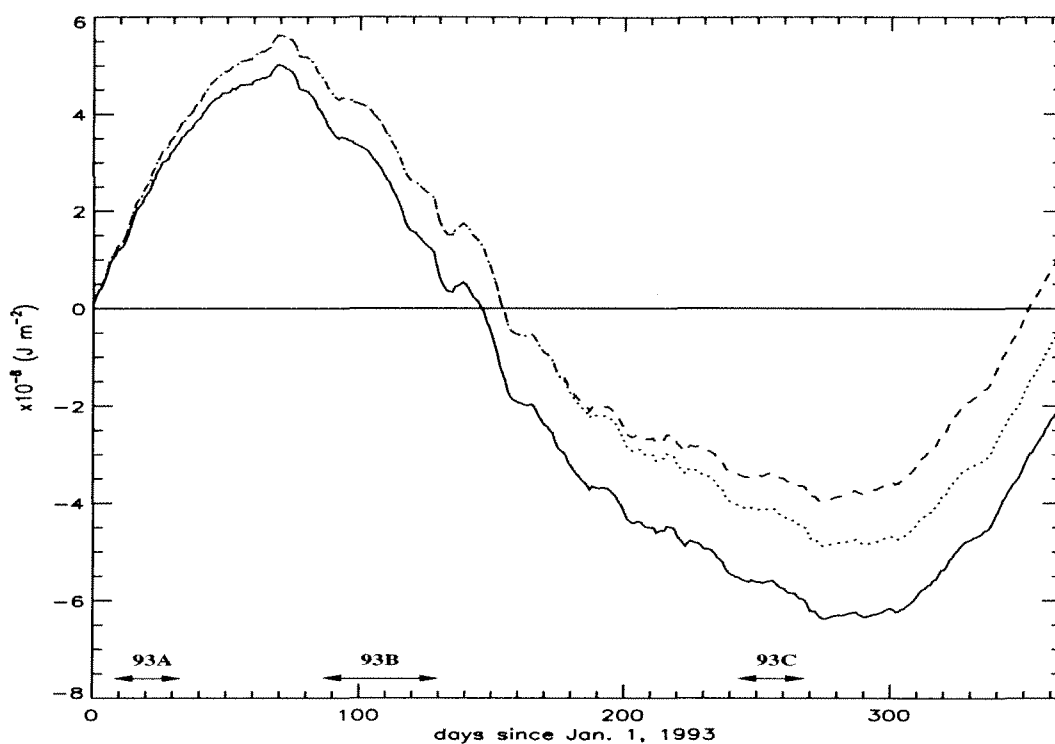
Figure 23. Time integrated 1993 heat budget $(\int Q_{open} \cdot dt)$. The solid line represents the integration for the ice free, surface budget only while the dashed line represents the calculation with an assumed double diffusive heat flux of 5 W m^{-2} into AASW from below the permanent pycnocline. The dotted line is the same as the dashed with an assumed 10 W m^{-2} heat loss included in the calculation during times when the west Antarctic Peninsula shelf is ice covered. The times of cruises are indicated with arrows and the solid, horizontal line provides the zero reference for the calculation.

4.3 Results from a thermodynamic ice-mixed layer model

4.3.1 Model initialization, forcing and spin-up

A coupled, dynamic-thermodynamic, ice-mixed layer model (Sections 3.3 and 3.4) is initialized with observed temperature and salinity from August 1993 (Figure 12a) and an idealized area-averaged ice thickness of $A_i h_i = 0.5$ m. The 1993 atmospheric time series from Faraday were repeated and used to force the model for an 8 year simulation so model spin-up and stability could be evaluated.

The simulated temperature and salinity of the mixed layer reproduced several key features of the ice-ocean system along the west Antarctic Peninsula including the timing of the ice cycle (i.e. timing of ice advance/melt and maximum extent), (Figure 24a-c) mixed layer depths (mld) and the depth of the permanent pycnocline. As in Kantha and Clayson [1994], the simulated mld is determined by the deepest point where the gradient Richardson number (Ri_g) exceeds the arbitrary threshold of 0.7 while the depth of the permanent pycnocline is determined by the depth 33.9 isohaline.

The simulated distribution of ice concentration adjusts from its initial winter conditions ($A_i h_i = 0.5$ m to 0.3 m) by the second winter (i.e. -0.2 m yr^{-1}). During the second through fourth winters, the simulated ice field increases its winter maximum ice thickness by approximately 0.02 m per year. After year 3, the simulation stabilizes with a maximum winter concentration of .35 m, gaining less than 1 cm yr^{-1} of area averaged ice cover during the last 4 years of the simulation.

The top 150 m of model undergoes a slow drift towards fresher conditions as seen in the salinity field (Figure 24c) with isohalines deepening over time. This drift can be seen in all isohalines; however, it is most evident in the 34.0 contour since this salinity is generally deep enough to be removed from seasonal processes associated with ice and surface forcing. A similar drift can be seen in the temperature field as the model spins-up with the top portion of the model tending towards colder
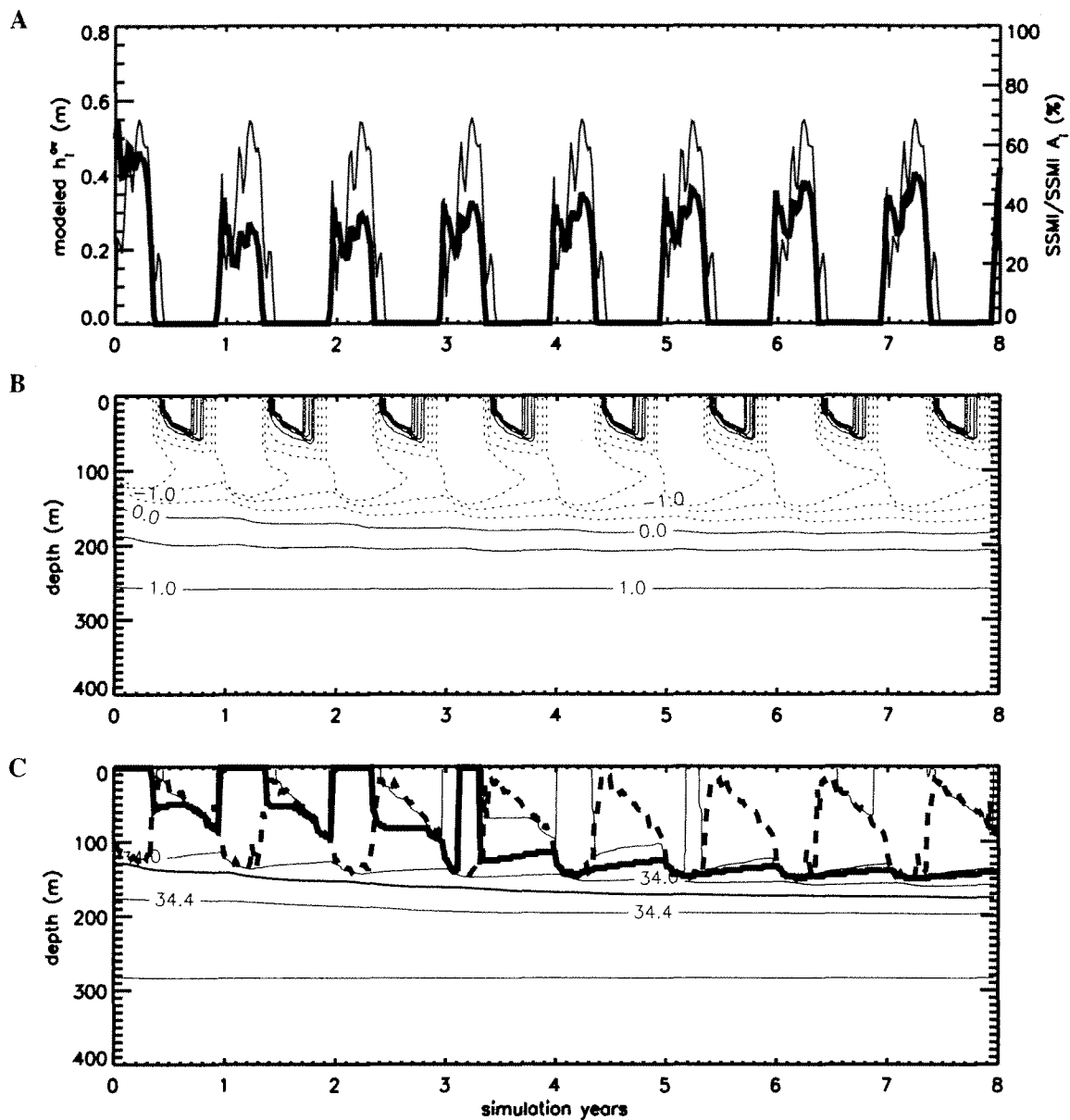
Figure 24. Simulated area averaged ice thickness and key hydrographic features for an 8 year model spin up. A) Area averaged ice thickness (thick line) and GSFC SMMR/SSMI near-Palmer ice record (thin line). B) Time and depth development of simulated temperature. Contours are for -2 to 2°C with a 0.5°C interval (negative contours are dotted). C) Time and depth development of simulated salinity. Contours are for 33.6 to 34.6 with a contour interval of .2. The position 33.9 isohaline is indicated with a thick line serves as a proxy for the depth of the permanent pycnocline. Mixed layer depths are illustrated by the thick dashed line.

conditions. This drift is most pronounced during the first four years of the simulation and most likely represents the period of time when the model adjusts its initial conditions to the prescribed forcing. Over the first four years, key features in the AASW (i.e. isotherms and isopleths) deepen at a rate of approximately 4 to 5 m yr^{-1}. After the fourth year, the model settles on a rate which is less than 1 m yr^{-1} and is considered to be stable. Some of this drift may be due to the oversimplification of precipitation (Section 3.4.5) or the missing physics associated with horizontal processes. As with the ice, the model appears to adjust after the fourth year when the simulated *mld* and the depth of the permanent pycnocline stabilize as suggested by a continuing deepening less than 1 m yr^{-1}. An annual cycle of the simulated *mld* and the depth of the permanent pycnocline develops and is discussed in the next section.

4.3.2 One year (1993) simulation

A one year record starting in the middle of model year 5 (01 January) is analyzed as the 1993 model simulation. The lack of recorded ice thickness along the west Antarctic Peninsula makes a direct comparison to observations difficult; however, the timing of growth and melt obtained from the simulations can be compared to the ice cycle observed in the near-Palmer GSFC SMMR/SSMI ice record (Figure 26). Simulated thermohaline distributions are compared to observed distributions as a further test of the model stability.

Ice cycle: Ice occurs in the model for 165 days (5.5 months) of the 365 day simulation (Figure 25a). Both observed and simulated ice fields, exhibit rapid growth beginning around day 150 (early May). The initial growth period lasts for several weeks and is followed by a period of alternating advance and retreat in ice cover. Around day 290 (mid-August), a rapid spring melt begins which persists until day 310 when the simulated ice cover vanishes. The transition from ice-covered to ice-
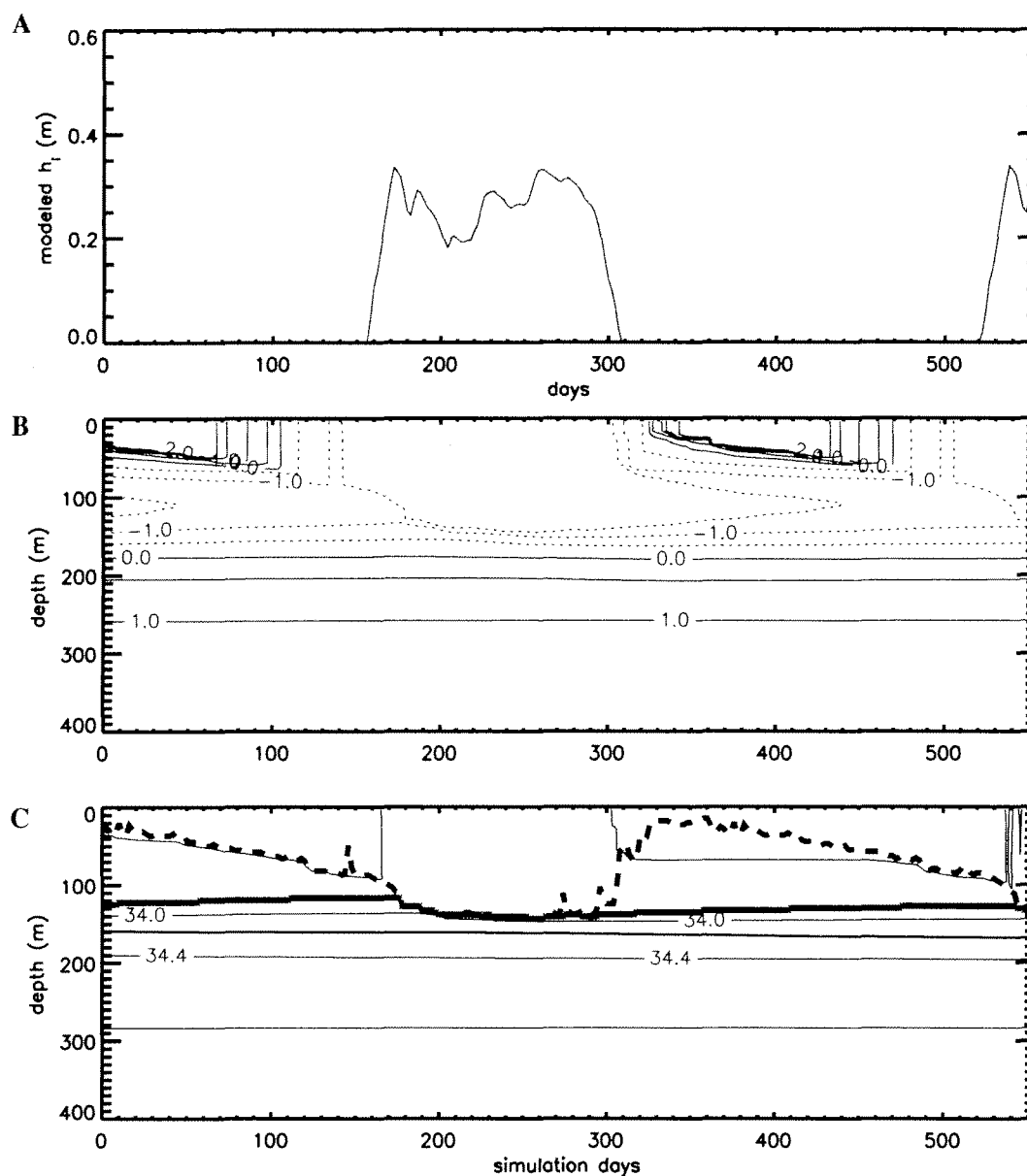
Figure 25. Simulated area averaged ice thickness and key hydrographic features for 1993. A) Simulated time distributions of area averaged ice thickness, B) depth and time distributions of temperature and C) salinity. Contour of model temperature with time. Temperature contours range from -2 to 2°C with a 0.5°C interval (negative contours are dotted) and salinity ranges are from 33.6 to 34.6 with a contour interval of 0.2. The position 33.9 isohaline is indicated by the thick, solid line and indicates the depth of the permanent pycnocline while mixed layer depths are indicated by the thick dashed line.

free conditions occurs faster in the simulated fields than in the observations (Figure 26a). Also, the model fails to reproduce the small observed peak between day 320 and 340. However, it is difficult to determine if the observed peak in ice cover at days 320 to 340 results from ice growth (thermodynamics) or from horizontal ice motion. Day 320 through 340 corresponds to a time of winds from the north which would tend to advect ice onshore. Horizontal advection is not allowed to contribute to changes in ice thickness in (23) and such an event would not be represented in the model. In addition to the overall timing of ice cycle, the ice simulations reproduce changes in ice thickness which occur on short time scales (a few days) (Figure 26a).

Heat fluxes and ice growth rates: During the rapid, initial ice growth (day 150 to 170 in Figure 26a), growth rates at the ice-ocean and the atmosphere-ocean interfaces are both positive (growth) and combine to produce a total growth rate on the order of 5×10^{-7} m s^{-1} (4 cm d^{-1}) (Figure 26b). This initial, rapid growth ends around day 170 when the growth at the base of the ice becomes negative and open ocean growth is reduced to nearly zero. From day 170 to the end of the ice cycle, melting at the ice-mixed layer interface is small with rates on the order of 0.3×10^{-7} m s^{-1} (0.5 cm d^{-1}) but persistent.

Throughout the 1993 simulation, the principal balance in (23) is between melting at the ice-ocean interface and growth at the atmosphere-ocean interface. The contribution from surface melting is significant only for a short time during the spring melt (e.g., notice that growth rates at the ice-ocean and atmosphere-ocean interfaces account for a large percentage of the total growth in Figure 26b). Periods of mid-winter ice retreat result when open ocean growth is either zero, or insufficient to counter the persistent melting at the ice-ocean interface. Conversely, ice growth is episodic and driven by ice formation in open water when oceanic ice formation is large compared to under ice melt. Many ice growth periods are characterized by
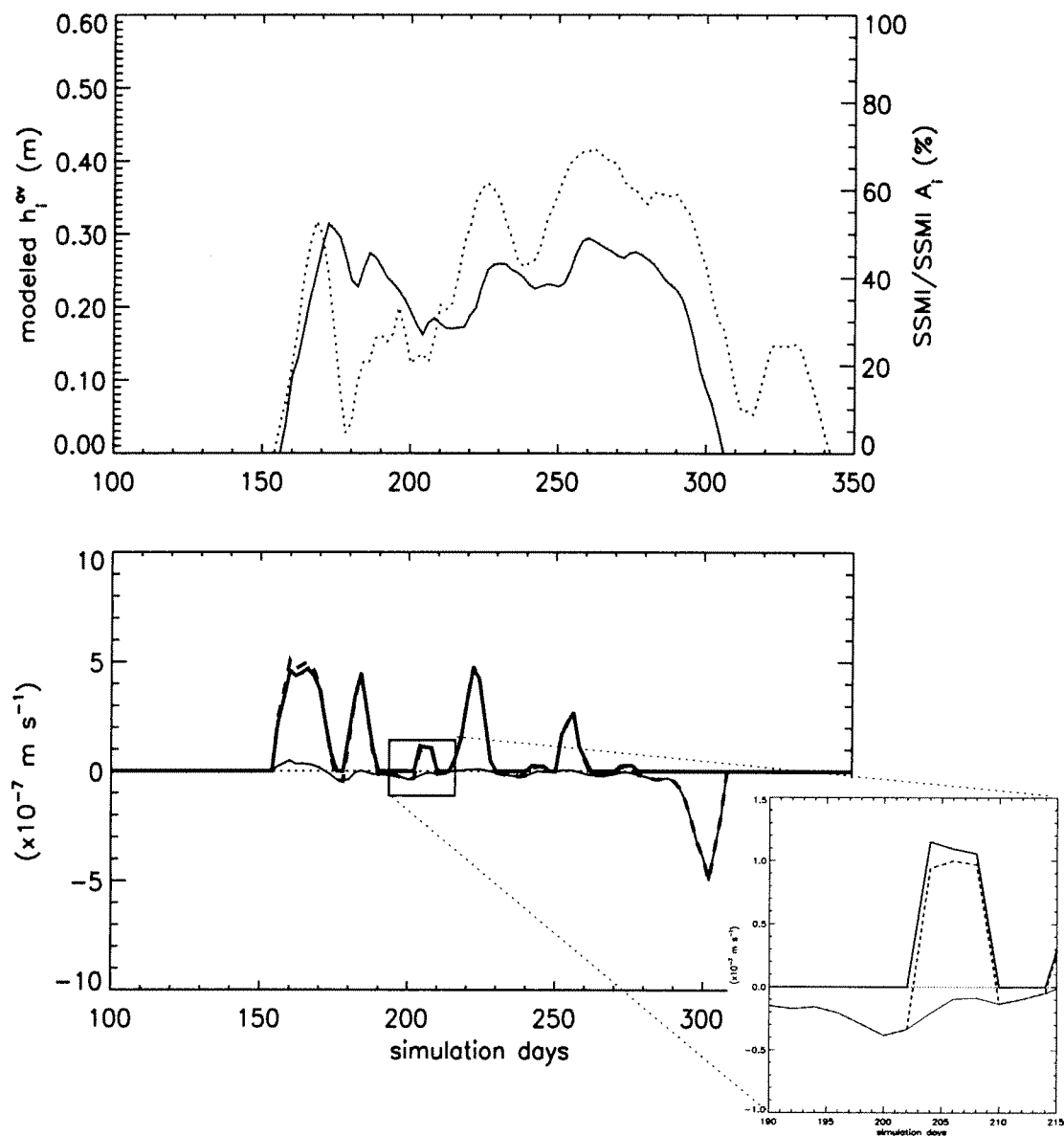
Figure 26. Simulated ice thickness, growth rates and the near-Palmer GSFC SMMR/ SSMI time series for winter 1993. A) Simulated (solid) and observed (dashed) sea ice for winter 1993. B) Simulated growth rates ($\times 10^{-7}$) for the simulation in A) with Wao (thick), Wio (thin) and total growth rate (W) (dashed) indicated. Zero growth is indicated with the horizontal dotted line and an expanded view of days 190-215 is provided in the insert.

open ocean growth rates in excess of 4×10^{-7} m s^{-1} (5 cm day^{-1}). An example of the competition between open ocean ice growth and melting under the ice is illustrated between days 185 and 200, at which time formation of ice in the open ocean is essentially 0 m s^{-1}, while melt rates at the base of the ice are on the order of 0.02 to 0.05 m s^{-1}. During this time, the area-averaged ice thickness is reduced by nearly 0.08 m. Open ocean growth rates becomes non-zero (around day 200), corresponding to cold atmospheric temperatures and large open ocean, sensible heat losses (see day 200 in Figures 16b, 18b,c and 26a,b), at which time ice grows.

The spring melt begins around day 290 (September-October) and is dominated by intense under-ice melting that occurs at a rate of 5×10^{-7} m s^{-1}, which is sufficient to reduce the ice cover from its maximum winter value to ice free conditions within 20 days.

The model open ocean heat budget is similar to the budget calculated in Section 4.1.2 (Figures 18c and 27a). In addition to heat fluxes calculated for ice-free conditions (Section 4.1.2) exchanges of heat between the AASW and the ice are included in the model (Figure 27b). Excluding the peak in heat flux between the AASW and the ice (Qio) around day 300, the average winter heat loss from AASW to the sea ice is 10 W m^{-2} (cooling surface waters). The peak ice-free heat flux is on the order of 100 W m^{-2} occurs during the spring melt, and is driven by solar warming. The elevated heat fluxes are initiated, and dominated, by heat input into the ice-free leads. Increased SST then drives the large, negative under ice melt and spring melt. As in the calculation of the ice-free heat budget (Section 4.1.2) the total, modeled heat flux (Figure 18a) becomes positive in the spring as a result of increased solar heating.

Salt fluxes associated with brine rejection and melting (Figure 27c) occur only with ice cover. Integrating the salt flux over the annual cycle results in a net input of fresh water which is equal to the prescribed precipitation (i.e., approximately
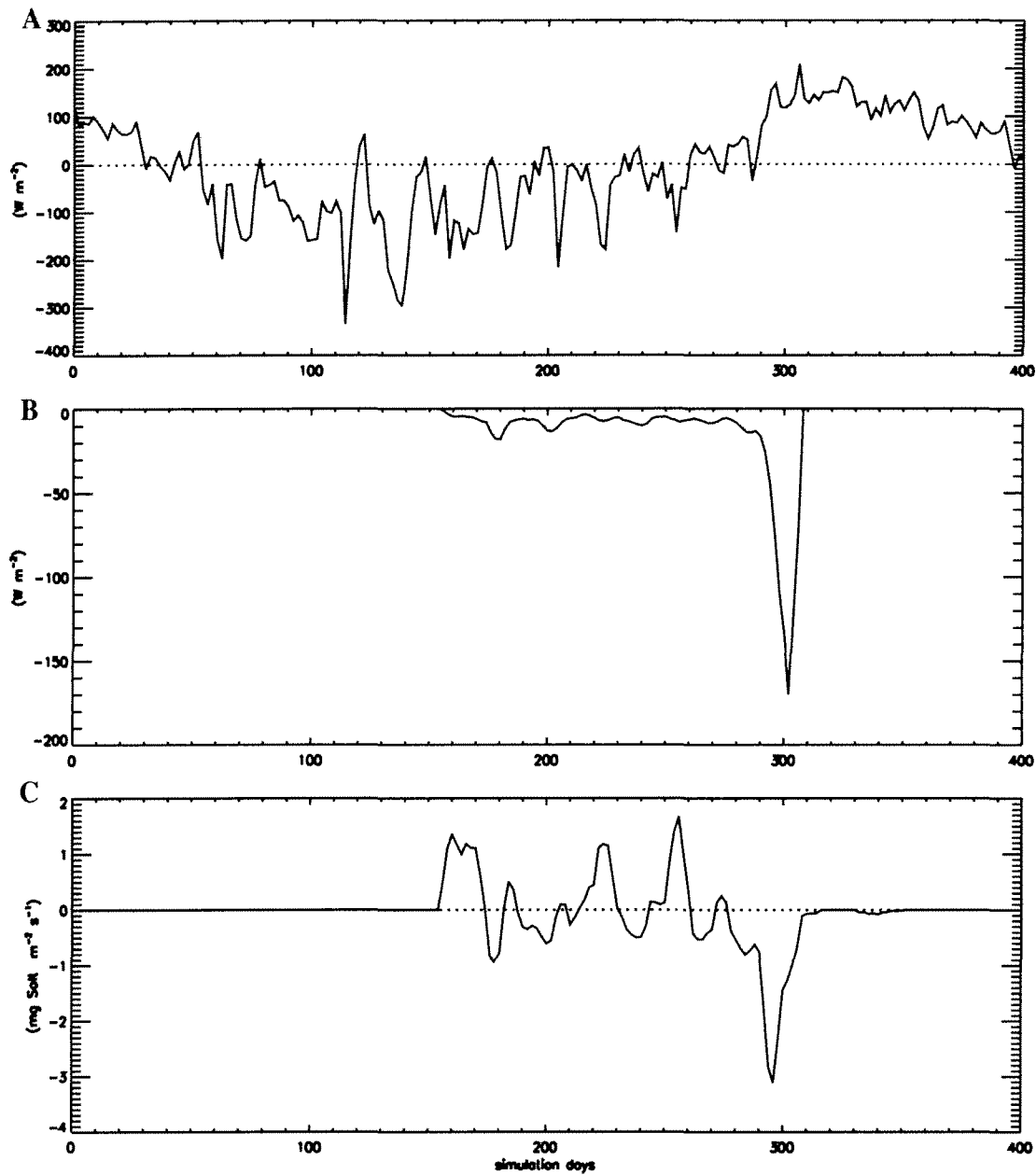
Figure 27. Heat and salt budgets from the 1993 simulation. A.) Simulated ice free heat budget calculated from the model using 1993 atmospheric data from Faraday station. B.) Simulated heat flux at the ice-ocean (Qio) interface (negative indicating heat loss from AASW). C.) Simulated salt flux associated with ice processes. Zero salt flux is indicated by the horizontal dotted line.

0.5 m). This comparison provides a consistency check and indicates that horizontal advective processes are not dominant and that the salt fluxes associated with the ice cycle are closed (i.e. freshening during ice melt cancels brine rejection during ice growth). The fresh water input via precipitation is needed to balance the persistent flux of salt from modified-UCDW to AASW.

Hydrographic cycle: Winter AASW hydrography is characterized by T=-1.9°C and S=33.8 extending from the surface to a depth of approximately 140 m (Figure 25b,c). These well mixed conditions persist throughout the winter period (day 200 to 300) of the simulation when ice cover is present. The surface layers warm, and freshen, around day 300 as surface heating drives the spring ice melt, which results in significant surface stratification (Figure 25b,c) and shallowing of the mixed layer (Figure 25c and 28a). The surface waters continue to warm (mainly) and freshen (slightly) throughout the summer due to solar heating and precipitation. The persistent erosion of the spring stratification can be seen as the *mld* deepens throughout the year due to surface wind mixing (Figure 25b,c). The simulated summer *mld* is typically between 40 and 80 m (Figures 25c and 28a,b) and peak surface temperatures and minimum salinities are 3°C and 33.65, respectively. These conditions are about 0.5 to 1°C warmer and 0.5 saltier than observed with the differences most likely due to insufficient surface mixing or the lack of horizontal processes in the model.

During the fall, surface temperatures decline under the influence of surface cooling (days 400 - 500, Figure 25b) which drives deeper mixing and accelerated erosion of the *mld*. Simulated surface salinities increase slightly during this time as deeper mixing injects salt into the upper water column. The salinity for AASW returns to winter values as sea ice forms and brine is injected into the surface waters. The simulated fall *mld* is around 80 to 100 m deepen to 120 m in the winter. Around
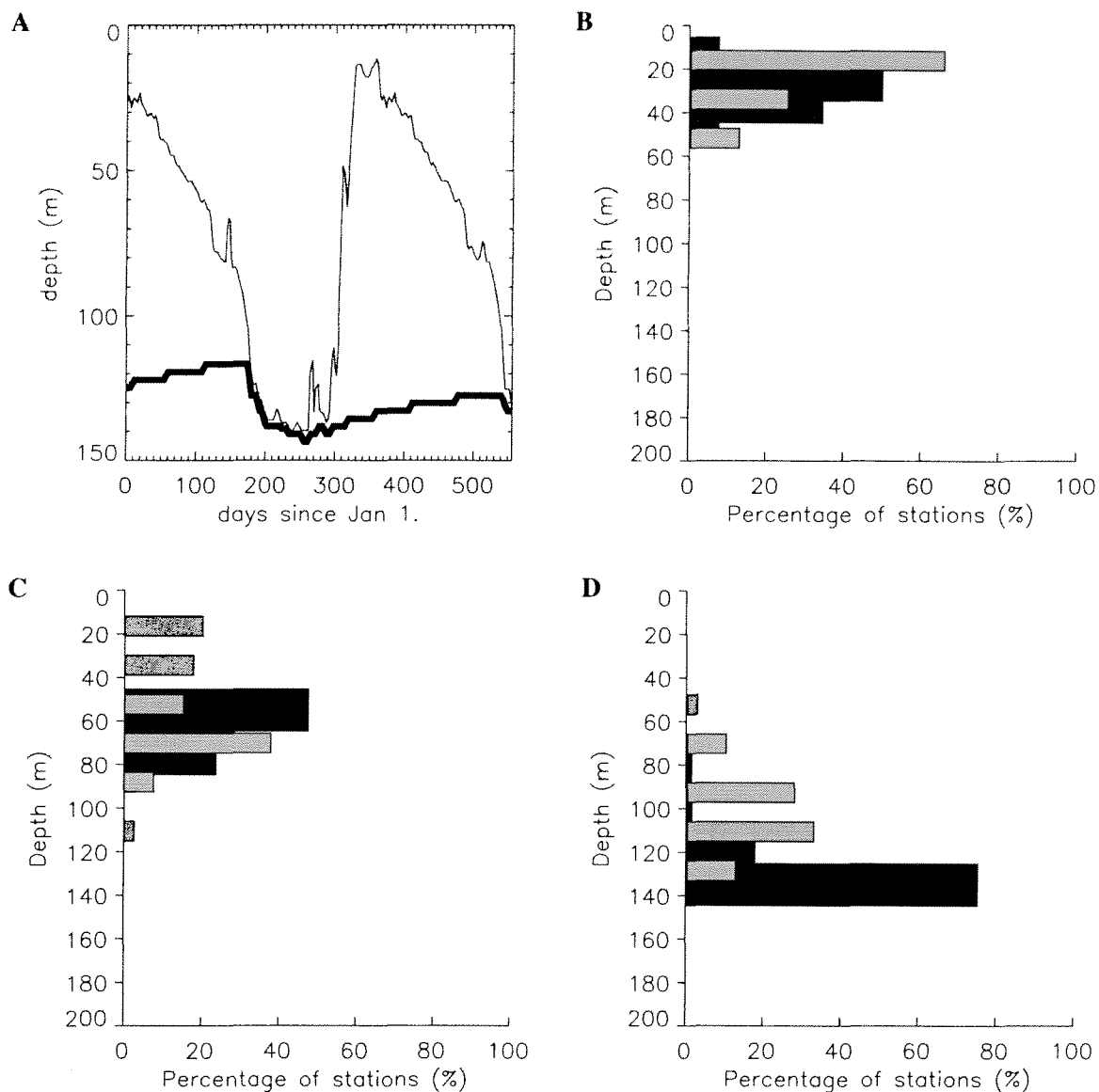
Figure 28. Simulated mixed layer and permanent pycnocline depths and hydrographic statistics. A) Simulated mixed layer (thin) and permanent pycnocline (thick) depths. Frequency distribution of simulated mixed layer depth for B) summer (0 < day < 60), C) fall (90 < day < 130) and D) winter (180 < day < 220). Times were chosen to coincide with the west Antarctic Peninsula cruises (Table 1).

day 150, the *mld* intersects the permanent pycnocline indicating that AASW is well mixed.

The permanent pycnocline is deepest (140 m) during the winter. When stratification exists within AASW (i.e. the formation of a seasonal pycnocline) the permanent pycnocline shallows somewhat as WW warms and becomes more salty from the input of heat and salt from below. This shallowing continues until stratification is eliminated within the AASW in winter and the permanent pycnocline depth is returns to its winter position. The overall trend in the simulated *mld* agrees with those from observations (Figure 28b-c); however, the model tends to mix excessively with *mld's* extending deeper than in the observations. This most likely is due to an over estimate of under ice stresses due to large ice velocities; a common result in models which use the free drift ice momentum equations [Steel et al., 1989].

Mixing regimes: The 1993 simulated ice field and two of individual components of the vertical mixing scheme (Sections 3.3.2 and 3.3.4) are presented in Figure 29. The MY2.5 turbulence closure scheme determines the mixing depth due to competing factors of wind induced mixing and buoyancy forcing. The deepest mixing occurs in the winter when freezing causes brine rejection and surface stress includes mixing at the open water interface and from under ice sources. Simulated winter mixing reaches depths of 120 to 140 m corresponding to mixing coefficients on the order of 0.1 to 0.01 m^2 s^{-1}. The shallowest penetration of turbulent mixing occurs during the spring as a result of surface stratification due to fresh water input from melting ice and from surface heating. Simulated spring mixing coefficients are typically 0.01 to 0.001 m^2 s^{-1}.

Mixing associated with double diffusion ($K_{dd}^T = 5 \times 10^{-5}$ to 10^{-4} m^2 s^{-1} and $K_{dd}^S = 5 \times 10^{-6}$ to 10^{-5} m^2 s^{-1}, respectively) occurs throughout the simulation; the maximum double diffusive heat flux is about 10 W m^{-2} (Figure 30a). Consistent
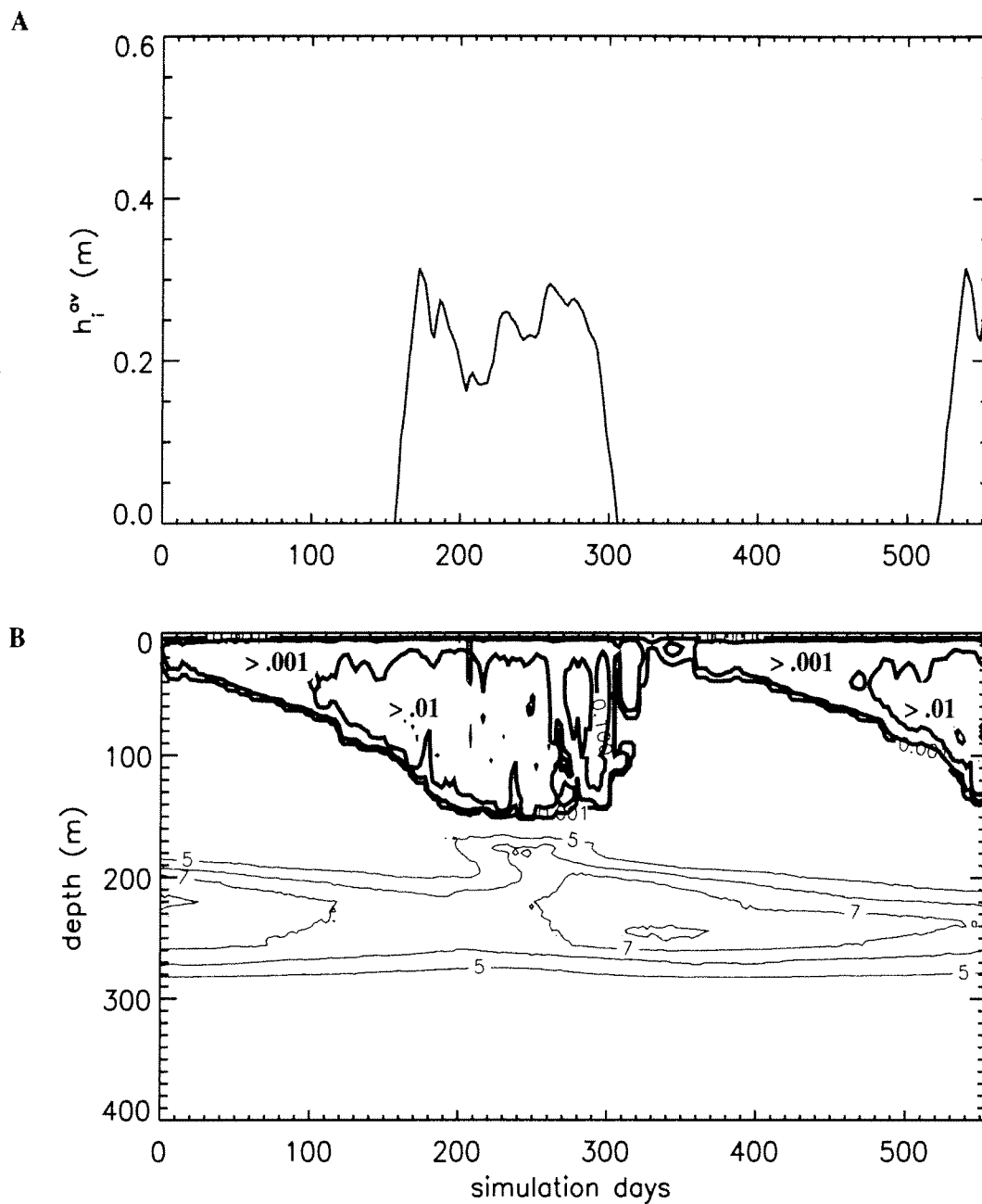
Figure 29. Mixing regimes during the 1993 simulation. A) Simulated, area-averaged ice thickness. B) Simulated vertical mixing coefficients for heat. Mixing coefficient associated with the MY2.5 scheme are indicated with thick contours while the coefficient associated with double diffusion are indicated with the thin contours. Contour levels for the MY2.5 mixing coefficient are 0.001, 0.01 and 0.1 while contour levels for double diffusion are 3×10^5 to 10×10^5 with a contour interval of 1×10^{-5}.

with the hydrographic data (Section 4.1.3), the maximum effects of double diffusion occur in the mid-pycnocline. where vertical gradients in temperature and salinity are maximum (Figure 29b). Gradient Richardson mixing contributes only for a few time steps during spring when surface stratification significantly reduces the ability of turbulence closure to break down the surface stratification. Otherwise, the vertical mixing coefficient from the MY2.5 turbulence scheme ($K_v^{MY2.5}$) is several orders of magnitude larger than any other mixing processes in the model, and thus, dominates mixing in the water column.

Nudging: The contribution of the nudging terms in (18) and (19) to the simulated distributions is found by vertically integrating (22) (using $\rho_o C_p T$ for heat and $\rho_o S$ for salt) from the surface of the model to the bottom. The resulting fluxes are the sources of heat and salt necessary to maintain the hydrographic character of the modified-UCDW (Figure 30a) and serve as an internal consistency check for how well the model is performing.

Results from this integration (Figure 30a) indicate that typical values for the replacement fluxes of heat (Q_{nudge}^T) and salt (Q_{nudge}^S) are 8 to 12 W m^{-2} and 0.5 to 0.6 mg salt m^{-2} s^{-1}, respectively and are fairly persistent throughout the simulation.

The integrated heat and salt fluxes in Figure 30a can be converted to effective mixing coefficients and compared to the results of the box model calculation presented in Klinck [1998] and in Smith et al.[1998]. These fluxes are converted using

$$K_h^T = \left(H Q_{nudge}^T \right) \left(\rho_o C_p \frac{\partial T}{\partial x} \right)^{-1}$$

$$K_h^S = \left(H Q_{nudge}^S \right) \left(\rho_o \frac{\partial S}{\partial x} \right)^{-1} \tag{42}$$

where shelf dimensions and hydrographic values are summarized in Figure 2. The

resulting mixing coefficients from (42) are approximately 15 m^2 s^{-1} for heat and salt (Figure 30b) which are similar the the values presented in Klinck [1998] and in Smith et al., [1999] and balance vertical heat losses associated with the vertical mixing terms in (18).

4.3.3 Sensitivity to sub-pycnocline heat fluxes

Given the potential source of heat and salt to AASW from the sub-pycnocline modified version of UCDW (Section 2.2.1), a series of numerical experiments were designed to test the sensitivity of the simulated distributions to the sub-pycnocline water is presented in this section. As in the reference 1993 simulation, each experiment was initialized with the hydrographic distributions illustrated in Figure 12a and spun up to a similar state of equilibrium. Results from the from these equilibrium (fifth year) of each simulation are compared to the fifth year results from the 1993, reference simulation.

The experiments are divided into two categories: sensitivity to changes in the temperature of the sub-pycnocline waters, and sensitivity to the parameterization of the double diffusive fluxes of heat and salt.

Temperature of the sub-pycnocline water: The initial conditions associated with the shelf sub-pycnocline waters (Figure 12a) were shifted by -0.75, -0.50, -0.25, 0.25, 0.50 and 0.75°C giving a total range in sub-pycnocline temperatures of 0.45 to 1.95°C. All other model processes and parameters are held constant. The lower end of the temperature range is colder than any shelf measurements in the historical data base [Hofmann et al., 1996] while the upper end corresponds to temperatures associated with UCDW found on the oceanic side of the shelf break Smith et al. [1999].

Increasing the temperature of the sub-pycnocline water reduces the overall thickness of the ice at the time of maximum winter ice extent (day 290) (Figure 31a)
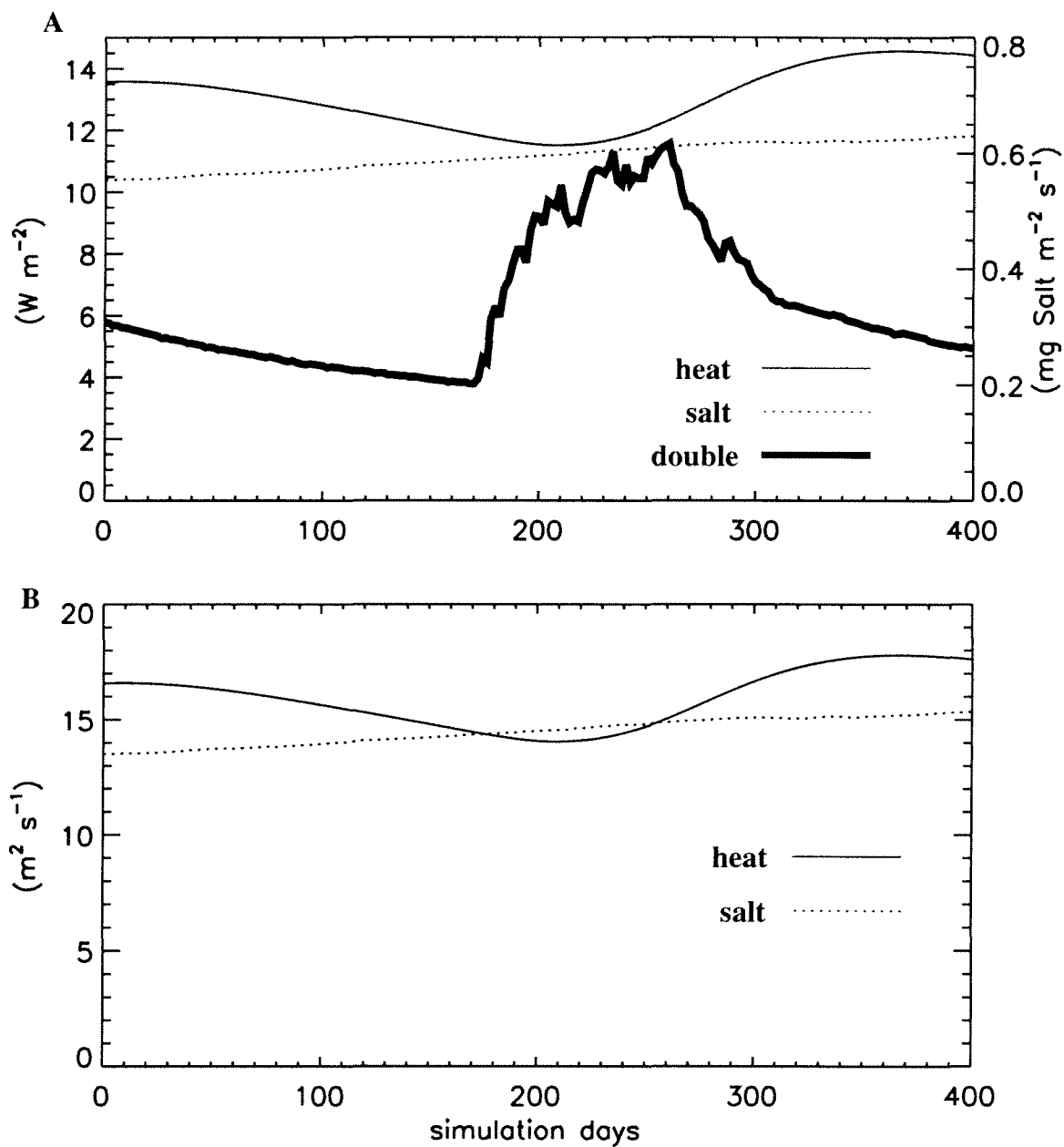
Figure 30. Oceanic fluxes of heat and salt through the permanent pycnocline during the 1993 simulation. A) Vertically-integrated heat and salt fluxes resulting from nudging (Equation 22) with the maximum double diffusive heat flux. B) Horizontal diffusion coefficients for heat and salt (Equation 1) calculated from the vertical fluxes of heat and salt in A).

while decreasing the temperature results in thicker ice. A temperature increase of 0.75°C reduces the average ice cover by half (Figure 31c) while decreasing the temperature by a factor of two results in 30% increase in simulated ice cover (Figure 31c).

The timing of the ice cycle is unaffected by changes in the sub-pycnocline temperature. In all simulations, rapid ice growth starts around day 150 and lasts for several weeks. Similarly, the spring ice retreat begins near day 290. Ice-free conditions occur earlier in the simulation with thinner ice (warmer sub-pycnocline water) but this is due to a smaller quantity of ice rather than an increased melt rate.

Simulated mixed layer and permanent pycnocline depths were only slightly affected by the changes in the sub-pycnocline temperature. Shallower *mld* resulted in simulations with thicker winter ice (cooler sub-pycnocline temperatures) while deeper *mld* were produced with reduced ice cover (warmer sub-pycnocline temperatures). The depth of the permanent pycnocline changes very little.

Parameterization of double diffusion: The mixing coefficients associated with double diffusion (K_{dd}^{T} and K_{dd}^{S}) were scaled by factors of 0.0, 0.5, 1.5. 2.0 and 3.0 while all other model processes and parameters held constant. Removing double diffusion ($K_{dd}^{T,S}=0$) resulted in a 50% increase in average winter ice thickness, while doubling double diffusion resulted in averaged winter ice thickness reduced by nearly 50% (Figure 31b,d). If double diffusion is increased by a factor of three, ice free conditions occur during mid-winter (day 224, Figure 31b).

As found for the simulations with modified sub-pycnocline water temperatures, the effect of changed vertical heat fluxes on simulated ice thickness at the time of maximum winter ice extent was less pronounced than for the average winter ice thickness (Figure 31d). The timing of the ice cycle was essentially unchanged with different double diffusive fluxes.
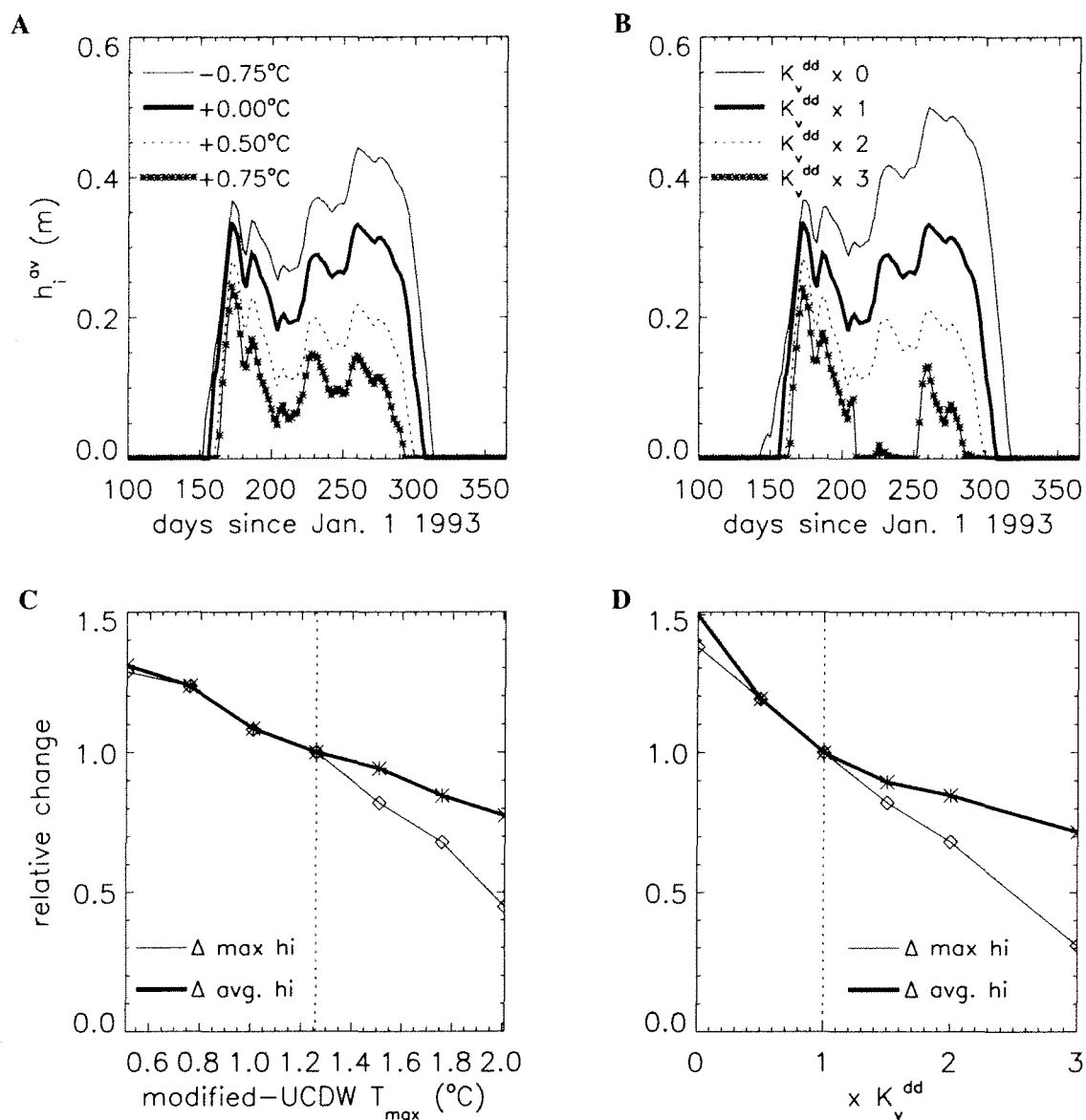
Figure 31. Area averaged ice thickness with changes in sub-pycnocline temperatures and double diffusive parameterization. A) Simulated area-averaged ice thickness for the reference case (temperature shifted by $0°C$) and with shifts in the sub-pycnocline temperatures. B) Same as A) except for changes in the parameterization of double diffusion (K_v^{dd}) C) Changes in maximum winter ice thickness and average winter ice thickness for simulations presented in A) (the reference simulation is indicated with the vertical dotted line) D) Same as C) except for simulations presented in B).
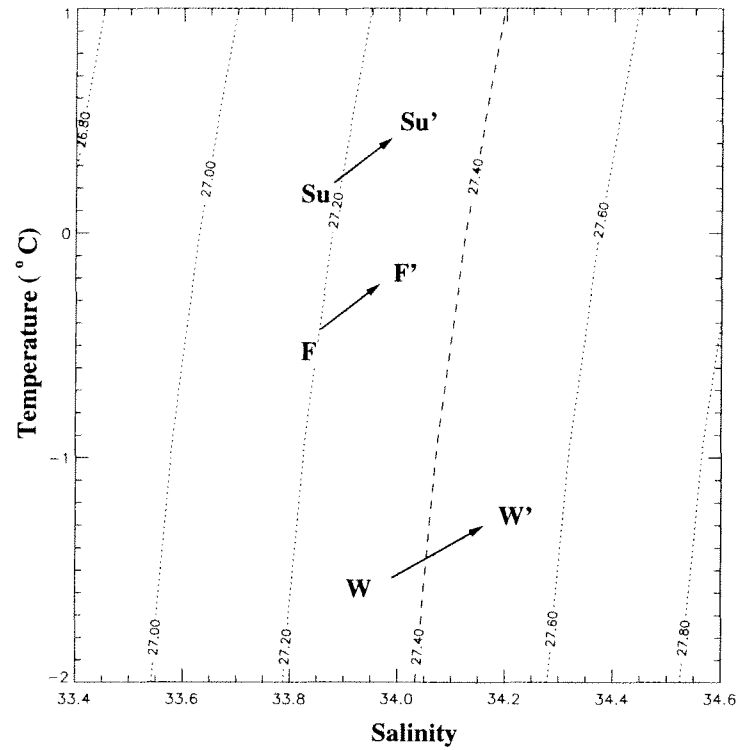
Figure 32. Surface water temperature and salinity averages for the base 1993 simulation with double diffusive effects turned off. Simulated, average winter (W), fall (F) and summer (S) temperature (°C) and salinity (psu) for AASW from the 1993 reference simulation (non-prime) and from a simulation using a constant background diffusive flux instead of the double diffusive mixing scheme (').

Changes in double diffusive heat fluxes and horizontal heat replacement from the nudging (Figures 29 and 30a) have similar effects. Increases in double diffusion produce slightly deeper spring *mld* due to reduced ice cover while reductions in double diffusion results shallower *mld* due to increased ice cover. The depth of the permanent pycnocline is slightly shallower for simulations with increased K_{dd}.

An additional simulation done in which the double diffusive effects were replaced by a constant background diffusion of (α_{bkgrnd}=5×10^{-5} m^{-2} s^{-1}) for both temperature and salinity. This simulation represents the default mixing scheme used in the MY2.5 mixing scheme. The simulation produces reasonable temperatures for AASW (Figure 32), but salinities are generally too high. In particular, winter AASW salinities are in excess of the maximum observed winter values of 34 [Hofmann and Klinck, 1998].

4.3.4 16 year (1978-1994) simulation

The sixteen year record (1978-1994) of atmospheric conditions at Faraday Station provide the opportunity to simulate ice conditions which can be compared to the GSFC SMMR/SMMI ice observations from the same time period. The reference 1993 simulation (discussed in the previous section) is used as initial conditions for the sixteen year simulation. The daily average meteorological conditions at Faraday Station force the 1978-1994 simulation.

The modeled ice cycle reproduced many of the high/low (as defined by departure from the sixteen year average [Smith et al., 1996]) ice years observed in the GSFC SMMR/SSMI ice field (Fig 33a,b). In particular, the model reproduced the record low and high ice years in 1989 and 1987 reported by Comiso et al. [1993] and others. As in the observed ice field, the model simulated high ice years in 1980, 1981 and 1982 and low ice years in 1983, 1984 and 1985. The high ice conditions in 1980 was not produced by the model and may result from imposing climatology in the
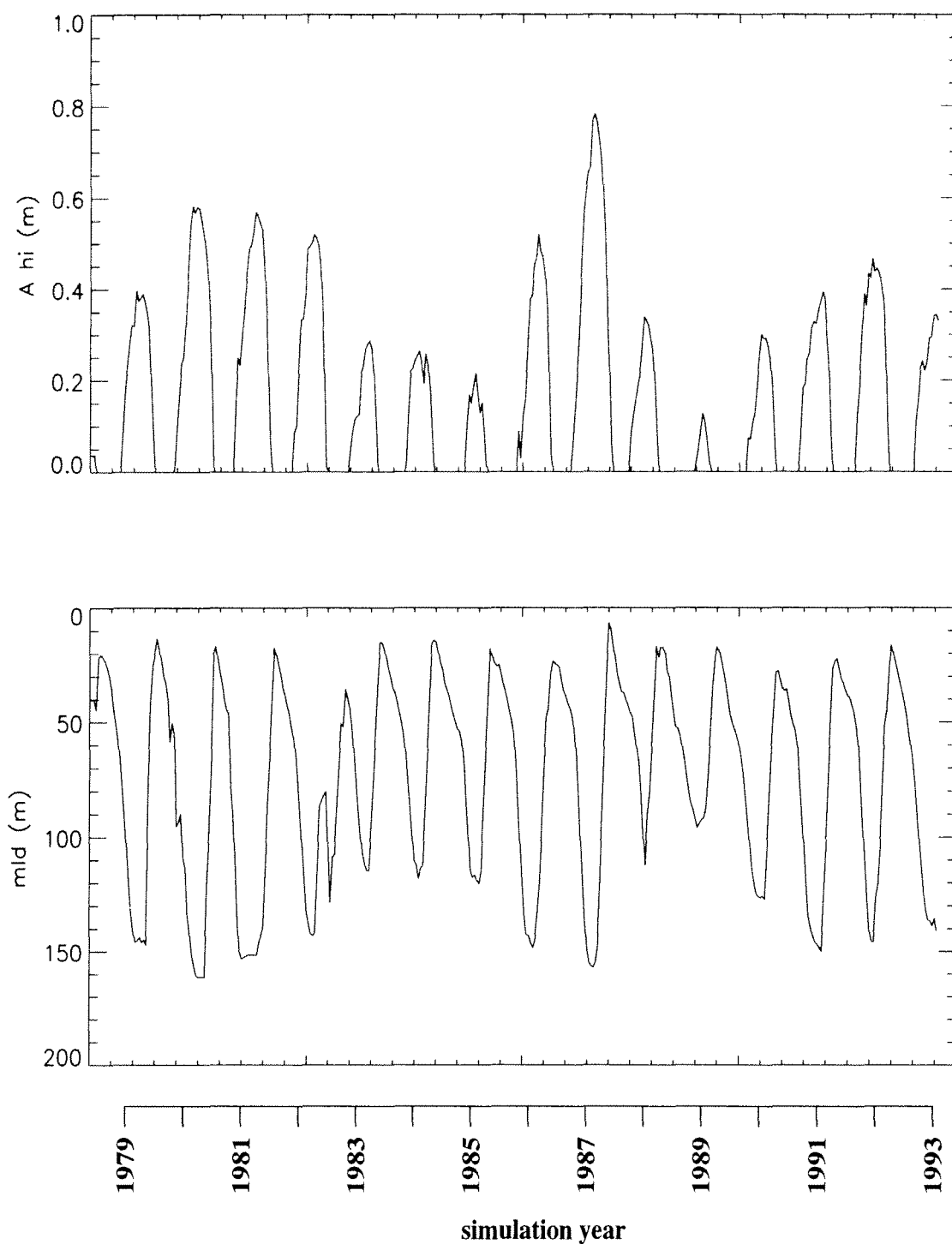
Figure 33. Results from a simulation forced with daily averaged atmospheric conditions from Faraday Station over a 16 (1978-1993) year period. A.) Simulated area-averaged ice thickness and B.) the depth of the mixed layer.

sub-pycnocline waters through nudging. Minimum spring *mld* were 10 to 30 m, with the deeper *mld* following years with low ice cover (Figure 33b). The depth of the permanent pycnocline was nearly 50 to 70 m shallower in low ice years (Figure 33b).

CHAPTER 5

DISCUSSION

The ice-free heat flux calculation (Section 4.1.2) provides a context for evaluating, ranking and quantifying important processes which affect the of sea-ice distribution and hydrographic structure of the west Antarctic Peninsula continental shelf. In addition, the numerical simulations provide a mechanism to investigate processes at the atmosphere/ice/ocean interface and to evaluate the assumptions used in the open ocean heat budget. In this section, the results from the previous section will be discussed and, whenever possible, comparisons will be made to other relevant studies in this and other regions.

5.1 AASW heat budgets

5.1.1 Surface heat budget

The ice-free heat budget for summer months (Figure 18c) is dominated by input from short wave radiation (Q_{sw}) while the winter budget is dominated by episodic sensible (Q_{sens}) heat losses. Summer values for the daily-averaged short wave radiation can exceed 200 W m^{-2} (Figure 16a) making it the most significant term in the heat budget. The small temperature differences between the atmosphere and AASW at this time result in little contribution from sensible heat exchanges (Figure 16b,e and 18b). During the winter, small zenith angles shorten the length of daylight for the region thereby diminishing the importance of short wave radiation while large temperature differences between the atmosphere and AASW result in sensible heat losses at the air-sea interface that are on the order of 100 to 150 W m^{-2}.

The latent heat flux (Q_{lat}) is generally the least significant term in the heat budget with magnitudes 4 to 10 times smaller than sensible fluxes. Evaporation (and consequentially, latent heat fluxes) is low for the region a result of high, 80% to 90%

relative humidity (Figure 16c). Low evaporative heat losses agree with observations in Cullather et al. [1998] who indicate that the west Antarctic Peninsula region is characterized by net precipitation over evaporation.

Net long wave radiation (Q_{lw}) is predominantly negative throughout the year, indicating that the ocean surface radiates more heat as long wave radiation than it receives. This arises because SST is generally warmer than the atmospheric temperatures throughout the year and because clouds remove part of the incoming radiation. The annual average for long wave radiation is approximately 30 W m^{-2} with modest variations created by changes in cloud cover and air temperature. There is an apparent seasonal trend in long wave radiation (Figure 18a), with winter values being slightly smaller than the summer. This reduction results from ice cover which reduces the area of open water, thus reducing the heat flux.

5.1.2 Total heat budget for surface waters

The time-integrated 1993 heat budget shows AASW losing more heat to the atmosphere than it gains making it a source of heat for the atmosphere (solid line in Figure 23). Winter SST is warm (approximately -2°C) compared to the atmosphere, which is typically colder than -10°C, and winter sensible heat losses are in excess of 100 to 150 W m^{-2}. This result indicates the importance of sea-ice since the large heat loss occurs only through the fraction of the ocean which remains ice-free. Under the assumption that ice acts as a perfect insulator, sensible heat loss would be zero if the shelf were completely ice covered, thus eliminating this source of heat for the atmosphere.

Despite AASW being a heat source for the atmosphere during 1993, there is no evidence in the hydrographic observations for the period showing that AASW experienced any significant cooling between the summer of 1993 and 1994 (Figure 22a). This result agrees with the low net heating between 1993 and 1994 found by

Klinck [1998] which was typically on the order of 5 W m^{-2} (the actual net heating depended on the exact station but was never found to be in excess of 25 W m^{-2}). The integrated 1993 heat budget (solid line in Figure 23) closes to within 25 to 30% of its maximum. Since there is no observed change in the heat content of AASW during the summers of 1993 and 1994 the heat lost must be accounted for by another source. Potential heat replacement processes include horizontal processes, vertical heat fluxes through the permanent pycnocline and heat exchanges between AASW and sea-ice.

Conservative estimates for vertical heat flux from calculations in Klinck [1998] and Smith et al. [1999] are between 5 and 10 W m^{-2}. Including this persistent heat source to AASW in the integration (dashed line in Figure 23) indicates that 5 W m^{-2} is more than enough heat to close the budget and predicts that AASW should gain heat throughout the year but closes the budget to within 10% to 15%. The integrated 1993 budget is closed within 5% of its maximum by including heat exchanges between AASW and the sea-ice with the persistent vertical heat flux calculated above (dotted line in Figure 23). The calculation is performed by prescribing a heat loss of 10 W m^{-2} when the GSFC SMMR/SSMI record indicates the presence of sea ice, an assumption which is later justified by the model results.

The closure of the vertical processes in the above heat budget does not diminish the possibility that horizontal fluxes of heat (and salt) are necessary to completely close the budget; however, they do suggest that much of the local variability observed in AASW can be explained by vertical processes. A further indication of the validity of the budgets can be found by calculating average, net heating between individual 1993 cruises (i.e., the slope of the curves in Figure 23) and comparing them to the observed changes in heat content within AASW calculated in Klinck [1998]. Average heating, cooling rates, from Figure 23 are on the order of ±50 W m^{-2} and are in agreement with values reported by Klinck [1998].

5.1.3 Validity and limitations of the surface heat flux calculation

The heat fluxes presented in Section 4.1.2 were calculated using data from around Palmer and Faraday Stations located mid-way along the Antarctic Peninsula (Figure 8). The validity of the calculation for the remainder of west Antarctic Peninsula continental shelf remains to be demonstrated. The estimates of sensible and latent heat exchanges are particularly sensitive to atmospheric conditions which may be different offshore whereas short wave radiation is basically estimated from time and geographic location. Klinck and Smith [1995] compare the atmospheric conditions measured at Palmer Station to ship-based measurements recorded during the two month, cruises in fall, 1993 (Table 1). While air temperatures recorded at the station are fairly representative of the conditions over the shelf, wind speed and direction are poorly represented. Smith [1996] compared AWS data from Palmer Station to ASW data from other stations along the coast and found that there was an alongshore gradient in atmospheric temperatures with colder conditions to the south. Given these two results, care must be taken in interpreting heat flux calculations outside of the area surrounding Palmer and Faraday Stations. These results are reasonably accurate for a region within 50 km of Palmer Station (i.e., the arc where GSFC SMMR/SSMI data were extracted in Figure 8). Outside of this region, the results are likely qualitatively correct. The trends in the heat budget, and the relative importance of the individual components most likely stay the same; however, the magnitude of the calculations should change.

5.2 Temporal variability in the winter heat budget

All of the components of the heat budget exhibit variability on time scales of a few days to weeks (Figures 18a-c) which corresponds to time scales associated with the passage of synoptic low pressure systems through Drake Passage. In this section, the effects of one low pressure on the atmospheric conditions and heat fluxes will

be examined as the system passes through Drake Passage during the winter of 1993 (Figure 34).

5.2.1   Temporal variability in the winter sensible heat budget

Mid-winter reversals in temperature and wind direction often coincide with the passage of a low pressure system to the north of the Antarctic Peninsula (Figures 34 and 35). For several days prior to the passage of a synoptic low pressure system, winds are out of the south and atmospheric temperatures are low. During this time, the total heat budget (dominated by sensible fluxes) is characterized by heat losses which are on the order of 100 W m^{-2} (day 240 in Figure 18). When a low pressure system forms to the west of the Peninsula (Figure 34b) atmospheric temperatures increase, winds reverse and sensible heat changes becomes zero (and slightly positive) for several days. After the low pressure system passes the Antarctic Peninsula, air temperature drops, the wind reverse and large heat losses from AASW to the atmosphere occur.

At the time of the passage of the low pressure system (day 230 to 250), the GSFC SMMR/SSMI ice record indicates a 33% reduction in ice cover (Figure 35c). While it is tempting to link the reduction in ice cover to increased atmospheric temperature, and decreased sensible heat fluxes it is unlikely that ice melt is responsible for all of the change. Factors associated with ice motion, not included in this analysis, are also likely to play a role in this change. Winds blowing from the north would tend to pile ice along the coast (increasing A_i), while transporting ice south and out of the domain (decreasing A_i). Thermodynamic effects associated with ice melt will be discussed in more detail in the modeling section of this chapter.

The cumulative effects of the passage of low pressure systems during 1993, and the impact that they have on atmospheric conditions along the Peninsula (Figure 17) indicate that winds from the north (geostrophic flow around a low pressure
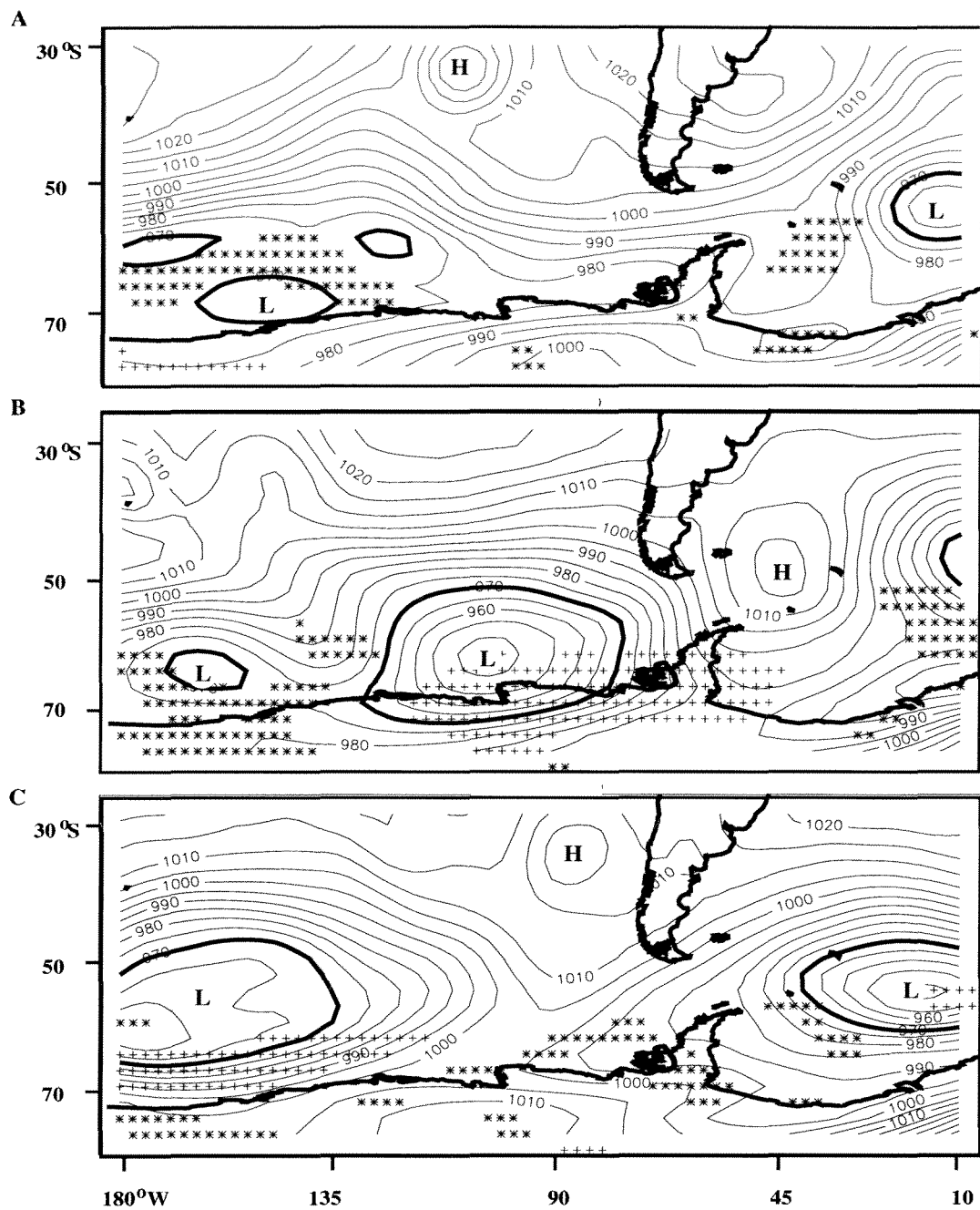
Figure 34. NCEP-derived sea level pressure for Drake Passage and the Southern Ocean (180°W to 30°W) for A) 1 Aug. 1993, B) 5 Aug. 1993 and C) 15 Aug. 1993. NCEP grid cells with temperature anomalies 10°C above and below the monthly mean are indicated with a plus (+) and an asterisks (*), respectively.
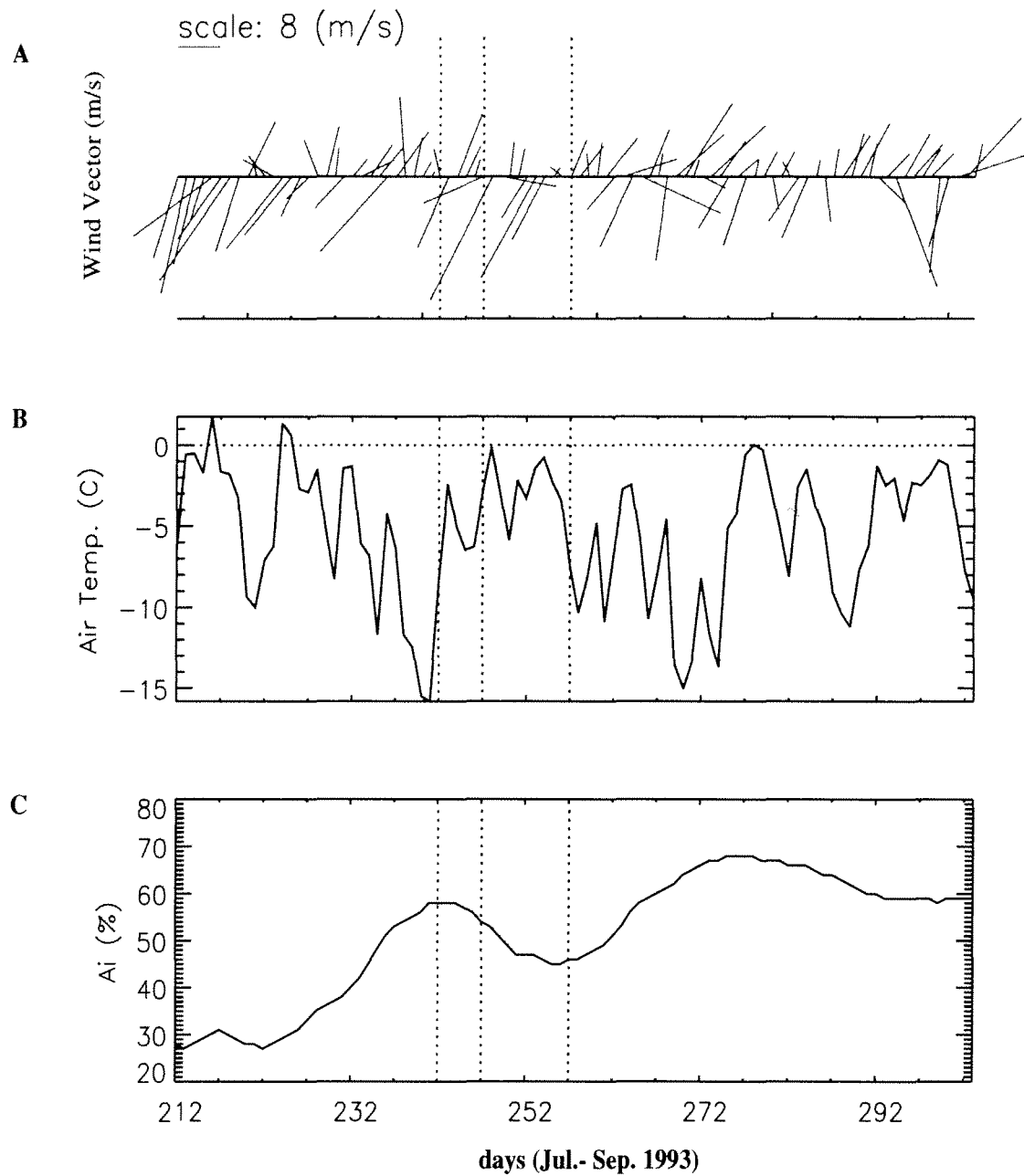
Figure 35. Daily averaged atmospheric and ice conditions for July-September 1993 at Faraday Station. A) Wind vectors with positive x-axis aligning with East, B) Atmospheric temperature and C) GSFC SMMR/SSMI near-Palmer ice area. Days 243, 247 and 257 are indicated with vertical dotted lines and correspond to the days in Figure 34a-c.

system) are associated with warmer conditions. This suggests that low pressure systems in Drake Passage have a significant impact on the overall heat budgets along the Antarctic Peninsula and suggests a link between the frequency and duration of storms and the warm/cold, low/high ice year relationship mentioned in Smith [1996].

5.2.2 The relationship between low pressure systems and interannual variability in the ice cycle

The relationship between storms and ice cover along the shelf to the west of the Antarctic Peninsula has been suggested by Jacobs and Comiso [1993] who relate the extreme low ice year of 1989 to anomalously high winter temperatures, winds from the north and increased storminess. Jacobs and Comiso [1993] do not quantify the "increased storminess" statement; however, it is reasonable to assume that an increase in the frequency, and/or, duration of low pressures in Drake Passage may be associated with increased storm activity.

The idea that synoptic, low pressure systems in Drake Passage result in warmer atmospheric conditions can be extended to include an argument which links the frequency and duration of these low pressure systems to the observed high and low ice years. A year with more frequent and/or longer duration low pressures in Drake Passage would tend to produce milder winters and lower ice coverage. Carleton and Fitch [1993] and Carrasco and Bromwich [1994] studied the relationship between synoptic low pressure systems and the outbreak of mesoscale cyclones after their passage of the Antarctic Peninsula. They indicate that after the passage of synoptic low, cold air outbreaks generate increased cyclonic activity. Van Loon [1991] indicates that the path of the synoptic low pressure systems are such that they either pass the Antarctic Peninsula, or stall in the South Pacific. The storms which stall in the South Pacific tend to produce winters with warmer, average winter temperatures and reduced ice cover.

The monthly NCEP data described in Section 3.1.4 can be used to explore the

link among atmospheric surface pressures, temperature and ice concentration in the vicinity of the Antarctic Continent (Figure 36). Years with anomalously low atmospheric pressures west of the Antarctic Peninsula correspond to years with above average winter temperatures. High and low ice years (Figure 9) correlate to the temperature and pressure anomalies (Figure 36). This relationship is especially apparent in the low ice years in 1983 and 1989 and the high ice year in 1986. Thus, the high/low ice year to cold/warm winter temperature correlation presented in Stammerjohn and Smith [1996] can be extended to include the anomaly in atmospheric surface pressure. All of these relate back to the idea of an Antarctic Circumpolar Wave (ACW) introduced by White and Peterson [1996]. White and Peterson [1996] track atmospheric and oceanic conditions around the Antarctic Continent for several years and find a coupling between the atmospheric temperature, sea level pressure, SST and ice cover. They find a wave, which they call the ACW, in the variable anomalies (departure from a mean) which circles the Continent with a period of 5 to 7 years. The role that low pressure systems play in determining atmospheric temperatures is related to the concept of an ACW and also relates to the observations presented in Jacobs and Comiso [1993] who state that the low ice year of 1989 corresponds to a time of "increased storminess". Results from the numerical model indicate that the direct mechanism for a high or low ice year is an increase or decrease of winter sensible heat flux which is directly related to the atmospheric temperatures.

5.3 Modeled results

5.3.1 Modeled heat fluxes and ice growth

Modeled ice free heat fluxes agree with the heat budgets calculated using atmospheric data from Faraday Station; an expected result, given that the same equations were used in both calculations. The only real difference between the ice free
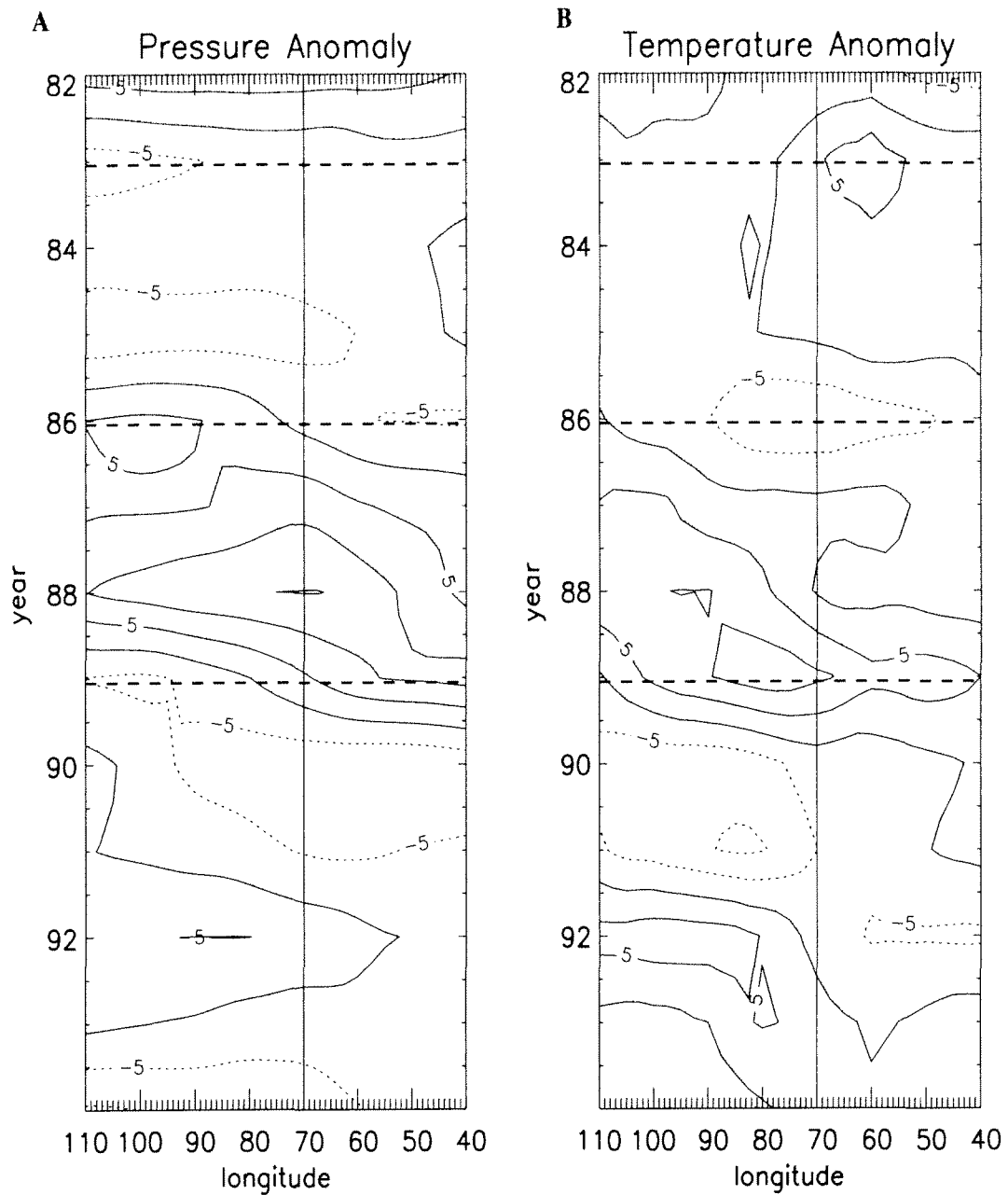
Figure 36. August A) Pressure (mb) and B) Temperature (°C) anomaly for 65°S. The vertical line indicates the location of the west Antarctic Peninsula shelf. Low ice years (1983 and 1989) and a high ice year (1986) are indicated with horizontal dashed lines for reference.

heat fluxes calculated from station data and the simulated heat fluxes is the use of modeled derived SST in the simulation. As already discussed, the overall heat budget is not sensitive to the choice of SST and therefore similarities between the calculations are not surprising.

Modeled heat fluxes between AASW and the ice are on the order of 5 to 10 W m^{-2} while the ice free heat fluxes are generally between 30 and 50 W m^{-2} with maximum heat losses on the order of 100 W m^{-2}. This result is consistent with Arctic simulations [Parkinson and Washington, 1979] where heat fluxes through the 2% of the model which remained ice free were much larger than that through the ice. In this study, through ice heat fluxes were an order of magnitude smaller than those in the ice free regions. The difference between the the results in this study and those of Parkinson and Washington [1979] most likely results from the fact that the west Antarctic Peninsula shelf is generally covered by relatively thin ice as opposed to the thick ice conditions in the Arctic. The averaged through ice heat flux, reported above, excludes the large peak which occurs during the spring when the heat loss from AASW to the ice are calculated to be in excess of 100 W m^{-2}. This large heat flux lasts for a short period of time and drives the rapid melt at the end of the ice cycle.

The result that simulated and calculated sensible heat fluxes were found to be orders of magnitude larger than latent heat fluxes is consistent with results from studies on the Ross Ice Shelf [Stearns and Weidner, 1993]. The low fluxes of latent heat result from the high relative humidities observed in the region (Figure 16c).

5.4 Modeled ice cycle

The simulated ice cycle reproduces well the GSFC SMMR/SSMI record capturing key features such as the timing of initial growth and the rapid spring melt (Figure 25a). The modeled ice cycle also reproduces much of the higher frequency variability

observed in the ice field which is most likely associated with the passage of storms through Drake Passage. The model results agree with the observations from the open-ocean, heat flux calculation which indicate that the timing of the ice cycle is largely determined by net solar radiation while the ice extent is determined by sensible heat flux driven by atmospheric temperatures.

Results from the model also suggest that modified-UCDW on the shelf influences overall ice thickness. Once AASW stratification is eroded (due to surface mixing, cooling and brine rejection), heat which is diffused vertically through the permanent pycnocline is available to melt the ice from underneath. Increasing the heat in the sub-pycnocline waters increases the overall heat available to AASW and reduces the overall ice thickness (Figure 31a,c). Similarly, increasing mixing reduces ice concentration (Figure 31b,d). As Martinson [1990] found for the Weddell Sea, this latter result indicates the importance of the role of the double diffusive instability in the balance of heat and salt in AASW. The process increases the flux of heat to AASW without greatly increasing the exchange of salt (Figure 32).

The simulations demonstrate that the two dominate terms in (23) are ice growth in the ice-free portion of the model (driven by sensible heat loss) and ice melt at the ice-ocean interface. These terms determines the net ice growth for a given period of time. The mid-winter reduction in the GSFC SMMR/SSMI ice area (associated with the passage of a low pressure system through Drake Passage and discussed in the previous section) is reproduced by the model (Figure 25a) suggesting that some of the reduction results from thermodynamic effects. When atmospheric temperature is warm, sensible heat losses from AASW to the atmosphere are reduced thus shutting off ice growth in the portion of the model which remains ice free. When ice is not being formed in the open ocean, ice melt at the ice-ocean interface drives net ice melt (see day 240 in Figure 26a). While this argument does not rule out the effect of motion on ice reduction, it does suggest that thermodynamics is important.

5.5 Modeled surface water hydrography

The model reproduces typical temperature and salinity ranges observed in the hydrography as well as several key hydrographic features of the system such as *mld* and the top of the permanent pycnocline. In this section, these features will be discussed.

5.5.1 Surface mixed layer and mixed layer depths

The depth of the mixed layer, and the hydrographic character of the upper water column, results from complex interaction between buoyancy forcing associated with surface thermodynamics (including ice processes) and momentum fluxes associated with wind and ice induced motion. Surface cooling during the fall, and the subsequent brine rejection associated with ice formation, drive winter *mld's* to the depth of the permanent pycnocline (140 to 150 m). In addition to the buoyancy driven convective mixing, momentum flux under the ice is large and these combine to produce large turbulent fluxes (Figure 29) which also deepen the mixed layer.

The absorption of short wave radiation through open leads during the spring drives a large heat flux to AASW which melts the ice over a period of a few weeks. This modeled, rapid ice melt, reproduces observations presented in Stammerjohn and Smith [1996] and is a strong indication that the input of solar radiation dominates the timing of the ice cycle. Ice melt generates a thin layer of fresh water at the surface of the model. Once all of the ice has melted, surface heating warms the surface layer increasing the surface stratification and generating a distinct seasonal pycnocline. It is between this seasonal pycnocline and the top of the permanent pycnocline where the distinct temperature minimum of WW is found.

Models that use the free drift equations (Section 3.4.4) for ice velocity tend to overestimate the *mld* because of excessive ice velocity. The free-drift equations lack internal pressure terms (i.e., rheology) which results from horizontal gradients in

the ice thicknesses or contact with land masses.

Modeled ice velocities in this study are typically 0.5 to 0.75 m s^{-1} which are higher than one would expected and a balance is established in (34) between the drag at the ice-water and atmosphere-ice interfaces ($\tau_{iw}^{(x,y)}$) and air-ice ($\tau_{ai}^{(x,y)}$), respectively). This analysis is not shown, but is consistent with results reported in Ikeda [1989]. Despite this limitation of using (34), the modeled depths of the convective, winter mixed layer agree well with observations (Figure 28) indicating that the higher than expected ice velocities do not invalidate the solution and indicates that the depth of the winter mixed layer is largely determined by surface buoyancy effects and the position of the permanent pycnocline. The mixing under the ice is sufficient to eliminate any stratification from mid-winter ice melt.

The model fails to reproduce surface salinities which are fresher that 33.2 observed during the fall 1993 cruise [Smith et al., 1999] even after ice melt. Smith et al. [1999] indicate that stations occupied where the fresh water were sampled was near near Marguerite Bay most likely originates as glacial melt. The modeled salinity changes are consistent with the formation and melting of the amount of ice produced during the simulation and the prescribed precipitation.

5.5.2   The depth of the permanent pycnocline

During the winter, the permanent pycnocline is defined by the depth of the mixed layer and is generally found between the depths of 140 to 150 m (Figure 28a). As discussed in the previous section, winter AASW hydrography is characterized by well mixed conditions and no stratification. During the spring and summer, surface warming and fresh water input results in the formation of a seasonal pycnocline (Figure 4a). The seasonal pycnocline persists through the fall when intense fall and winter mixing (Figure 29a), once again eliminates surface stratification, and the seasonal pycnocline.

The formation of the seasonal pycnocline plays an important role in the position of the permanent pycnocline. When stratification exists in the upper 100 m of the water column, heat and salt fluxes from beneath the permanent pycnocline are trapped at the depth of WW warming it and increasing its salinity. The trapping of heat and salt appears as a slow lifting of the permanent pycnocline which occurs throughout the simulation while the surface of the model is stratified. Once the surface stratification is eliminated, the heat stored in WW is released for mixing with surface waters; thus, a direct link between the heat flux though the permanent pycnocline and the atmosphere/ice interfaces is established. This transfer is further enhanced by the intense winter mixing.

5.5.3 Modified-CDW and double diffusion

The warm, salty character of the sub-pycnocline water on the shelf differentiates the shelf to the west of the Antarctic Peninsula from other Antarctic shelf systems [Hofmann and Klinck, 1998]. As discussed in the previous section, the heat flux through the permanent pycnocline may play an important role in the hydrographic character of WW and in the formation of ice. While the timing of the ice cycle appears to be determined by input of solar radiation (in particular short wave radiation) the extent of winter ice is determined by a delicate balance between melting at the base of the ice and ice formation at the ice-ocean interface. To a large extent, atmospheric conditions control this balance; however, heat fluxes through the permanent pycnocline definitely impacts growth at the ice ocean interface and therefore affect net ice production. The model indicates that heat fluxes through the permanent pycnocline are typically 10 W m^{-2} which is also the average under ice heating suggesting that the heat supplied from beneath the permanent pycnocline drives winter ice melt, when atmospheric conditions would favor growth.

For model simulations with warm sub-pycnocline temperature (i.e., consistent

with pure UCDW) the winter ice cover was reduced by nearly 50% while the model formed more ice for simulations with reduced deep temperatures. Changes in the sub-pycnocline hydrography affect the ice field primary after day 170 due to the presence of the seasonal pycnocline (Figure 28).

Double diffusion increases the flux of heat (primarily) and salt (slightly) through the permanent pycnocline to AASW which determining the character of WW. The importance of double diffusion to the overall heat budget is first presented in Smith et al., [1999] and Klinck [1998] and explored in this study through its implementation in the numerical model. The results indicate that the process is important in determining the overall thickness of ice during maximum ice extent (Figure 31b,c) and the hydrography of WW (Figure 32). When double diffusion is not included in the model, WW does not warm sufficiently; however, if the background diffusion is increased to compensate for the under-heating then WW becomes too warm and salty (Figure 32). This result indicates that the differential transfer of heat and salt (more heat than salt) is important in determining the character of AASW, in particular WW.

5.6 Trends observed from the 16 year model run

The long record of atmospheric data from Faraday was used to force the model over a 16 year period which coincides with the GSFC SMMR/SSMI ice area time series (Figure 9b). Modeled trends in the ice concentrations and the hydrographic response and mixed layer structure are discussed in this section.

5.6.1 Modeled ice cycle

The winter ice cover to the west of the Antarctic Peninsula is characterized by an inter-annual variability of high and low ice years which correlates to atmospheric conditions (Figure 9) [Jacobs and Comiso, 1993; Smith et al., 1996; Stammerjohn

and Smith, 1996 and Stammerjohn and Smith, 1997]. In Section 4.3.4 the one dimensional model is forced with atmospheric conditions from Faraday and the resulting ice cycle reproduces this high/low ice cycle fairly well (Figure 33). Of particular interest is the model's ability to reproduce one of the highest and lowest ice years on record (1987 and 1989, respectively). In addition to the extremes, the model was able to reproduce many of the observed trends such as the consecutive high ice years of 1979-1982, which were immediately followed by three low ice years from 1983 to 1985.

Given the vertical only character of the model used in the study, and its ability to reproduce many of the observed trends in the ice field, these results support the findings of Smith [1996] who suggests an atmospheric (that is, thermodynamic) control on the ice cover. This conclusion is also supported by the model results which suggest that the primary mechanism for winter ice growth is sensible heat loss during the winter months which is primarily driven by temperature differences between the atmosphere and the ocean. It also supports the concept of the ACW which may account for the observed inter-annual variability in atmospheric conditions along the Antarctic Peninsula.

While the model does produce 1980 as a high ice year, it fails to indicate it as the highest ice on record (Figures 9b and 33a). One possible explanation for this mismatch is the exclusion of horizontal processes in the model and the numerical treatment of the sub-pycnocline water which are nudged to hydrographic conditions imposed from 1993 data. Given the persistent character of sub-pycnocline waters [Hofmann et al., 1996], over decadal time scales, the use of 1993 data throughout the simulation is a reasonable first assumption. However, the sensitivity of the modeled ice cover to changes in the parameterization of double diffusion, and the temperature of the modified-UCDW (Section 4.3.3) suggests that the difference in the modeled ice cover could be explained by changed temperature of the sub-pycnocline waters.

The data record does not contain detailed observations of the shelf waters for 1980; however, if the waters were colder than the average temperature used in the model, the difference would be explained.

5.6.2 Hydrographic response

The trends in the ice field which were discussed in the previous section, and the relationship between the ice and the atmosphere have been understood for several years. Unfortunately, the lack of a long time series of high quality hydrographic data for the region has limited investigations to the atmosphere and the ice cycle while the ocean's role has not been included. This analysis based on an observation of a model permits the ocean's role to be investigated.

Of particular interest from the model results are the depth of the mixed layer and the permanent pycnocline. A time series of these parameters are available from the hydrographic data but are important in understanding the system's physics and biology. Model results indicate that the warm/cold to low/high ice year linkage can be extended to include shallow/deep winter mixed layers (Figure 33a). The depth of the permanent pycnocline was generally found 40 to 50 m deeper during high ice years as compared to low ice years.

Additionally, spring *mld* was found to be shallower and more stable following a high ice year. This results from an increased input of fresh water from ice melt. Results also suggest that years following high ice cover would favor stability in the surface waters and increase primary production.

While the results from the sixteen year simulation are interesting, they must be interpreted with caution. The model used for these simulations is only a vertical model and neglects horizontal processes on ice dynamics and thermodynamics. The low ice years, which appear to coincide with years of increased low pressure activity in Drake Passage (Figure 36) would also be years when prevailing, geostrophic winds

from the north would compress ice against the coast, closing leads and producing thicker ice cover. These dynamics oppose the thermodynamic tendency increased atmospheric temperatures to reduce overall ice cover. A full investigation of horizontal processes would require a more elaborate numerical model capable of simulating ice convergence/divergence.

CHAPTER 6
SUMMARY AND CONCLUSIONS

The oceanic and atmospheric observations combined from ship and station observations near Palmer Station provide an excellent source of data for the investigation of air/ice/sea interactions along the region to the west of the Antarctic Peninsula. These data also provide the basis for the development of numerical models which are used to further investigate the physical processes in the system, its temporal variability and the oceanic response to atmospheric and ice driven surface buoyancy forcing. The observations and the results from the simulations are summarized in this chapter.

6.1   Hydrographic observations

Hydrography observations along the west Antarctic Peninsula are used to characterize the shelf waters as consisting of a two layer system. AASW occupies the upper 100 to 200 m of the water column and exhibits hydrographic variability on time scales consistent with atmospheric heating, cooling and ice related buoyancy forcing. A distinct permanent pycnocline separates AASW from a deeper layer of water with oceanic origin originating in the ACC as UCDW. This lower layer of water has relatively warm temperatures ($> 1.4°C$) and high salinities (> 34.6 psu) and exhibits very little variability on seasonal, annual and decadal time scales.

Klinck [1998] and Smith et al.[1999] propose that the deep, modified-UCDW forms as pure UCDW, from the ACC, intrudes on the the shelf and diffuses heat and salt vertically through the permanent pycnocline to the cooler, fresher AASW (WW) above. The authors test a first order balance of horizontal and vertical transfer of heat and salt and find that the balance is consistent with reasonable oceanic parameters. Calculations presented in this study support this finding and suggest

that the hydrographic character of the sub-pycnocline waters can be maintained with horizontal eddy diffusion coefficients on the order of 10 m^2 s^{-1} which balance vertical diffusive losses from modified-UCDW to AASW (WW).

Simple double diffusive calculations based on $\Delta T^{\frac{4}{3}}$ models and model results indicate that vertical diffusion of heat (mainly) and salt (slightly) are enhanced by double diffusion. Model results suggest that double diffusion accounts for at least 50% (5 to 10 W m^{-2}) of the total heat transferred through the permanent pycnocline while the prescribed background diffusion accounts for the rest. Furthermore, double diffusion allows for a differential vertical transfer of heat and salt which appears to be necessary for the proper hydrographic character in the bottom portion of AASW (WW).

6.2 Vertical and horizontal fluxes of heat and salt

The atmospheric data from the vicinity of Palmer Station are used to estimate surface rates of heating and to rank the importance of individual terms in the heat overall budget. Using these data, net atmospheric heating, and cooling, rates between the 1993 Palmer-LTER cruises are estimated to be ± 50 W m^{-2}. These estimates agree with calculations presented in Klinck [1998] who used measured oceanic temperatures to estimate the required heating, and cooling, necessary to produce the observed hydrographic changes between the same cruises.

The results from the open-ocean heat budget (Section 4.1.2) indicate overall exchanges of heat at the atmosphere/ice/ocean interface are on the order of ± 150 to 200 W m^{-2}. The net heat budget for 1993, estimated by integrating the time series of calculated heat fluxes, balances giving a net heating near zero W m^{-2}. This net result near zero requires the assumption that heating from below the permanent pycnocline is a persistent process throughout the year and that, on average, 10 W m^{-2} of heat is lost from AASW to sea ice when sea ice is present. These two

assumptions are supported by the results of the model analysis.

Given the magnitude of the open-ocean, atmospheric heat fluxes, ($\sim \pm 150$ to 200 W m^{-2}) and the closure of the integrated budget, two general conclusions can be made: 1.) heat fluxes at the atmosphere/ocean interface account for most of the vertical exchanges of heat, and 2.) local atmospheric conditions along the west Antarctic Peninsula account for much of the observed variability in the shelf's hydrography. The ability of the vertical model to reproduce the high/low ice cycle means that local atmospheric conditions control ice processes along the region to some extent. This result is consistent with the work of Smith et al. [1996] and Stammerjohn and Smith [1996] who link the high/low ice years along the Peninsula to cold/warm atmospheric conditions.

During the summer months, the surface heat flux is dominated by incoming short wave radiation on the order of 200 W m^{-2} and occurs at a time when sensible heat losses are small because atmospheric and oceanic temperatures are similar. During the fall and through the winter, atmospheric temperatures can reach lows below -15°C while SST is clamped by the freezing point ($T_f \sim$ -2°C). The large differential between atmospheric and oceanic temperatures (with the atmosphere being cooler) leads to high rates of sensible heat loss and dominates the winter heat budget. Open-ocean, wintertime, sensible heat losses can be in excess of 100 to 150 W m^{-2}, producing ice formation in the portion of the ocean which remains open (i.e. leads).

Other terms in the surface heat budget play a less significant role in the overall heating. Net long wave radiation is on the order of 30 W m^{-2} and is a persistent throughout the year; high values of relative humidity ($\sim$ 90%) diminishes the importance of latent heating in the region. Latent heating is typically one tenth that of the sensible heating.

6.3 Momentum fluxes, vertical mixing and the depth of the mixed layer

Mixed layer depths from observations and those from the model are consistent with each other (Figure 28). While mixed layer depths from hydrographic observations give an accurate, detailed account of the surface density structure during the times of the observations, the model provides a tool for evaluating the physical processes which determine the depth of the mixed layer and provides insight into the time evolution of characteristics within AASW. Model results indicate that ice formation, brine rejection, surface cooling and ice driven mixing produce well mixed hydrographic conditions which extend to the bottom of AASW (150 to 200 m).

Well mixed conditions persist throughout the winter until the ice retreats during the spring melt. During this retreat, a thin layer of fresh water forms at the surface of model which warms and stabilizes the surface. Beneath this layer, a seasonal pycnocline forms separating the wind mixed layer at the surface (top 10 to 20 m) from the temperature minimum found at depth indicating the position of the bottom of AASW (WW). This seasonal pycnocline forms a density barrier to the vertical mixing of heat and salt, trapping the heat and salt which is mixed from below the permanent pycnocline in the WW. This heating through the permanent pycnocline slowly erodes the hydrographic character of WW resulting in a lifting of the permanent pycnocline.

Stratification within AASW persists through the summer until the subsequent fall when surface cooling and wind mixing drives the mixed layer deeper. The mixed layer is reset to its winter depths when ice forms during the next winter. As the winter mixed layer is reset, it erodes the heat stored in WW which was trapped by the existence of the seasonal pycnocline. An important period of time in the model simulations occurs when the surface mixed layer is driven back to the depth of the permanent pycnocline. At this time, the stratification within AASW is eliminated

and heat fluxes from modified-UCDW are no longer impeded from the surface and become available to the atmosphere (in the portion of the ocean which remains ice free) and to the ice. The results from the model indicate that when stratification within AASW is eliminated, the under ice growth rate switches from a growth term, to a persistent ice loss term slowing the overall ice growth.

Within AASW, eddy diffusion coefficients are quite large and range from 0.01 to 0.001 m s^{-2} with the higher coefficients occurring in the winter under the influence of ice formation and ice driven mixing. Diffusion coefficients within the permanent pycnocline are typically on the order of 1×10^{-4} $m^2 s^{-1}$ and are enhanced by double diffusion.

6.4 Ice processes

The timing of the ice cycle is largely determined by the input of short wave radiation while the extent of the ice at winter maximum (i.e., thickness and/or concentration) is determined by sensible heat losses at the air/ocean interface. These sensible heat losses drive freezing rates in the open ocean which can exceed several centimeters per day. The primary balance in the ice growth equation is between growth at open ocean and ice melt at the ice-ocean interface. The balance between these two processes determines whether or not ice is forming or melting.

The presence of warm, oceanic water beneath the permanent pycnocline determines the thickness of the ice at maximum ice extent. It does not, however, seem to affect the timing of the onset of ice formation or spring melt. Likewise, the parameterization of heat fluxes through the permanent pycnocline is significant in determining the overall extent of the winter ice thickness. Model results from sensitivity tests indicate that ice cover is reduced by as much as 50% when considering double diffusion in the vertical transfer of heat as compared to when it is not included.

6.5   Temporal variability and winter storms

An interesting result is that ice growth can be stopped, and reversed (ice melt), in mid-winter by large temperature reversals, which occur on time scales coincident with the passage of synoptic low pressure systems through Drake Passage, as seen in atmospheric data collected at Palmer Station. Several mid-winter temperature reversals are seen in the atmospheric data collected at Palmer Station (Figure 16b). The response in the resulting heat budgets and ice growth rates are also observed (Figures 18c and 26b). During several of these mid-winter episodes where atmospheric temperatures warm by 15 to 20°C and ice cover in the model is reduced by up to 40%.

The occurance along the west Antarctic Peninsula of warm (cold) winters low (high) ice cover [Smith et al., 1996] is linked to the frequency and duration of synoptic low pressure systems in and around Drake Passage. An investigation using data from the NCAR/NCEP re-analysis project suggests that a suite of coupled anomalies (i.e., atmospheric pressure at sea level, atmospheric temperatures, SST and ice cover), termed the ACW, manifests itself along the west Antarctic Peninsula and supports concept of high/low ice years.

6.6   Relevance to other studies and concluding remarks

Biologists who study the waters to the west of the Antarctic Peninsula are interested in the sometimes complex density structures which form within AASW under the competing forces of wind mixing, ice driven buoyancy forcing, surface heating and cooling. These forces act to determine the hydrographic character of the surface waters along the west Antarctic Peninsula. Understanding these processes is crucial to understanding the biology for the region.

During the winter, brine rejection, surface cooling and intense wind and ice driven mixing combine to drive deep well mixed layers within AASW. These con-

ditions do not favor biological organisms which have little, or no ability, to control their position within the water column. Conversely, the shallow, stable surface mixed layers which form in the spring during ice melt are conditions which highly favor large blooms of phytoplankton. These concentrations of phytoplankton are the fundamental basis for the region's food web.

The presence of modified-UCDW on the shelf, introduces a unique source of heat and salt to the shelf waters. This heat source is available to interact with the ice and atmosphere along the west Antarctic Peninsula and has potential impact on both biological and atmospheric sciences.

The results from this study are intended to form the basis for future work in the the region. The processes investigated here should lend insight into the development of two- and three-dimensional ice-ocean modeling studies which will be able to directly investigate horizontal processes and how they affect ice cover and biological processes along the west Antarctic Peninsula.

REFERENCES

Blumberg, A. F., and G. L. Mellor, A description of a three-dimensional coastal ocean model, Heaps, N. S. (editor), *Coastal and Estuarine Science 4: Three-Dimensional Coastal Ocean Models.* American Geophysical Union, Washington, D.C., 1987.

Capella, J. E., Circulation and temperature effects on the development and distribution of the eggs and larvae of the Antarctic krill, *Euphausia superba*: A modeling study, Ph.D. thesis, Texas A&M University, 162 pp., 1989.

Carelton A., and M. Fitch, Synoptic aspects of Antarctic mesocyclones, *J. Geophys. Res.*, *98*, 12,997–13,018, 1993.

Carrasco, J. F., and D. H. Bromwich, Climatological aspects of mesoscale cyclogenesis over the Ross Sea and Ross Ice Shelf regions of Antarctica, *Mon. Wea. Rev.*, *122*, 2405–2425, 1994.

Cavalieri D. J., Claire L. P., P. Gloersen, and H. J. Zwally, Arctic and Antarctic sea ice concentrations from multichannel passive-microwave satellite data sets: October 1978 - September 1995, Technical Report 104647, NASA, Goddard Space Flight Center, Washington, D.C., 17 pp., 1997.

Clowes, A. I. J., Hydrography of the Bransfield Strait, *Discovery Reports*, *9*, 1–64, 1934.

Comiso, J. C., D. J. Cavalieri, C. L. Parkinson, and P. Gloersen, Passive microwave algorithms for sea ice concentration: a comparison of two techniques, *Remote Sens. Environ.*, *60*, 375–384, 1997.

Cullather, R. I., D. H. Bromwich, and M. L. Van Woert, Spatial and temporal

variability of Antarctic precipitation from atmospheric methods, *J. of Climate*, *11*, 334–367, 1998.

Everson, I., and D. G. M. Miller, Krill mesoscale distribution and abundance: results and implications of research during the BIOMASS programme, El-Sayed, S. Z. (editor), *Southern Ocean Ecology: the BIOMASS prespective*. Cambridge University Press, Cambridge, pp. 129-144, 1994.

FRAM Group, An eddy-resolving model of the Southern Ocean, *EOS*, *72*, 169, 174–175, 1991.

Fujino, K., E. L. Lewis, and R. G. Perkins, The freezing point of seawater at pressures up to 100 bars, *J. Geophys. Res.*, *79*, 1792–1797, 1974.

Gordon, A. L., and W. D. Nowlin, Jr., The basin waters of the Bransfield Strait, *J. Phys. Oceanogr.*, *8*, 258–264, 1978.

Häkkinen, S., and G. L. Mellor, One hundred years of arctic ice cover variation as simulated by a one-dimensional, ice-ocean model, *J. Geophys. Res.*, *95*, 15,959–15,969, 1990.

Hibler, W. D., III., A dynamic thermodynamic sea ice model, *J. Phys. Oceanogr.*, *9*, 815–846, 1979.

Hofmann, E. E., and J. M. Klinck, Hydrography and circulation of the Antarctic continental shelves: 150°E eastward to the Greenwich Meridian, Robinson, A. R. and K. H. Brink (editors), *The Sea, The Global Coastal Ocean, Regioanl Studies and Synthesis*, Volume *11*, 1998.

Hofmann, E. E., J. M. Klinck, C. M. Lascara, and D. A. Smith, Water mass distribution and circulation west of the Antarctic Peninsula, Ross, R. M., E. E.

Hofmann and L. B. Quetin (editors), *Foundations for Ecological Research West of the Antarctic Peninsula*. American Geophysical Union, 1996.

Huntley, M. E., D. M. Karl, P. P. Niiler, and O. Holm-Hansen, Research on Antarctic coastal ecosystem rates (RACER): an interdisciplinary field experiment, *Deep Sea Res.*, *38*, 911–941, 1991.

Ikeda, M., A coupled ice-ocean mixed layer model of the marginal ice zone responding to wind forcing, *J. Geophys. Res.*, *94*, 9699–9709, 1989.

Jacobs, S. S., and J. C. Comiso, A recent sea-ice retreat west of the Antarctic Peninsula, *Geophys. Res. Let.*, *20*, 1171–1174, 1993.

Jones, P. D., and D. W. S. Limbert, *A data bank of Antarctic surface temperature and pressure data, Office of Energy Research*, Office of Basic Energy Sciences, Carbon Dioxide Research Division, Washington, D. C., 1987.

Kamph, J., and J. O. Backhaus, Shallow, brine-driven free convection in polar oceans: Nonhydrostatic numerical process studies. *J. Geophys. Res.*, *103*, 5577–5594, 1998.

Kalnay, E., M. Kanamitsu, R. Kistler, W. Collins, D. Deaven, L. Gandin, M. Iredell, S. Saha, G. White, J. Woollen, Y. Zhu, , A. Leetmaa, R. Reynolds, M. Chelliah, W. Ebisuzaki, W. Higgins, J. Janowiak, K. C. Mo, C. Ropelewski, J. Wang, R. Jenne, and D. Joseph, The NCEP/NCAR 40-year reanalysis project, *Bull. of the Amer. Meteorol. Soc.*, 1996.

Kantha L. H., and C. A. Clayson, An improved mixed layer model for geophysical applications, *J. Geophys. Res.*, *99*, 25,235–25,266, 1994.

Kantha, L. H., and G. L. Mellor, A two-dimensional coupled ice-ocean model of the

Bering Sea marginal ice zone, *J. Geophys. Res.*, *94*, 10,921–10,935, 1989.

Kelly, D., Effective diffusivities within oceanic thermohaline staircases, *J. Geophys. Res.*, *89*, 10,484–10,488, 1984.

Klinck, J. M., Heat and salt changes on the continental shelf west of the Antarctic Peninsula between January 1993 and January 1994, *J. Geophys. Res.*, 7617 - 7636, 1998.

Klinck, J. M., and D. A. Smith, Palmer lter: Comparison of meterological observations from RV N.B. Palmer to those at Palmer Staton, *Antarctic J. of the U. S*, 1995.

Klinck, J. M., R. C. Smith, and D. Menzies, Hydrographic data collected aboard *RV Polar Duke* August-September 1993, Technical Report 94-01, Center for Coastal Physical Oceanography, Old Dominion University, Norfolk, VA, 265 pp., 1994.

Laevastu, T., Factors affecting the temperature of the surface layer of the sea, *Comment. Phys. Math.*, *25*, 1, 1960.

Large W. G., J. C. McWilliams, and S. Doney, Oceanic vertical mixing: A review and model with a nonlocal boundary layer parameterization, *Rev. of Geophys.*, *99*, 25,235–25,266, 1994.

Lascara, C. M., R. C. Smith, D. Menzies, and K. S. Baker, Hydrographic data collected aboard *RV Polar Duke* January-February 1993, Technical Report 93-02, Center for Coastal Physical Oceanography, Old Dominion University, Norfolk, VA, 265 pp., 1993a.

Lascara, C. M., R. C. Smith, D. Menzies, and K. S. Baker, Hydrographic data col-

lected aboard *RV Polar Duke* november 1991, Technical Report 93-01,, Center for Coastal Physical Oceanography, Old Dominion University, Norfolk, VA, 95 pp., 1993b.

Lemke, P., A coupled one-dimensional sea ice-ocean model, *J. Geophys. Res.*, *92*, 13,164–13,172, 1987.

Lemke, P., W. B. Owens, and W. D. Hibbler, III, A coupled sea ice-mixed layer-pycnocline model for the Weddell Sea, *J. Geophys. Res.*, *95*, 9513–9525, 1990.

Marmorino, G. O., and D. R. Caldwell, Heat and salt transport through a diffusive thermohaline interface, *Deep Sea Res.*, *23*, 59–67, 1976.

Marr, J. W. S., The natural history and geography of the Antarctic krill (*Euphausia superba* Dana), *Discovery Reports*, *32*, 33–464, 1962.

Martinson, D. G., Evolution of the Southern Ocean winter mixed layer and sea ice: open ocean deepwater formation and ventilation, *J. Geophys. Res.*, *95*, 11,641–11,654, 1990.

Maykut, G. A., and N. Untersteiner, Numerical prediction of the thermodynamic response of Arctic sea ice to environmental changes, Technical Report RM-60093-PR, The Rand Corporation, Santa Monica, CA, 1969.

Mellor, G. L., *User's guide for a three-dimensional, primitive equation, numerical ocean model.* Princeton University: Report AOS Program, Princeton NJ 08540, 1993.

Mellor, G. L., and L. H. Kantha, An ice-ocean coupled model, *J. Geophys. Res.*, *94*, 10,937–10,954, 1989.

Mellor, G. L., and T. Yamada, A hierarchy of turbulence closure models for planetary boundary layers, *J. Atmos. Sci.*, *31*, 1791–1896, 1974.

Mellor, G. L., and T. Yamada, Development of a turbulence closure model for geophysical fluid problems, *Rev. of Geophys. Space Phys.*, *20*, 851–875, 1982.

Mosby, H., The Waters of the Atlantic Antarctic Ocean. Scientific Results of the Norwegian Antarctic Exediton 1927-1928 *11*, 1-131.

Niiler, P. P., A. Amos, and J. H. Hu, Water masses and 200 m relative geostrophic circulation in the western Bransfield Strait region, *Deep Sea Res.*, *38*, 943–959, 1991.

Niiler, P. P., J. Illeman, and J. H. Hu, RACER: Lagrangian drifter observations of surface circulation in the Gerlache and Bransfield Straits, *Antarctic J. of the U. S.*, *25*, 134–137, 1990.

Nowlin, W. D., Jr., and M. Clifford, The kinematic and thermohaline zonation of the Antarctic Circumpolar Current at Drake Passage, *J. Mar. Res.*, *40*, 481–507, 1982.

Parkinson, C. L., and W. M. Washington, A large-scale numerical model of sea ice, *J. Geophys. Res.*, *84*, 311-336, 1979.

Semtner, A. J., Jr., *An oceanic general circulation model with bottom topography, numerical simulation of weather and climate.* Technical Report 9, Department of Meteorology, University of California, 1974.

Semtner, A. J., Jr., A model for the thermodynamic growth of sea ice in numerical investigations of climate, *J. Phys. Oceanogr.*, *6*, 379–389, 1976.

Sievers, H. A., and W. D. Nowlin Jr., The stratification and water masses at Drake Passage, *J. Geophys. Res.*, *89*, 10,489–10,514, 1984.

Smith, D. A., E. E. Hofmann, J. M. Klinck, and C. M. Lascara, Hydrography and circulation of the West Antarctic Peninsula shelf, *Deep Sea Res.*, *46*, 925-949, 1999.

Smith, D. A., R. A. Locarnini, B. L. Lipphardt, Jr., and E. E. Hofmann, Hydrographic data collected aboard *RV Nathaniel B. Palmer* March-May 1993, Technical Report 93-04,, Center for Coastal Physical Oceanography, Old Dominion University, Norfolk, VA, 265 pp., 1993a.

Smith, D. A., R. C. Smith, and D. Menzies, Oceanographic data collected aboard *RV Nathaniel B. Palmer* March-May 1993, Technical Report 93-05, Center for Coastal Physical Oceanography, Old Dominion University, Norfolk, VA, 265 pp., 1993b.

Smith, R. C., K. Baker, W. Fraser, E. Hofmann, D. Hofmann, D. Karl, J. Klinck, L. Quetin, B. Prézelin, R. Ross, W. Trivelpiece, and M. Vernet, The Palmer LTER: A Long-Term Ecological Research Program at Palmer Station, Antarctica, *Oceanography*, *8*, 77–86, 1995.

Smith, R. C., S. E. Stammerjohn, and K. S. Baker, Surface air temperature variations in the western Antarctic Peninsula region, Ross, R. M., E. E. Hofmann and L. B. Quetin (editors), *Foundations for Ecological Research West of the Antarctic Peninsula*. American Geophysical Union, 1996.

Smith, R. C. and C. R. Booth, Oceanographic bio-optical profiling system, *A;;lied Optics*, *23*, 2791-2797, 1984.

Stammerjohn, S., and R. C. Smith, Spatial and temporal variability in West Antarctic sea ice coverage, Ross, R. M., E. E. Hofmann and L. B. Quetin (editors), *Foundations for Ecological Research West of the Antarctic Peninsula*. American Geophysical Union, 1996.

Stammerjohn S., and R. C. Smith, Opposing southern ocean climate patterns as revealed by trends in regional sea ice coverage, *Climate Change*, *37*, 617–638, 1997.

Stearns, C. R., and D. H. Bromwich, Sensible and latent heat flux estimates in Antarctica, Bromwich, D. H. and C. R. Stearns (editors), *Antarctic Meteorology and Climatology: Studies Based on Automatic Weather Stations*, volume *61*, 1993.

Steel, M. G., G. L. Mellor, and M. G. McPhee, The role of the molecular sublayer in the melting or freezing process, *J. Phys. Oceanogr.*, *19*, 139–147, 1989.

Stein, M., The distribution of water masses in the South Shetland Islands area during FIBEX, *Mem. Nat. Inst. Polar Res.*, *27*, 16–23, 1983.

Stein, M., Variability of water masses and currents off the Antarctic Peninsula during SIBEX, *Arch. FischWiss.*, *37*, 25–50, 1986.

Stein, M., Seasonal variation of waters masses in Bransfield Strait and adjacent waters, *Arch. FischWiss.*, *39*, 15–38, 1989.

Stein, M., Variability of local upwelling off the Antarctic Peninsula. 1986-1990, *Arch. FischWiss.*, *41*, 131–158, 1992.

Stein, M., and S. Rakusa-Suszczewski, Geostrophic currents in the South Shetland Islands area during FIBEX, *Mem. Nat. Inst. Polar Res.*, *27*, 24–34, 1983.

Stein, M., and S. Rakusa-Suszczewski, Meso-scale structure of water masses and bottom topography as the basis for krill distribution in the se Bransfield Strait February-March 1981, *Meeresforsch.*, *30*, 73–81, 1984.

Stossel, A., P. Lemke, and W. B. Owens, Coupled sea ice-mixed layer simulations for the Southern Ocean, *J. Geophys. Res.*, *95*, 9539–9555, 1990.

Turner, J. S., *Buoyancy Effects in Fluids*, Cambridge University, New York, 1973.

UNESCO, Algorithms for computation of fundamental properties of seawater, Fofonoff, N. P. and R. C. Millard, Jr. (editors), *Technical Papers in Marine Science.*, volume *44*, 53pp, 1983.

Van Loon H., A review of the surface climate of the Southern Hemisphere and some comparisons with the Northern Hemisphere, *J. of Marine Sys.*, *2*, 171–194, 1991.

Wamser, C. and D. G. Martinson, Drag coefficients for winter Antarctic pack ice, *J. Geophys. Res.*, *98*, 12,431–12,437, 1993.

Waters, K. J., and R. C. Smith, Palmer LTER: A sampling grid for the Palmer LTER program, *Antarctic J. of the U. S.*, *27*, 236–239, 1992.

Webb, D. J., P. D. Killworth, A. Coward, and S. Thompson, *The FRAM Atlas of the Southern Ocean*. Natural Environmental Research Council, Swindon, U.K., 1991.

White, W. B., and R. Peterson, An Antarctic circumpolar wave in surface pressure, wind, temperature, and sea-ice extent, *Nature*, *381*, 699–702, 1996.

Whitworth, T., III, W. D. Nowlin, Jr., A. H. Orsi, R. A. Locarnini, and S. G. Smith,

Weddell Sea shelf water in the Bransfield Strait and Weddell-Scotia Confluence, *Deep Sea Res.*, *41*, 629–641, 1994.

Zillerman, J. W., A study of some aspects of radiation and heat budgets of southern hemisphere oceans, *Meteorol. Stud.*, *26*, 562–575, 1972.

VITA

David A. Smith

Department of Ocean, Earth and Atmospheric Sciences
Old Dominion University
Norfolk, VA 23529

Education:

Ph.D. Ocean, Earth & Atmos. Sciences, Old Dominion University (1999)
B.A.   Physics, West Virginia University (1990)
B.S.   Secondary Education, West Virginia University (1990)

Professional Experience:

1991 - 1999   Graduate Research Assistant, Department of Oceanography, Old Dominion University, Norfolk VA

1990 - 1991   Graduate Teaching Assistant, Department of Physics, Old Dominion University, Norfolk VA

Publications:

Smith, D.A., E.E. Hofmann, J.K. Klinck and C.M. Lascara. Hydrography and circulation of the west Antarctic Peninsula continental shelf. *Deep-Sea Research,* 46: 925-949, 1999

Hofmann, E.E., J.M. Klinck, C.M. Lascara and D.A. Smith. Water mass distribution and circulation west of the Antarctic Peninsula. In: *Foundations for ecological research west of the Antarctic Peninsula,* Ross, R.M., E.E. Hofmann and L.B. Quetin, editors, Antarctic Research Series, Vol. 70, American Geophysical Union, Washington DC., pp 61-80, 1996.

Klinck, J.M. and D.A. Smith. Effect of wind changes during the last glacial maximum on the circulation in the Southern Ocean. *Paleoceanography,* 8: 427-433, 1993.